IMPACT OF PARTIALLY NON-ERGODIC PROBABILISTIC SEISMIC HAZARD ON RISK ASSESSMENT OF RC BUILDINGS IN TURKEY

A THESIS SUBMITTED TO
THE GRADUATE SCHOOL OF NATURAL AND APPLIED SCIENCES
OF
MIDDLE EAST TECHNICAL UNIVERSITY

BY

ÖZGÜR ÇOBANYILMAZ

IN PARTIAL FULFILLMENT OF THE REQUIREMENTS
FOR
THE DEGREE OF MASTER OF SCIENCE
IN
ENGINEERING SCIENCES

DECEMBER 2023

Approval of the thesis:

IMPACT OF PARTIALLY NON-ERGODIC PROBABILISTIC SEISMIC HAZARD ON RISK ASSESSMENT OF RC BUILDINGS IN TURKEY

submitted by **ÖZGÜR ÇOBANYILMAZ** in partial fulfillment of the requirements for the degree of **Master of Science** in **Engineering Sciences, Middle East Technical University** by,

Prof. Dr. Halil Kalıpçılar
Dean, Graduate School of **Natural and Applied Sciences** _____

Prof. Dr. Murat Dicleli
Head of the Department, **Engineering Sciences** _____

Assoc. Prof. Dr. Zehra Çağnan Ertuğrul
Supervisor, **Engineering Sciences, METU** _____

Examining Committee Members:

Prof. Dr. Murat Dicleli
Engineering Sciences, METU _____

Assoc. Prof. Dr. Zehra Çağnan Ertuğrul
Engineering Sciences, METU _____

Assoc. Prof. Dr. Rıza Seçer Orkun Keskin
Civil Engineering, TED University _____

Date: 06.12.2023

I hereby declare that all information in this document has been obtained and presented in accordance with academic rules and ethical conduct. I also declare that, as required by these rules and conduct, I have fully cited and referenced all material and results that are not original to this work.

Name Last name :Çobanyılmaz, Özgür

Signature :

ABSTRACT

IMPACT OF PARTIALLY NON-ERGODIC PROBABILISTIC SEISMIC HAZARD ON RISK ASSESSMENT OF RC BUILDINGS IN TURKEY

Çobanyılmaz, Özgür
Master of Science, Engineering Sciences
Supervisor : Assoc. Prof. Dr. Zehra Çağnan Ertuğrul

December 2023, 125 pages

This study aims to compare the seismic risk estimates obtained based on Probabilistic Seismic Hazard Assessment (PSHA) employing both the traditional ergodic approach and a partially non-ergodic site-and source-specific approach. Two different partially non-ergodic ground-motion attenuation relationships available for Turkey are adopted for this purpose. For four sites located in Turkey under the predominant influence of Eastern Anatolian Fault, seismic hazard is estimated using both the traditional ergodic approach and partially non-ergodic approach. For each site, the hazard estimates of the two PSHa approaches are utilized to select and scale two sets of hazard-consistent ground-motion records according to the Turkish Design Princible for Buildings Subjected to Earthquakes (2018) that are employed to estimate the response of eight ductile structures representing the low- to mid-rise reinforced concrete buildings is Eastern part of Turkey. The seismic responses of these reinforced concrete structures are estimated by performing nonlinear response history analyses according to the Turkish Design Principles for Buildings Subjected to Earthquakes (2018) regulations.

Keywords: Probabilistic Seismic Hazard Assessment, Ergodic Approach, Partially Non-Ergodic Approach

ÖZ

TÜRKİYE'DE BETONARME YAPILARIN RİSK DEĞERLENDİRMESİNDE KISMİ ERGODİK OLMAYAN OLASILIKSAL SİSMİK TEHLİKENİN ETKİLERİ

Çobanyılmaz, Özgür
Yüksek Lisans, Mühendislik Bilimleri
Tez Yöneticisi: Doç. Dr. Zehra Çağnan Ertuğrul

Aralık 2023, 125 sayfa

Bu çalışma, geleneksel ergodik ve yakın zamanda ortaya atılmış olan kısmi ergodik olmayan yaklaşımlar kullanılarak elde edilmiş olasılıksal sismik tehlike analiz sonuçlarının deprem riski tahminleri üzerindeki etkisini karşılaştırmayı amaçlamaktadır. Bu hedefle, Türkiye için geliştirilmiş iki kısmi ergodik olmayan yer hareketi azalım ilişkisi kullanılmıştır. Türkiye'de bulunan Doğu Anadolu Fay Hattı etkisi altındaki 4 yerleşim yeri seçilmiş ve bu yerleşim yerleri için geleneksel ergodik yaklaşım ve kısmi ergodik olmayan yaklaşımlar kullanılarak olasılıksal sismik tehlike hesaplanmıştır. Seçilen dört yerleşim yerinin her biri için, Deprem Etkisi Altında Binaların Tasarımı için Esaslar (2018) uyarınca olasılıksal deprem tehlike analiz sonuçları ile tutarlı ikişer kuvvetli yer hareketi kayıt takımı seçilmiş ve ölçeklendirilmiştir. Oluşturulan kayıt takımları Türkiye'de bulunan alçak ve orta yükseklikteki sünek betonarme yapıları temsil eden modellere uygulanmış ve bu yapıların deprem davranışı Deprem Etkisi Altında Binaların Tasarımı için Esaslar (2018) uyarınca gerçekleştirilen zaman tanım alanında doğrusal olmayan hesap yönteminin kullanılması ile elde edilmiştir.

Anahtar Kelimeler: Olasılıksal Sismik Tehlike Analizi, Ergodik Yaklaşım

To My Belowed Family…

ACKNOWLEDGEMENTS

First and foremost, I would like to express my sincere and heartfelt gratitude to Assoc. Prof. Dr. Zehra Çağnan Ertuğrul for her invaluable guidance, encouragement, interest, and understanding, which have played a crucial role in bringing about the realization of this study. At the same time, I would like to express my gratitude to Prof. Dr. Murat Dicleli and Assoc. Prof. Dr. Rıza Secer Orkun Keskin for their interest and support.

I would like to extend my sincere thanks to Dr. Sreeram Reddy Kotha for providing a portion of the crucial data used in the thesis study.

I am grateful to my university and high school friends, childhood friends, for the attention, support, and understanding they demonstrated during difficult times. I also thank my close relatives for their support.

I feel fortunate and consider it a debt of gratitude to my private company and colleagues for the opportunities they have provided me to complete my thesis.

And most importantly, I am infinitely grateful to my mother, Nazmiye Çobanyılmaz, who is the primary reason and source of motivation for completing this thesis, as well as to my father, Hayrettin Çobanyılmaz, and my sister, Pınar Çobanyılmaz, for their unwavering patience, understanding, and support, and for the invaluable advice they provided during challenging moments.

TABLE OF CONTENTS

LIST OF TABLES

TABLES

LIST OF FIGURES

FIGURES

LIST OF ABBREVIATIONS

ABBREVIATIONS

AFAD : Disaster and Emergency Management Department,

ASCE SEI41-17: American Society of Civil Enginnering Structural Enginnering Institute,

ATC-40 : Applied Technology Council,

BKS : Building Usage Class,

CP : Collapse Prevention,

DCCP : Diablo Canyon Power Plant,

DD-2 : Gorund motion level, which will be exceeding 50 years with a 10% probability or have a return period of 475 years,

DTS : Earthquake Design Class,

EMME : Earthquake Model of the Middle East,

ESHM2020 : European Seismic Hazard Model 2020,

ESMD2018 : European Strong Motion Dataset 2018,

GMIM : Ground Motion Intensity Measure,

GMPM : Ground Motion Prediction Model,

GP : Gaussian Process,

IO : Immediate Occupancy,

ISDR : Inter Storey Drift Ratio,

ITACA : Italian Accelerometric Archive,

Kik-net : Kiban Kyoshin Network,

K-NET : Kyoshin Network,

LS : Life Safety,

MSE : Mean Squared Error,

NEHRP : National Earthquake Hazards Reduction Program,

NESS : Near Source Strong Motion,

NLME : Non-linear Mixed Effect,

NLTHA : Non-linear Time History Analysis,

PEER : Pacific Earthquake Engineering Research Center,

PGA : Peak Ground Acceleration,

PGV : Peak Ground Velocity,

PSA : Pseudo Spectral Acceleration,

PSHA : Probabilistic Seismic Hazard Asessment,

RESORCE : Refence Database for Seismic Ground-Motion in Europe,

SA : Spectral Acceleration,

SDOF : Single Degree of Freedom,

TBEC18 : Turkey Building Earthquake Code 2018,

TS 498(1997) : Design Loads for Buildings,

TS500,2000 : Requirements for Design and Construction of Reinforced Concrete Structures,

TS ISO 9194(1997) : Bases for Design of Structures; Actions Due to the Self-Weight of Structures, Non-Structural Elements and Stored Materials: Density,

TSMD2014 : Turkish Strong Motion Dataset 2014,

UHS : Uniform Hazard Spectra,

VCM : Varying Coefficient Model,

LIST OF SYMBOLS

SYMBOLS

Δ : Delta

δ : Delta

ε : Epsilon

ϕ : Phi

ρ : Rho

Σ : Summation

τ : Tau

CHAPTER 1

INTRODUCTION

1.1 General

Earthquakes have been a phenomenon to be considered for engineers for many years. It is an important factor to consider for civil engineers, especially when designing buildings, designing underground water and natural gas pipelines, designing important structures such as nuclear power plants, etc. For this reason, while the structures are being designed, the ground-motion intensity parameters that may occur should be predicted as accurately as possible. There are deterministic and probabilistic approaches for estimating these parameters. The most common method utilized for the estimation of such parameters today is the Probabilistic Seismic Hazard Assessment (PSHA) method that was first introduced by Cornell (1968).

PSHA is based on estimating the probabilities of exceeding the order of each strong-motion parameter during the time period of interest within a given area or defined region (Yunatçı, 2007). In PSHA computations, characteristics of regional seismic sources, soil class, regional attenuation of ground-motion intensity measures are used and all of these parameters create a certain degree of ambiguity in the results. The following two terms: aleatory variability and epistemic uncertainty are frequently used to represent this ambiguity. Toro et al. (1997) explained aleatory variability as that 'inherent to the unpredictable nature of future events and cannot be reduced by collection of additional information'. Toro et al. (1997) further described epistemic uncertainty as that 'linked to incomplete knowledge and data about the physics of the earthquake process, which can be reduced theoretically to zero with sufficient knowledge'. By increasing available data, it is possible to reduce epistemic uncertainty thus ambiguity around the PSHA results.

For seismically less active regions, due to scarcity of ground-motion data it is not possible to develop regional ground-motion prediction models (GMPMs). Instead, global GMPMs that are developed based on else where's ground-motion data are used in PSHA of these seismically less active regions. Of course, in the case of such studies the accuracy of the PSHA results is a matter of debate. Today, with increasing station sites at moderately and highly seismic regions, more strong-motion data became available. Chiou and Youngs (2014) and Kale et al. (2015) illustrated that with increasing number of stations recording each major earthquake, it was possible to reduce aleatory variability associated with developed GMPMs which would improve PSHA results' accuracy that are based on these GMPMs. With increasing number of strong-motion records, it became possible to develop site-, source-, path-specific so-called non-ergodic GMPMs. With these prediction models, seismic hazard level at a site can be more accurately estimated and aleatory variability around such estimates can be more accurately quantified.

"An ergodic process is a random process in which the distribution of a random variable in space is the same as the distribution of that same random variable in time at a single point." (Anderson and Brune, 1999). When ergodic GMPMs are utilized as part of seismic hazard assessment studies, an inherent assumption is made, namely that the ground-motion variability obtained based on a global (or regional) dataset is the same as the variability of ground-motion caused by a single-source at a single-site. Over the last decade, the availability of recorded ground motions at single sites caused by multiple earthquakes originating from the same tectonic sources has allowed researchers to develop nonergodic GMPMs and estimate their corresponding standard deviations representing these models' aleatory variabilities. The number of nonergodic GMPMs developed up until now are much limited in comparison to their ergodic counterparts due to considerable amount of data required for their development (i.e., Rodriguez- Marek et al., 2011, Morikawa et al., 2008; Kotha et al., 2022; Lanzano et al. 2017; Ktenidou et al. 2018; Zafarani and Soghrat, 2017; Lin et al., 2011; Villani and Abrahamson, 2015; Kotha et al. 2017, Akkar and

Cagnan, 2019; Landwehr et al., 2016; Lavrentiadis et al., 2021; Campbell et al., 2022, Lavrentiadis et al., 2023; Onder, 2022; Macedo and Liu, 2022)

Utilizing common ergodic GMPMs or state of the art nonergodic GMPMs where available influence the seismic hazard results and hence seismic performance of structures especially when the design of structure under consideration is based on long return period hazard assessment results (Rodriguez- Marek et al., 2014; Abrahamson and Hollenback, 2012; Bommer et al., 2015, Abrahamson et al., 2019; Cagnan, 2021, Kohrangi et al., 2021).

1.2 Literature Review

Many researchers have attempted to develop nonergodic GMPMs for numerous regions. One of the earliest studies in this field was conducted by Chen et al. (2002), where they proposed a new method for developing GMPMs that enables breaking down model variance into its components such as earthquake-to-earthquake, site-to-site and path-to-path. Chen et al. (2002) applied the newly developed method to the Taiwan Strong-motion database. This study classifies site-to-site and path-to-path components of variance as epistemic uncertainty. Whereas, earthquake-to-earthquake component of the variance is envisioned to include both epistemic uncertainty and aleatory variability. As a result, for PGA, ergodic standard deviation was computed to be 0.731; whereas its counterpart partially nonergodic single-station standard deviation was computed to be 0.631. Hence by dropping the ergodic assumption even partially the authors showed that 14% reduction in developed GMPM's standard deviation was possible (Abrahamson et al., 2012).

Another one of the first studies in this regard is Atkinson (2006). In Atkinson (2006) study that was conducted based on the Los Angeles region strong-motion data, it was found that the sigma associated with an individual station is smaller than the regional sigma. The uncertainty in regions containing multiple seismic sources has been tested to generate more uncertainty compared to regions with only a single seismic

source. In Atkinson (2006) study it has been shown that when multiple seismic sources are involved, the value of sigma for a specific site can be reduced by 10%in comparison to regional sigma. However, if the hazard is caused by a single seismic source, the value of sigma for a specific site can be reduced by 40% compared to the regional sigma (Atkinson, 2006). As a result of the Atkinson (2006) study, for PGA, ergodic standard deviation is determined as 0.711 whereas single-station sigma is determined as 0.617. It was observed that the standard deviation can be reduced by 13% if ergodic assumption is excluded even partially (Abrahamson et al., 2012).

Al Atik et al. (2010) first divides ergodic standard deviation or total sigma into its between-event standard deviation (τ) and within-event standard deviation (ϕ) components. The between-events standard deviation is representative of source related factors such as stress drop and variation of slip in space and time that are not considered directly by GMPMs. The within-events standard deviation is representative of influences such as crustal heterogeneities, deeper geological structures, near-surface layering that are too complicated to be modelled by simple distance metric and soil characterization scheme frequently employed in GMPMs. When path-to-path and site-to-site effects can be modelled as part of a nonergodic GMPM, Al Atik et al. (2010) suggests separating path-to-path standard deviation and site-to-site standard deviation from within-events standard deviation and modelling the former two as epistemic uncertainty within a PSHA framework. Similarly, when source-to-source effects are modelled as part of a nonergodic GMPM, Al Atik et al. (2010) suggests separating source-to-source standard deviation from between-events standard deviation and treating source-to-source standard deviation as the third epistemic uncertainty within a PSHA framework.

Morikawa et al. (2008) studied the influence of source-, path- and site-effects on GMPM total sigma based on K-NET and KiK-net strong-motion data. Morikawa et al. (2008) study reduced epistemic uncertainties due to path- and source-effects by only studying ground-motion of events from six narrow areas with similar mechanisms. A correction factor approach was implemented to reduce epistemic uncertainty due to site-effects. Morikawa et al. (2008) results illustrated that

nonergodic sigma is much smaller than its original ergodic counterpart. Morikawa et al. (2008) underlines importance of region specific GMPMs as such have higher accuracies but also mention that region specific GMPMs can only be developed for high seismicity regions with dense strong motion networks.

Lin et al. (2011) quantified nonergodic standard deviation based on strong-motion data from Taiwan. Lin et al. (2011) included systematic source-, site-, and path-effects into their study. Modelling path effects requires a significant amount of data. When there is insufficient data at certain sites to calculate path effects, it has been observed that while aleatory variability decreases, epistemic uncertainty increases considerably. However, in this study, due to the use of a comprehensive database, the single-path standard deviation was shown to be 39% to 47% less of total standard deviation. At the same time, Lin et al. (2011) study also illustrated that the single-site standard deviation can be 9% to 14% less than its counterpart ergodic total standard deviation.Marek et al. (2011) employed an intuitive approach for derivation of a site-specific GMPM from an ergodic GMPM and applied this approach in Marek et al. (2011) to KiK-net data then in Marek et al. (2013) to strong-motion data from other tectonic regions as well. Marek et al. (2011) managed to reduce ergodic standard deviation by 16% by applying site correction. This approach is well-established and has been repeatedly employed in various studies (i.e., Cagnan and Akkar, 2019 to Turkey; Ktenidou et al., 2018 to Greece; Lanzano et al., 2017 to Italy; Zafarani and Soghrat, 2017) and it has been extended by Lanzano et al. (2017) for the derivation of site-and source-specific GMPMs.

In GMPM development, the traditionally used random-effects approach was first introduced by Brillinger and Preisler (1985) and Abrahamson and Youngs (1992) to handle imbalanced strong-motion dataset (i.e., to avoid bias in the predicted median when a dataset features well-recorded atypical earthquakes). Although Abrahamson and Youngs (1992) approach can detect atypical earthquakes, it is not tailored towards detecting atypical sites and estimating the site-to-site variability during regression. Stafford (2014) pointed out shortcomings of this deficiency from a

statistical point of view and suggested a remedy through adopting a non-linear mixed effects approach over random effects approach in GMPM development. Kotha et al. (2017) studied influences of using Stafford (2014) approach instead of Marek et al. (2011) approach by applying them to strong-motion data from Europe and Middle East. Kotha et al. (2017) detected up to 20% reduction in site-to-site standard deviation when Stafford (2014) suggested nonlinear mixed-effects approach is used instead of Marek et al. (2011) approach in development of nonergodic GMPM. Median predictions were also observed to differ, more for less frequently sampled rock sites. Kotha et al. (2022) and Campbell et al. (2022) applied Stafford (2014) nonlinear mixed-effects approach recently to strong-motion data from Europian - Middle Eastern crustal and Japanese subducting tectonic regions, respectively . The GMPM develop by Kotha et al. (2022) is fully nonergodic and includes strong-motion data from Turkey as well. Campbell et al. (2022) conducted a study for the Japanese subduction zone, generating a total of 44 GMPMs using three base models and eight submodels. These models were differentiated based on the inclusion or exclusion of source parameters, forearc and backarc attenuation, type of regression model, ergodicity, distance metrics, etc. Campbell et al. (2022) concluded that the 3E-600 model (where "3" represents the number of the base model, "E" represents the submodel, and "600" represents the maximum distance of rupture) provided the best results.

In recent years, a different approach has started to be used to develop non-ergodic models, distinct from the approach proposed by Stafford (2014). In Landwehr et al. (2016), a new approach called the varying-coefficient model (VCM) approach is introduced. In the VCM approach the coefficients of the components could vary by geographical location, enabling the inclusion of the effects of spatially varying source, path, and site conditions. In this approach, separate sets of coefficients need to be calculated for each location coordinate and source. This implies that individual models need to be developed for each specific location. The problem here is that, due to limited data in close locations, it becomes challenging to create independent models. Therefore, to address this issue, spatial correlations are considered, and the

coefficients are placed into a Gaussian process (GP) (Rasmussen and Williams, 2006) prior to modelling. As a result, separate coefficients are obtained similarly for each region and also the coefficient are continuous throughout study region. In the study, which only used records from California, the aleatory variability was reduced by approximately 40%. This reduction in aleatory variability has a significant impact on high return period hazard calculations. The total standard deviation has decreased from 0.81 to 0.52 in logarithmic units, resulting in approximately a 35% reduction for peak ground acceleration (PGA). Furthermore, in their research for California, Lavrentiadis et al. (2021) used a non-ergodic model created using the same approach as well as the path-effects modelling approach of Dawood and Marek (2013) and reduced the total aleatory standard deviation by approximately 30-40% compared to the ergodic GMPM of Bayless and Abrahamson (2019) . More recently, Macedo et al. (2022) also applied similar approaches to develop a non-ergodic GMPM for the Chile subduction zone.

In today's world, the number of highly sensitive structures such as nuclear power plants, dams, gas pipelines, and others is increasing. This situation necessitates the need for more sensitive PSHA calculations. Studies show that hazard estimations obtained using ergodic GMPMs can underestimate or overestimate the real hazard. The most significant factor in this is the aleatory variability contained in the used ergodic GMPMs. Particularly in the hazard curve, this greatly influences the values of computed ground motion intensity measures caused by low-probability earthquakes. Such low probability large magnitude earthquakes are crucial in the design of sensitive structures. Abrahamson et al. (2012) demonstrated the application of the single-station sigma model for PSHA in their article for the Diablo Canyon Power Plant (DCCP) area located on the Central Coast of California. The calculations were performed using two earthquake records that occurred close to the site and were recorded with DCCP's own recording station. The rupture distances and V_{s30} values of all stations that recorded these two earthquakes were known. Since the distance of DCCP to the epicenters of these two earthquakes is 35 and 85 km, large distance effects were not considered in the calculations. Based on this data, the

site-term has been calculated. As a result, a significant decrease in the hazard prediction was observed using the single-station sigma model. A similar study was conducted for the Thysipunt Nuclear Siting Project in the South African region (Marek et al., 2014). As seismic records were not available in the South African region, the working teams decided to apply a different variation of the hybrid-empirical approach (Campbell,2003). In this approach, a model is created by making seismic modifications to the GMPMs developed for data-rich regions to adapt them for the target region. Within the scope of the project, a type of drilling technique called PS suspension logging was used to thoroughly study the ground characteristics and reduce the aleatory variability in the GMPM. This allowed determination of the shear wave velocity with depth for the entire area. The results showed a significant decrease in the total sigma value, which resulted in a change in the low-frequency hazard curve. The main objective of applying non-ergodic models to PSHA is to transfer the aleatory variability within the model to epistemic uncertainty and reduce the epistemic uncertainty with the help of abundant data or model it by adopting logic tree approach. These results have motivated further increasing research in this area (e.g., Abrahamson et al., 2019, Bommer et al., 2015, Lanzano et al., 2017).

We have discussed the development process of non-ergodic models and the results obtained by applying these models to PSHA. In addition to that, non-ergodic models also have a significant impact on risk analysis. As known, risk is equal to the multiplication of hazard, vulnerability, and exposure components. Changes in these components will alter the amount of risk. Researchers approach the assessment of risk resulting from earthquake hazards from different perspectives. Cagnan (2021) conducted a risk assessment for the İstanbul-Fatih district based on fragility, while Kohrangi (2020) evaluated seismic behaviour using the single degree of freedom (SDOF) structures in their study. These studies will be briefly described below.

Cagnan and Akkar (2019) aimed to reduce the total sigma (σ_{total}) of GMPMs derived for Turkey by partially eliminating the ergodic assumption. For this, they developed event-corrected-single-station standard deviation (ϕ_{SS}) and source-

corrected-between-event standard deviation (τ_{SS}) models. As a result of the study, the total standard deviation decreased by 15% with site correction, while it decreased by 30% with site and source correction, resulting in a more accurate and realistic sigma model for ground-motion prediction (Cagnan and Akkar, 2019). Cagnan (2021) furthered the aforementioned Cagnan and Akkar (2019) study and conducted a study specific to the Istanbul's Fatih district. The scope of Cagnan (2021) is to investigate the effect of ergodic assumption on the economic losses computed for a region. Calculations were made for a deterministic earthquake scenario of magnitude 7.3 on the Marmara Fault. Results indicated that due to the ergodic assumption computed economic losses can be underestimated by 29% with 0.50 probability. This once again emphasizes the importance of the non-ergodic approach.

Kohrangi et al. (2021) conducted a study on this subject, examining the effects of spectra obtained by non-ergodic and ergodic methods on single degree of freedom structures' seismic response. Bindi et al. (2014) and Kotha et al. (2016) GMPMs were used in the study. The response of SDOF systems at 3 different sites were compared. Soil characteristics of selected sites are as following: Site#1 V_{s30}=747 m/s (soft rock); Site#2 V_{s30}=481 m/s (dense soil); Site#3 is V_{s30}= 339 m/s (stiff soil). Differences were observed in the uniform hazard spectra (UHS) representing a return period of 475 years obtained with non-ergodic and ergodic methods. The main reason for this is the use of the site term $\delta S2S_s$ in the non-ergodic method (Kohrangi et al., 2021). The low sigma value of the non-ergodic GMPM does not mean that a lower level of UHS will be obtained than the ergodic method. In some cases, underestimation of the ergodic UHS has also been observed (Kohrangi et al., 2021). Kohrangi et al. (2021) study also reaches the conclusion that relaxing the ergodic assumption does not influence the seismic risk for all building types at a site the same way. Dynamic characteristics of the building type under consideration in relation to the dynamic characteristics of the soil it is sitting on determines the amount of bias introduced.

1.3 Objective and Scope

In this study, Probabilistic Seismic Hazard Assessment (PSHA) is carried out for the Eastern part of Turkey by both employing the traditional ergodic approach and a partially non-ergodic site and source-specific approach. In order to carry out non-ergodic probabilistic seismic hazard assessment, Cagnan and Akkar (2019) study is extended for the Eastern part of Turkey and a source correction term for the Kale et al. (2015) GMPM representing the influence of the Eastern Anatolian Fault as well as the corresponding source-corrected standard deviation are computed. The only other available non-ergodic GMPM available for the Eastern part of Turkey is Kotha et al. (2022) which is also utilized in this study in order to carry out non-ergodic PSHA for the Eastern part of Turkey. For four selected station sites located in Turkey under the predominant influence of Eastern Anatolian Fault, seismic hazard is estimated using both the traditional ergodic approach and partially non-ergodic approach. For each site, the ergodic and non-ergodic PSHA estimates are utilized to select and scale two sets of hazard consistent ground-motion records by following the Turkish Design Principles for the Buildings Subjected to Earthquakes (2018). These ground-motion record sets are employed to estimate the seismic response of eight ductile reinforced concrete structures representing the low- to mid-rise buildings in Turkey. These representative building models are designed within the scope of this study according to the Turkish Design Principles for the Buildings Subjected to Earthquakes (2018). The seismic responses of these structures are estimated by performing nonlinear time history analysis on 3D structural models again by following the Turkish Design Principles for the Buildings Subjected to Earthquakes (2018). Based on the analyses results the influence of the ergodic assumption on seismic risk is assessed.

CHAPTER 2

DESIGN OF THE MODEL BUILDINGS ACCORDING TO TBEC2018

2.1 General Design Criteria of Models

The selected seismic records that are consistent with the ergodic probabilistic seismic hazard assessment (PSHA) and partially non-ergodic PSHA results will be applied to 2 different types of buildings that are modelled in Sap2000 software (Computers and Structures, Inc. v21.1.0). This chapter is devoted to explaining details of design of these buildings and then development of their structural models in Sap2000 will be explained in chapter 6.

Firstly, the buildings under consideration are reinforced concrete residential type and were designed according to the 2019 Building Earthquake Code of Turkey (TBEC, 2018) and Requirements for Design and Construction of Reinforced Concrete Structures (TS500,2000). Two different buildings in terms of height and bearing system dimensions were modelled in order to study the influence of different dynamic building characteristics on seismic performance when imposed hazard is computed both ergodically and non-ergodically. It is assumed that the buildings are located at the 4 strong-motion station sites in and around the province of Elazığ, close to the Eastern Anatolian Fault Zone. The geometrical, structural and usage information of these buildings are explained below.

One of these buildings was designed to have three spans in the longitudinal X-direction and a single span in the lateral Y-direction, each having a span spacing of 5 m. In the vertical Z-direction, there is a single storey and the selected floor height is 3 m (Figure 2.1a). The second building type has the same floor plan as the first building type but with different column dimensions. Another difference is in the vertical Z-direction. The second building type was designed to have five stories and

the selected floor height is again 3 m (Figure 2.1b). The total heights of the buildings are 3 m and 15 m, respectively.

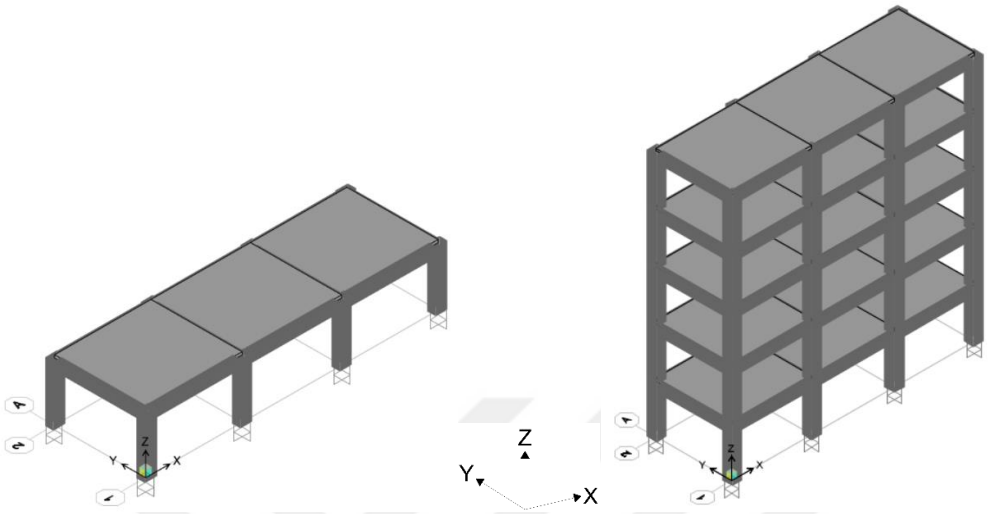

(a) (b)

Figure 2.1 Mathematical models of the selected archetypes corresponding to (a) low-rise and (b) mid-rise reinforced concrete buildings.

The chosen building type and dimensions statistically represent the category of school buildings found in Turkey. However, within the scope of this study, they have been treated as residential buildings, and all calculations have been conducted accordingly.

In terms of the height of the modelled buildings, one of the models is classified as a "low-rise building," and the other is classified as a "mid-rise building" according to the 2019 Building Earthquake Code of Turkey (Table 3.3 TBEC, 2018). The low-rise model building height class is BYS=8, the mid-rise model building height class is BYS=6. These classes are presented in Table 2.1 below.

Table 2.1 According to Building Height Classes and Earthquake Design Classes Defined Building Height Ranges (Table 3.3 TBEC, 2018)

Building Height Classes	According to Building Height Classes and Earthquake Design Classes Defined Building Height Ranges [m]		
	DTS=1, 1a, 2, 2a	DTS= 3, 3a	DTS= 4, 4a
BYS=1	$H_N > 70$	$H_N > 91$	$H_N > 105$
BYS=2	$56 < H_N \leq 70$	$70 < H_N \leq 91$	$91 < H_N \leq 105$
BYS=3	$42 < H_N \leq 56$	$56 < H_N \leq 70$	$56 < H_N \leq 91$
BYS=4	$28 < H_N \leq 42$	$42 < H_N \leq 56$	
BYS=5	$17{,}5 < H_N \leq 28$	$28 < H_N \leq 42$	
BYS=6	$10{,}5 < H_N \leq 17{,}5$	$17{,}5 < H_N \leq 28$	
BYS=7	$7 < H_N \leq 10{,}5$	$10{,}5 < H_N \leq 17{,}5$	
BYS=8	$H_N \leq 7$	$H_N \leq 10{,}5$	

Since the modelled buildings are designed as residential structures, the building usage class (BKS) is determined as BKS=3, and the buildings' importance coefficient (I) is determined as I=1.0 according to Table 3.1 of TBEC (2018). This data is presented in Table 2.2 below.

Table 2.2 Building Usage Classes and Importance Factors (Table 3.1 of TBEC, 2018)

Building Usage Class	Purpose of Usage	Importance Factor [I]
BKS=1	**Buildings that need to be used after an earthquake, buildings where people are present for a long time and intensely, buildings where valuables are kept, and containing dangerous materials** a) Buildings that must be used immediately after an earthquake (Hospitals, dispensaries, health centers, fire brigade buildings and facilities, PTT and other communication facilities, transportation stations and terminals, energy production and distribution facilities; province, district governorship and municipality administration buildings, first aid and disaster planning stations) b) Schools, other educational buildings and facilities, dormitories and hostels, military barracks, prisons, etc. c) Museums d) Buildings that containing or storing toxic, explosive and flammable materials, etc.	1,5

Table 2.2 (Cont'd)

BKS=2	**Buildings where people are present intensively for a short time** Malls, sport facilities, cinema, theatre and concert halls, temple etc.	1,2
BKS=3	**Other Buildings** Buildings that are not included in the definitions given for BKS=1 and BKS=2 (Residential and office buildings, hotels, building type industrial structures, etc.)	1,0

Additionally, it is necessary to determine the buildings' earthquake design class (DTS). According to TBEC(2018) S_S (Short period map spectral acceleration coefficient) and building usage class values must be determined in order to select the DTS. BKS value was determined as 3 for both models. The S_S value depends on the location of the building under consideration as well as ground-motion level adopted for design (i.e. DD-2 that represents ground-motion level, which will be exceeded in 50 years with a 10% probability or have a return period of 475 years). The different S_S values obtained through the AFAD (Disaster and Emergency Management Department) website (https://tdth.afad.gov.tr/TDTH/main.xhtml) are given in Table 2.3 below.

Table 2.3 Soil and Ground Motion Parameters According to Location of Stations

Station ID	Latitude	Longitude	Earthquake Ground Motion Level	Local Soil Type	S_S	S_1	F_S	F_1	PGA [g]	PGV [cm/sn]
2301	38,6704	39,1926	DD-2	ZC	0,912	0,257	1,20	1,50	0,383	23,91
2302	38,3923	39,6754	DD-2	ZB	1,148	0,306	0,90	0,80	0,478	28,57
2304	38,7209	39,8629	DD-2	ZC	1,533	0,409	1,20	1,50	0,630	43,73
2307	38,6958	39,9319	DD-2	ZD	1,584	0,420	1,00	1,88	0,653	47,95

S_1(T=1 sec. map spectral acceleration coefficient), another spectral acceleration value like S_{DS}, was also obtained from the AFADs' website. Corresponding S_{DS} and S_{D1} values were calculated using the site coefficients of tables 2.4 and 2.5 below as well as Equations 2.1 and 2.2.

Table 2.4 Site Coefficient at Short Period

Site Class	Site Coefficient at Short Period, F_S					
	Ss≤0,25	Ss = 0,50	Ss = 0,75	Ss = 1,00	Ss = 1,25	Ss = 1,50
ZA	0,80	0,80	0,80	0,80	0,80	0,80
ZB	0,90	0,90	0,90	0,90	0,90	0,90
ZC	1,30	1,30	1,20	1,20	1,20	1,20
ZD	1,60	1,40	1,20	1,10	1,00	1,00
ZE	2,40	1,70	1,30	1,10	0,90	0,80
ZF	Site -specific soil behaviour analysis will be performed.					

Table 2.5 Site Coefficient for 1,00 sec. Period

Site Class	Site Coefficient for 1,00 sec. Period,F_1					
	S_1≤0,10	S_1 = 0,20	S_1 = 0,30	S_1 = 0,40	S_1 =0,50	S_1 = 0,60
ZA	0,80	0,80	0,80	0,80	0,80	0,80
ZB	0,80	0,80	0,80	0,80	0,80	0,80
ZC	1,50	1,50	1,50	1,50	1,50	1,40
ZD	2,40	2,20	2,00	1,90	1,80	1,70
ZE	4,20	3,30	2,80	2,40	2,20	2,00
ZF	Site -specific soil behaviour analysis will be performed.					

$$S_{DS} = S_S \,.\, F_S \tag{2.1}$$

$$S_{D1} = S_1 \,.\, F_1 \tag{2.2}$$

Table 2.6 Short Period and 1,00 sec. Period Design Spectral Acceleration Coefficients

Station ID	S_{DS}	S_{D1}
2301	1,094	0,386
2302	1,033	0,245
2304	1,840	0,613
2037	1,584	0,790

Then, the earthquake design class was chosen as DTS=1 for all buildings under consideration according to TBEC (2018) as shown in Table 2.7 below. Thus, it has been determined that the buildings are located in the region with the highest earthquake risk.

Table 2.7 Earthquake Design Classes (Table 3.2 of TBEC, 2018)

Short Period Design Spectral Acceleration Coefficient in DD-2 Earthquake Ground Motion Level (S_{DS})	Building Usage Class	
	BKS=1	BKS=2,3
S_{DS} < 0.33	DTS=4a	DTS=4
0.33 ≤ S_{DS} < 0.50	DTS=3a	DTS=3
0.50 ≤ S_{DS} < 0.75	DTS=2a	DTS=2
0.75 ≤ S_{DS}	DTS=1a	DTS=1

The horizontal elastic design acceleration spectra constructed according to TBEC (2018) for 4 different strong-motion station sites selected are given in Figure 2.2. These spectra were used for hazard consistent earthquake record selection for nonlinear time history analyses to be carried out.

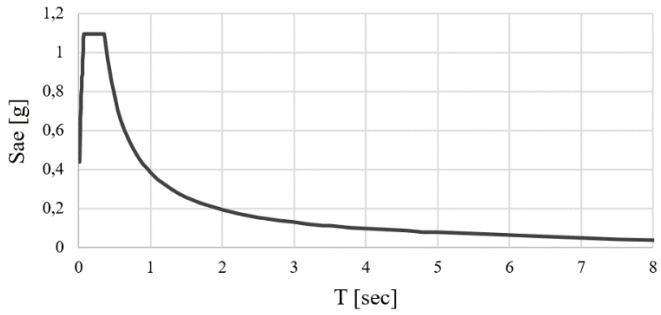

a)

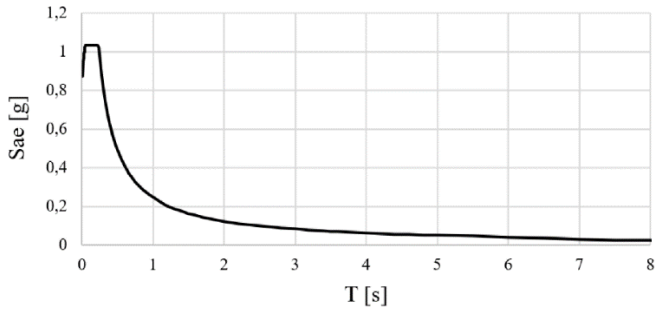

b)

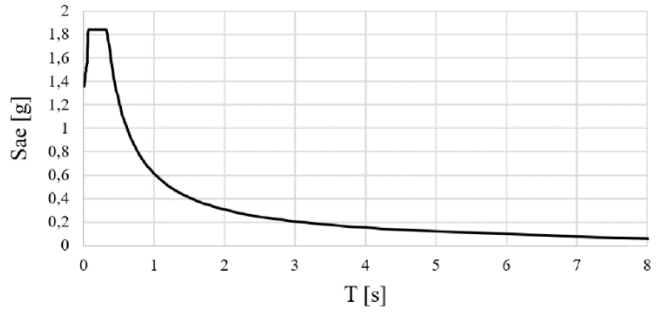

c)

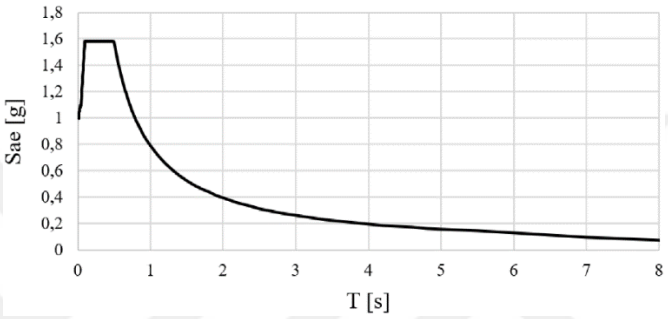

d)

Figure 2.2 Horizontal Elastic Design Spectrum of Low & Mid-rise Buildings in a) 2301 Station Location b) 2302 Station Location c) 2304 Station Location d) 2307 Station Location

2.2 General Structural Properties

In both models (i.e. low-rise and high-rise buildings) floor area of buildings is approximately 75 m^2. There is no torsional irregularity, as the building is symmetrical in both directions. Discontinuities in floors or projections in floors do not exist in both models. On each floor columns, beams, and slabs are designed with the same material properties and dimensions. Therefore, there are no weak story and soft story irregularities. In addition, there are no discontinuities in the bearing elements. The typical floor plans are presented in Figure 2.3. for both models. 5% eccentricity will be given to the horizontal loads acting on the models, so the torsional movement of buildings will be observed under applied earthquake records.

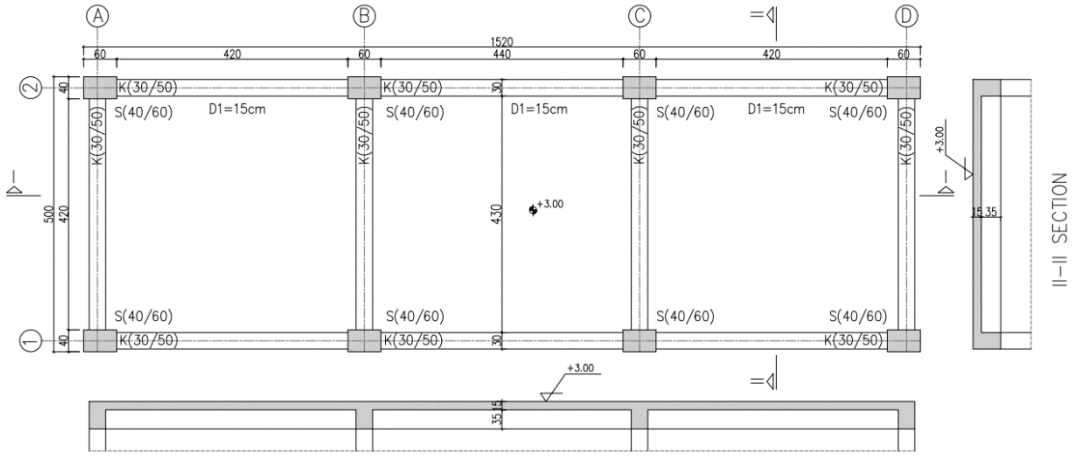

a)

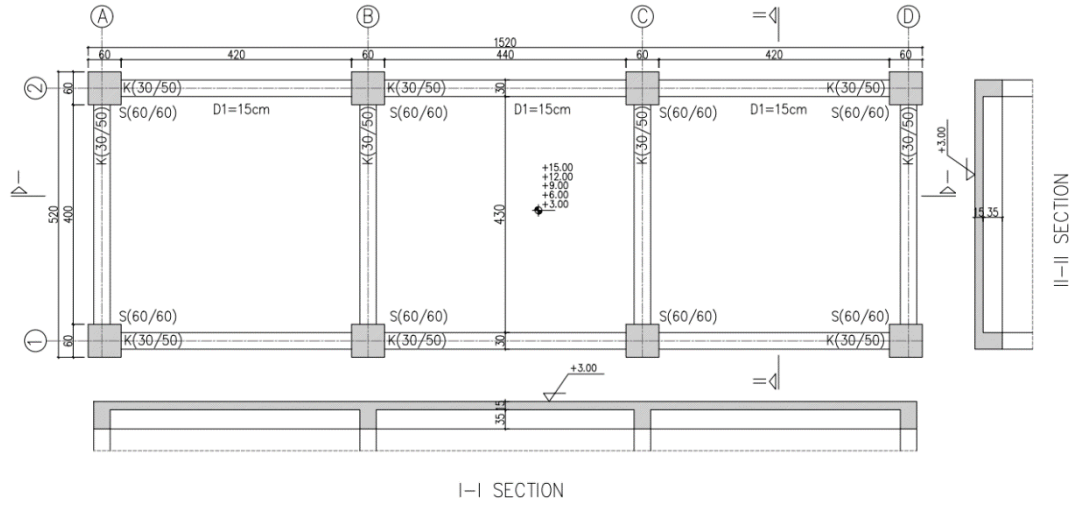

b)

Figure 2.3 The typical floor plan of (a) low-rise building (b) mid-rise building

2.2.1 Design of the Models

According to the TBEC (2018) regulations, performance targets have been established for model buildings based on their height class, earthquake design class, and earthquake ground motion level (Table 2.8). Consequently, the selected ground motion level is DD-2. The design target performance level for this study is controlled damage (KH in TBEC, 2018). Achieving this level of performance holds significant importance when constructing structural system components to guarantee the safety

of human life, as it corresponds to a level of damage that is typically non-critical and can be easily repaired. In order to accomplish this objective, strength based design principles were adopted in this study. The buildings were modelled using the Sap2000 program, and through response spectrum analyses, it was confirmed that the sections fulfilled the demand/capacity ratios required by the TBEC (2018).

Table 2.8 Performance Targets and Design Approaches for New or Existing Reinforced Concrete Building According to Earthquake Design Class

Ground Motion Level	DTS=1,1a,2,2a,3,3a,4,4a		DTS=1a,2a	
	Normal Performance Level	Design Approach	Advanced Performance Level	Design Approach
DD-3	-	-	SH	ŞGDT
DD-2	KH	DGT	KH	DGT
DD-1	-		KH	ŞGDT

The buildings were designed as reinforced concrete frame systems. In the developed models, only column and beam elements were used as the bearing system of the structure, and shear walls were not included. The load-bearing system (column, beam, and slab) dimensions were selected according to TS500(2000) and TBEC (2018) to provide minimum cross-sectional dimensions. For the beams, the cross-sectional dimensions were selected as 30 cm x 50 cm, provided that the body width is a minimum of 250 mm, the beam height is not less than three times the floor thickness, and 300 mm (Figure 2.4) and the floor thickness is chosen as 15 cm to meet minimum 12 cm floor thickness. For ease of analysis, the in-plane deflection of the floor slab is neglected; that is, the floors are considered to behave as rigid diaphragms.

The concise summary given above on determination of beam cross-sectional dimensions can be found in TS500 (2000) section 7.3 and TBEC (2018) section 7.4.1. The minimum ratio of beam longitudinal reinforcements is calculated according to equation 2.3 (Eq 7.8 of TBEC, 2018).

$$\rho \geq 0.8 f_{ctd} / f_{yd} \tag{2.3}$$

ρ in the above equation is the ratio of the top or bottom tension reinforcement at the beam supports; f_{ctd} represents design tensile strength; f_{yd} represents the design yieldstrength of the longitudinal reinforcement. Transverse reinforcement criteria and specifications for their spacing and cover requirements are given in the relevant sections of TBEC, 2018 and TS500, 2000. (i.e. sections 7.4.3 and 7.4.4 in TBEC, 2018).

Another important check for beams is shear safety. Control was provided according to Equation 2.4 (i.e. Eq 7.9 in TBEC, 2018).

$$V_e = V_{dy} \pm (M_{pi} + M_{pj})/l_n \tag{2.4}$$

V_e in this equation is the shear force used in the transverse reinforcement calculation, V_{dy} represents simple beam shear force consisting of loads not multiplied by load coefficients, M_{pi}, M_{pj} represents positive or negative moment capacity at the left and right ends of the beam, respectively, l_n represents free span of the beam. Selected beam reinforcements are shown in Figures 2.4.

Since the minimum column dimensions are determined as 30 cm x 30 cm according to TBEC (2018), the selected dimensions of the column elements are chosen as 60 cm x 60 cm for mid-rise building and 40 cm x 60 cm for low-rise building (Figure 2.5). For the column sections, the checks specified in both regulations and which are provided below are applied.

$$N_d \leq 0{,}9\, f_{cd} A_c \tag{2.5}$$

$$N_{dm} \leq 0{,}4\, f_{ck} A_c \tag{2.6}$$

N_d above is the design axial force, f_{cd} represents design compression strength of concrete, A_c represents the entire cross-sectional concrete area of the element under consideration in Equations 2.5 and 2.6 (i.e., Eq. 7.7 in TS500, 2000). N_{dm} is the largest of the calculated axial compressive forces under the effect of vertical loads and earthquake loads, f_{ck} represent characteristic cylindrical compressive strength

of concrete in Equation 2.6 (i.e., section 7.3.1.2 of TBEC18). In addition, the conditions specified in Equations 2.7, 2.8 and 2.9 (i.e., Eqs. 7.8,7.9 and 7.10 in TS500, 2000) are provided for column longitudinal reinforcements.

$$\rho_t = A_{st}/A_c \geq 0.01 \tag{2.7}$$

$$\rho_t \leq 0.04 \tag{2.8}$$

$$\rho_t \leq 0.06 \tag{2.9}$$

ρ_t in the Equation 2.7 is the total longitudinal reinforcement ratio in the columns, A_{st} denotes the total cross-sectional area of the column longitudinal reinforcement. Equation 2.8 expresses the maximum area of the longitudinal reinforcement that can be in the section, while Equation 2.9 shows the maximum area of the reinforcement in the overlap zones. The transverse reinforcement criteria and reinforcement locations in the columns have been chosen in accordance with the relevant sections of both regulations (i.e., 7.3.2, 7.3.3 in TBEC, 2018) and the capacity values computed based on response spectrum analyses. Column reinforcements are shown in Figure 2.5.

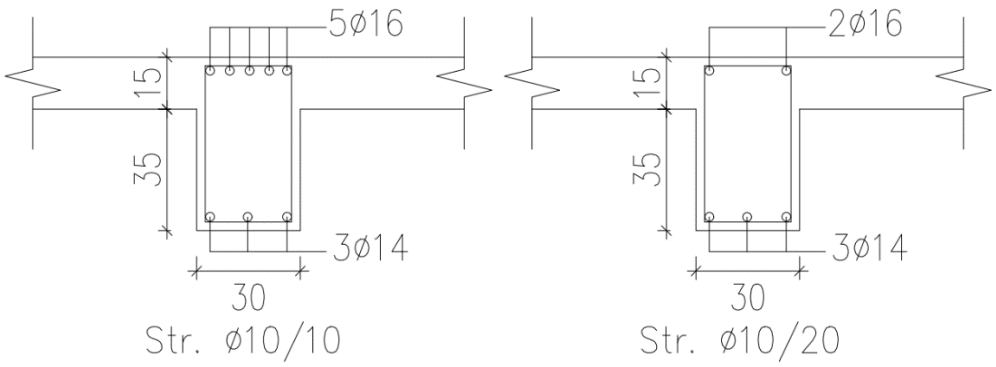

a) Cross-sections of beams in the X direction for the 1st,2nd and 3rd floors of the mid-rise building.

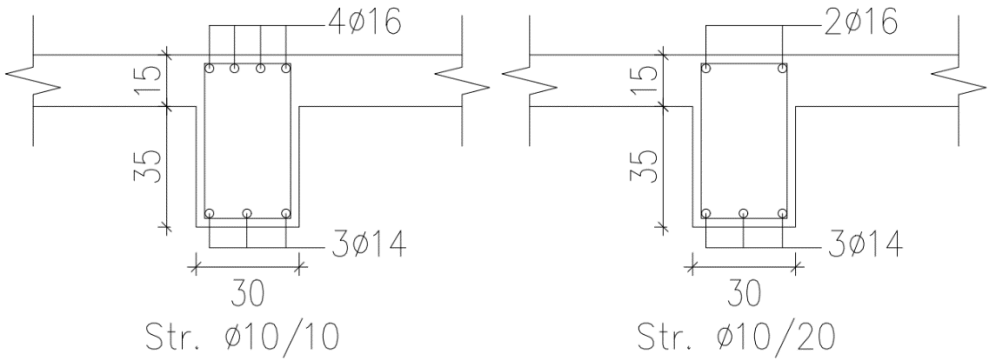

b) Cross-sections of beams in the X direction for the 4th floors of the mid-rise building.

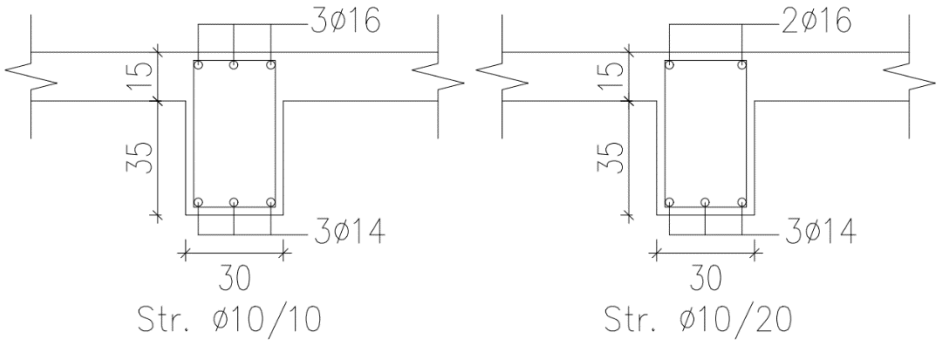

c) Cross-sections of beams in the X direction for the 5th floor of the mid-rise and 1st floor of the low-rise building.

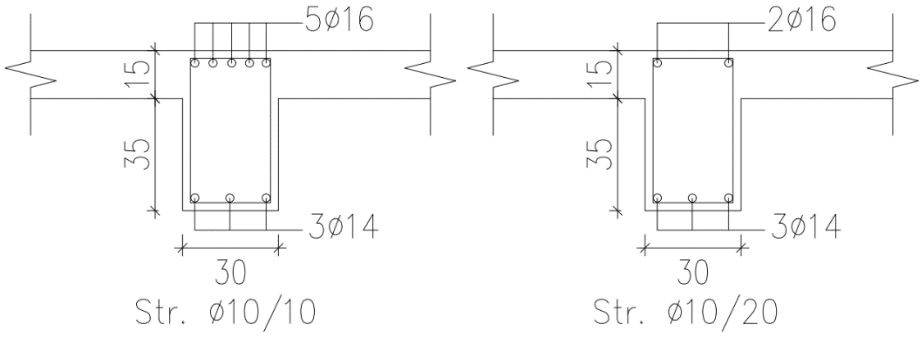

d) Cross-sections of beams in the Y direction for the 1st,2nd,3rd,4th floors of the mid-rise building.

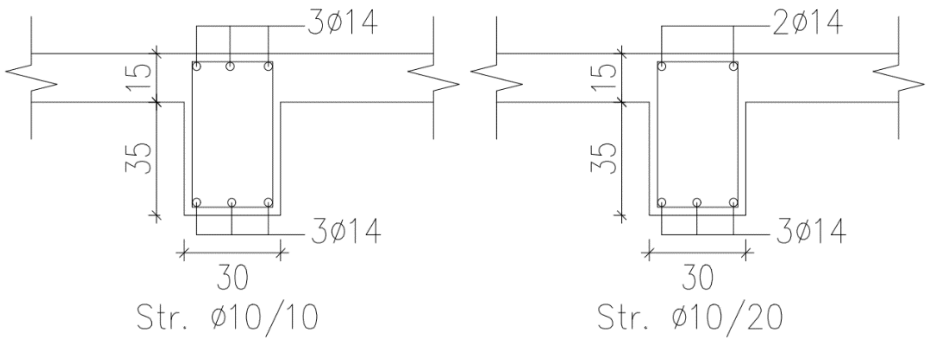

e) Cross-sections of beams in the Y direction for the 5th floors of the mid-rise and 1st floor of the low-rise buildings.

Figure 2.4 Typical beam cross-sections (The cross-section on the left side is confinement zone, on the right side is middle zone of the beam)

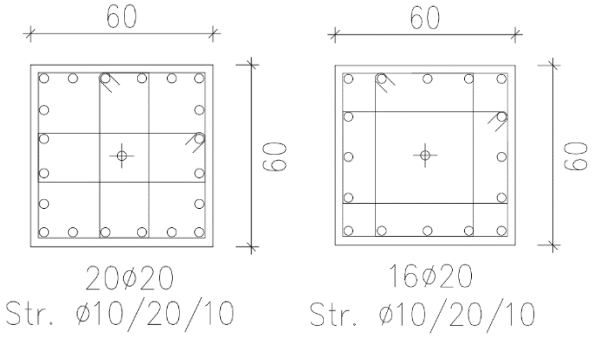

a) Cross-section of columns for the mid-rise building (The cross-section on the left side is for 1st and 2nd floors, on the right side is for 3rd,4th and 5th floors).

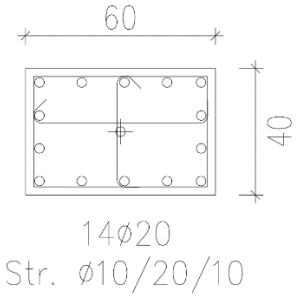

b) Cross-section of columns for the low-rise building.

Figure 2.5 Typical column cross-section

When selecting the structural system reinforcements, the design was made, and the reinforcements were determined under the combinations of the earthquake loading, the figures of which are provided above (Figure 2.2), and dead & live loads.

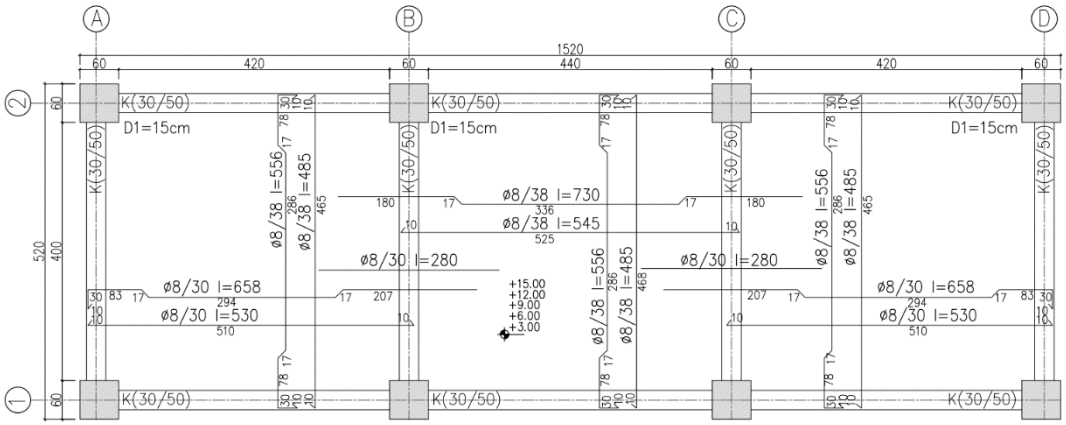

Figure 2.6 Typical static floor plan for mid/low-rise buildings type.

Eigenvalue analyses in Sap2000 were also conducted within the scope of this study. The computed periods and mode shapes of the buildings are provided in a Figure 2.7. According to TBEC (2018), the total sum of modal effective masses for base shear force, computed separately for each mode in the earthquake directions (X) and (Y), must be at least 95% of the building's total mass (Eq. 2.10). Related values are presented in Tables 2.9 and 2.10.

$$\sum_{n=1}^{\mathrm{YM}} m_{txn}^{(X)} \geq 0.95 m_t \quad ; \quad \sum_{n=1}^{\mathrm{YM}} m_{tyn}^{(Y)} \geq 0.95 m_t \qquad (2.10)$$

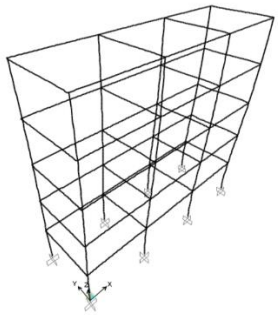	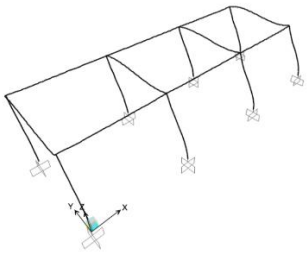
Mode 1 ; T= 0,578495 sec	Mode 1 ; T= 0,120749 sec
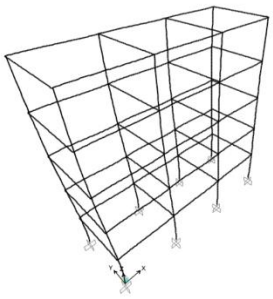	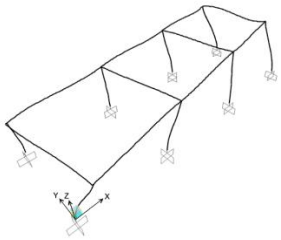
Mode 2 ; T= 0,545734 sec	Mode 2 ; T= 0,092578 sec
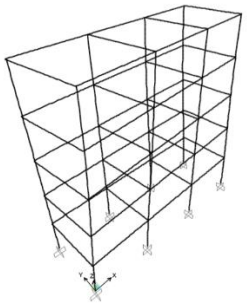	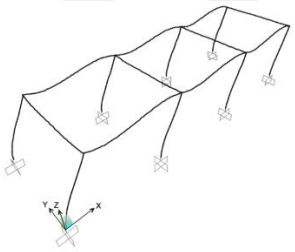
Mode 3 ; T= 0,468186 sec	Mode 3 ; T= 0,089808 sec
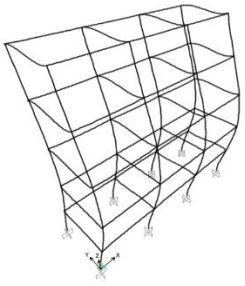	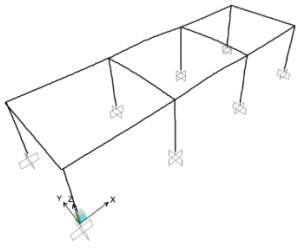
Mode 4 ; T= 0,168214 sec	Mode 4 ; T= 0,079375 sec

Figure 2.7 (Cont'd)

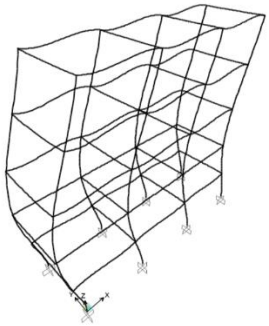	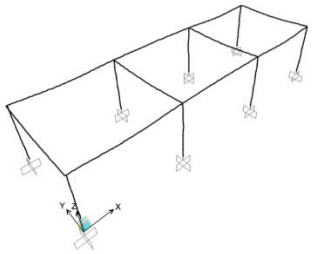
Mode 5 ; T= 0,161203 sec	Mode 5 ; T= 0,077413 sec
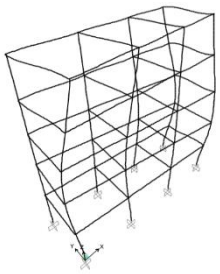	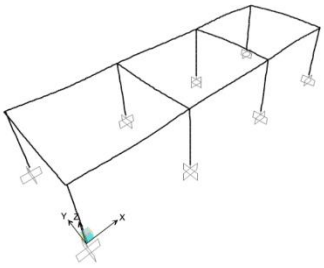
Mode 6 ; T= 0,138531 sec	Mode 6 ; T= 0,077286 sec
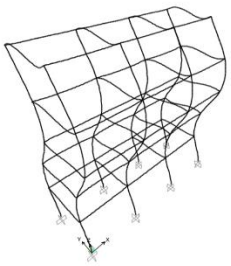	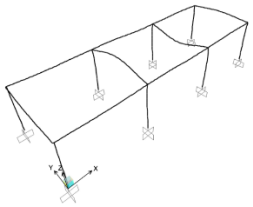
Mode 7 ; T= 0,084259 sec	Mode 7 ; T= 0,042896 sec
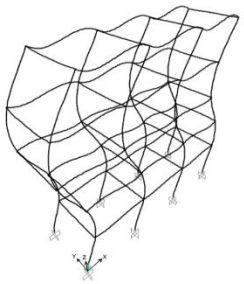	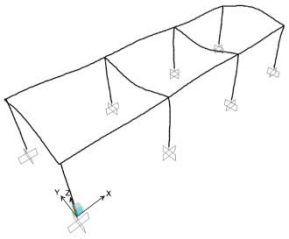
Mode 8 ; T= 0,082282 sec	Mode 8 ; T= 0,040803 sec

Figure 2.7 Periods and Mode shapes of Low and Mid-rise buildings

Table 2.9 Modal Participating Mass Ratios (Mid-rise Model)

Modal Participating Mass Ratios (Mid-rise Model)				
StepType	Period	SumUX	SumUY	SumRZ
Mode 1	0,578495	0	0,78891	0
Mode 2	0,545734	0,79571	0,78891	0
Mode 3	0,468186	0,79571	0,78891	0,79529
Mode 4	0,168214	0,79571	0,91109	0,79529
Mode 5	0,161203	0,91272	0,91109	0,79529
Mode 6	0,138531	0,91272	0,91109	0,91257
Mode 7	0,084259	0,91272	0,96273	0,91257
Mode 8	0,082282	0,96273	0,96273	0,91257

Table 2.10 Modal Participating Mass Ratios (Low-rise Model)

Modal Participating Mass Ratios (Low-rise Model)				
StepType	Period	SumUX	SumUY	SumRZ
Mode 1	0,120749	0	0,99653	0
Mode 2	0,092578	0	0,99653	0,99535
Mode 3	0,089808	0,98710	0,99653	0,99535
Mode 4	0,079375	0,98710	0,99653	0,99535
Mode 5	0,077413	0,98710	0,99653	0,99535
Mode 6	0,077286	0,99126	0,99653	0,99535
Mode 7	0,042896	0,99126	0,99653	0,99535
Mode 8	0,040803	0,99126	0,99653	0,99535

In the subsequent section, the methods of Ground Motion Prediction Models (GMPM) to be employed in calculating seismic forces for the buildings described in the thesis's relevant section and outlined above will be elucidated. This will include an account of the previous applications of GMPM methods in Turkey and the determination of GMPM parameters to be applied within the scope of this study.

CHAPTER 3

REGION-AND SITE-SPECIFIC GMPMs APPLICABLE FOR TURKEY

Within the scope of this study, Kale et al. (2015) GMPM which was regionalized for the North Anatolian Fault Zone and for which δS2S parameters were computed for selected station sites within the scope of the Cagnan and Akkar (2019) study and Kotha et al. (2022) region and site-specific GMPMs were used. In the first section of this chapter, these models are introduced and compared. In the second section of this chapter, Cagnan and Akkar (2019) study is extended for the East Anatolian Fault Zone and for the 3 additional station sites that are within the scope of this study.

3.1 Comparison of Region- and Site-specific GMPMs Applicable for Turkey

Kotha et al. (2016) based on the RESORCE pan-European strong motion dataset (Akkar et al., 2014) developed a new ground-motion prediction model (GMPM) that adopted the relatively simple functional form of Bindi et al. (2014) but uses a non-linear mixed effect regression that can estimate regional differences as random effects applied to different model parameters.

$$\ln(GM) = e_1 + F_D(R_{JB}, M_w) + F_M(M_w) + \delta B_e + \delta B_S + \varepsilon \tag{3.1}$$

$$F_D(R_{JB}, M_w) = \left[c_1 + c_2(M_w - M_{ref})\right] ln\left(\frac{\sqrt{{R_{JB}}^2 + h^2}}{R_{ref}}\right) + (c_3 + \Delta c_{3,r})\left(\sqrt{{R_{JB}}^2 + h^2} - R_{ref}\right) \tag{3.2}$$

$$F_M(M_w) = \begin{cases} b_1(M_w - M_h) + b_2(M_w - M_h)^2 & for\ M_w < M_h \\ b_3(M_w - M_h) & for\ M_w \geq M_h \end{cases} \tag{3.3}$$

$$\delta B_S = (g_1 + \Delta g_{1,r}) + (g_2 + \Delta g_{2,r}) \ln(V_{S30}) + \delta_{S2S} \tag{3.4}$$

In Equations 3.1 to 3.4, M_w represents moment magnitude, R_{JB} represents Joyner and Boore distance, M_h is 6.75, M_{ref} is 5.5, R_{ref} is 1km, e_1 is the global off-set parameter, F_D and F_M are the distance and magnitude components, δB_e and δB_s are random effects on e_1 describing the between-event and between-station variability, ε is the residual distribution representing aleatory variability, δ_{S2S} is the systematic deviation of recordings for individual station with respect to the model. δB_e is a normally distributed random variable with mean zero and standard deviation τ (between-event variability), δ_{S2S} is a normally distributed random variable with mean zero and standard deviation ϕ_{S2S} (between-station variability), ε is a normally distributed random variable with mean zero and standard deviation ϕ_o (aleatory variability). Kotha et al. (2016) actually starts with a large dataset but through regionalization develops separate GMPMs for Turkey and Italy. τ therefore is not fully source-corrected between-event standard deviation of Cagnan and Akkar (2019) study. ϕ_{S2S} is site-to-site variability of Cagnan and Akkar (2019) study. Kothe et al. (2016) do not adopt a style-of-faulting term as well as does not consider nonlinear site amplification effects. The developed GMPMs are applicable for M_w:4.0-7.6, V_{S30}:180-1000 m/s and R_{JB} <200km ranges. The suggested GMPMs cannot be categorized as partially nonergodic from the point of view of Cagnan and Akkar (2019) study.

Figure 3.1 compares Kotha et al. (2016) suggested response spectra for Turkey with Kale et al. (2015) suggested response spectra. For the two magnitudes considered and for periods less than 0.2s and R_{JB}>10km, Kotha et al. (2016) suggested pseudo spectral acceleration values (PSA) exceed Kale at al. (2015) suggested PSA values. For R_{JB}<10km, the difference between Kotha et al. (2016) and Kale et al. (2015) response spectra is larger and exists throughout the whole period range considered.

Figure 3.2 compares the distance scaling of Kotha et al. (2016) GMPM for Turkey and that of Kale et al. (2015) GMPM. The comparisons are given for magnitudes ranging between M_w 4 and 7. The chosen spectral ordinates are PGA and PSA at T: 0.2s, T: 1:0s, and T: 3:0s. The median trends in Figure 3.2 are computed for reference rock (V_{S30}: 800 m/s) conditions. The faulting mechanism is strike-slip. There is a good match between estimated spectral ordinates of two GMPMs except for near-

fault regions. The distance-dependent decay rates suggested by Kotha et al. (2016) and Kale et al. (2015) GMPMs are also similar except for M_w:4.0 and M_w:5.0 events: a more gradual decay is observed in the case of Kale et al. (2015) GMPM. Figure 3.2 also provide visual information about magnitude scaling of two GMPMs. The magnitude saturation is more apparent in the case of Kotha et al. (2016) GMPM in comparison to Kale et al. (2015) GMPM especially for PGA and PSA at T: 0.2s. Aleatory variability models suggested by Kotha et al. (2016) are comparable to those suggested by Kale et al. (2015) for a large magnitude scenario and lower than those suggested by Kale et al. (2015) for a moderate magnitude scenario.

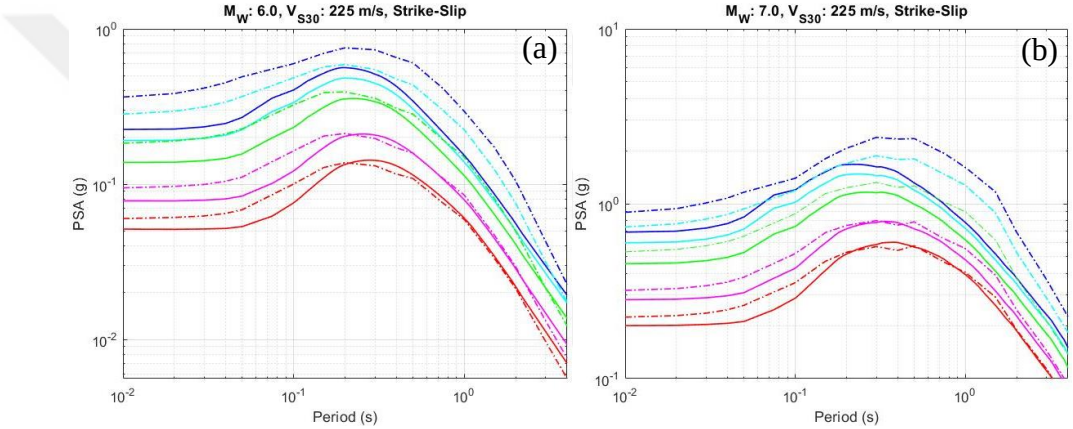

Figure 3.1 Comparison of Kotha et al. (2016) suggested response spectra (represented by dash-dot lines) with Kale et al. (2015) suggested response spectra (represented by solid lines) for Turkey for strike-slip, M_w: 6.0 and 7.0, V_{S30}: 225 m/s, R_{JB}: 1km (represented by dark blue line), 5km (represented by light blue line), 10km (represented by green line), 20km (represented by pink line) and 30km (represented by red line) scenarios. (a) gives median response spectra, (b) gives median+1.0sigma response spectra.

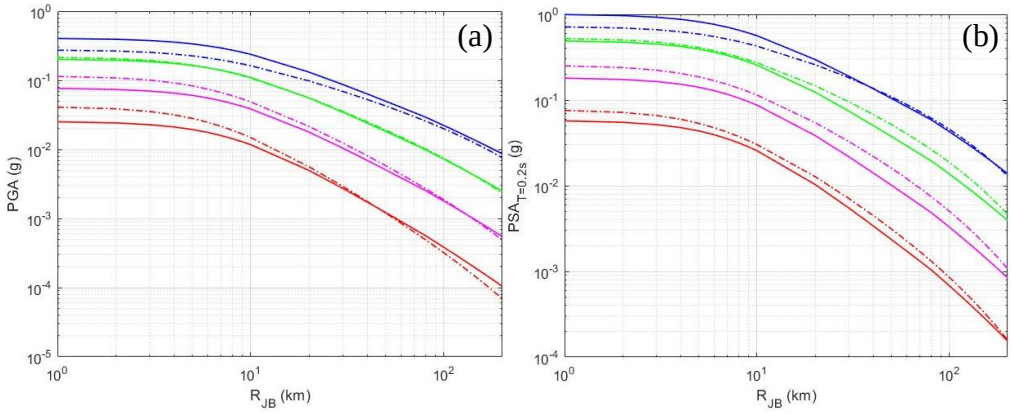

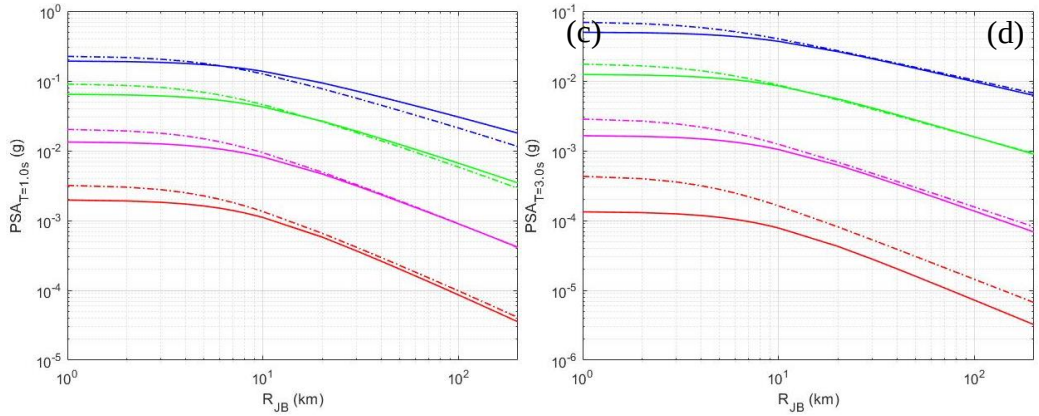

Figure 3.2 Comparison of Kotha et al. (2016) suggested GMPM (represented by dash-dot lines) with Kale et al. (2015) suggested GMPM (represented by solid lines) for Turkey for strike-slip, M_w: 4.0 (represented by red line), 5.0 (represented by pink line), 6.0 (represented by green line) and 7.0 (represented by dark blue line), V_{S30}: 800 m/s scenarios. (a) gives variation of PGA with R_{JB}, (b) gives variation of PSA at T=0.2s with R_{JB}, (c) gives variation of PSA at T=1.0s with R_{JB}, (d) gives variation of PSA at T=3.0s with R_{JB}.

Kotha et al. (2020) suggested a new GMPM capable of predicting the 5% damped RotD50 of PGA, PGV, and SA(T=0.01-8s) from shallow crustal earthquakes of $3 \leq M_w \leq 7.4$ occurring $0 < R_{JB} \leq 545$km away from sites with $90 \leq V_{S30} \leq 3000$ m/s based on the new European Strong-Motion database (Lanzano et al., 2018). Kotha et al. (2020) suggested GMPM is a true partially nonergodic GMPM capable of considering source as well as site effects. For the model development, 18,222 records from 927 events monitored by 1829 stations are used. In comparison to Kotha et al. (2016) more data was available to Kotha et al. (2020). The suggested GMPM is given below:

$$\ln(GM) = e_1 + F_{R,g}(R_{JB}, M_w) + F_{R,a}(R_{JB}) + F_M(M_w) + \delta B^0_{e,l} + \delta L2L_l + \delta S2S_S + \delta c_{3,r} + \varepsilon \quad (3.5)$$

$$F_{R,g}(R_{JB}, M_w) = [c_1 + c_2(M_w - M_{ref})] ln\left(\sqrt{\frac{({R_{JB}}^2 + h_D^2)}{({R_{ref}}^2 + h_D^2)}}\right) \quad (3.6)$$

$$F_{R,a}(R_{JB}) = \left(\frac{c_3}{100}\right)\left(\sqrt{{R_{JB}}^2 + h_D^2} - \sqrt{{R_{ref}}^2 + h_D^2}\right) \quad (3.7)$$

$$F_M(M_w) = \begin{cases} b_1(M_w - M_h) + b_2(M_w - M_h)^2 \; for \; M_w \leq M_h \\ b_3(M_w - M_h) \qquad\qquad\qquad for \; M_w > M_h \end{cases} \tag{3.8}$$

$$\delta S2S_S{}^{V_{S30}} = g_0 + g_1 \ln(\tfrac{V_{S30}}{800}) + g_2(\ln\left(\tfrac{V_{S30}}{800}\right))^2 \tag{3.9}$$

Equation 3.6 represents geometric spreading. Equation 3.7 represents anelastic attenuation. Equation 3.8 represents magnitude scaling of GMPM. It was noticed that Kotha et al. (2020) GMPM has a problematic magnitude scaling: it is predicting decreasing short-period spectral accelerations with increasing magnitudes for $M_w \geq M_h$=6.2 and has large model uncertainty at near-source distances (i.e., $R_{JB} \leq$30km). In Kotha et al. (2022), these deficiencies are rectified based on analyses of the recently disseminated Near source strong motion (NESS) dataset (Sgobba et al. 2021) by suggesting an updated M_h value of 5.7 instead of 6.2 of Kotha et al. (2020). The adopted functional form is essentially same as that of Kotha et al. (2020). Kotha et al. (2022) also suggests a heteroscedastic variance model as a more appropriate form. Equation 3.11 below represents geometric spreading. Equation 3.12 represents anelastic attenuation. Equation 3.13 represents the magnitude scaling. Equation 3.14 is the V_{S30} based linear site response model.

$$\ln(GM) = e_1 + F_{R,g}\left(R_{JB}, M_w\right) + F_{R,a}\left(R_{JB}\right) + F_M(M_w) + \delta B^0_{e,l} + \delta L2L_l + \delta S2S_S + \varepsilon \tag{3.10}$$

$$F_{R,g}\left(R_{JB}, M_w\right) = \left[c_1 + c_2(M_w - M_{ref})\right] ln\left(\sqrt{\frac{({R_{JB}}^2 + h_D^2)}{({R_{ref}}^2 + h_D^2)}}\right) \tag{3.11}$$

$$F_{R,a}\left(R_{JB}\right) = \left(\tfrac{c_3 + \delta c_{3,r}}{100}\right)\left(\sqrt{{R_{JB}}^2 + h_D^2} - \sqrt{{R_{ref}}^2 + h_D^2}\right) \tag{3.12}$$

$$F_M(M_w) = \begin{cases} b_1(M_w - M_h) + b_2(M_w - M_h)^2 \; for \; M_w \leq M_h \\ b_3(M_w - M_h) \qquad\qquad\qquad for \; M_w > M_h \end{cases} \tag{3.13}$$

$$\delta S2S_S{}^{V_{S30}} = g_0 + g_1 \ln(\tfrac{V_{S30}}{800}) + g_2(\ln\left(\tfrac{V_{S30}}{800}\right))^2 \tag{3.14}$$

$$\tau_{0,M_w}(M_w) = \begin{cases} \tau_{0,M_1} \; for \; M_w < M_1 \\ \tau_{0,M_1} + (M_w - M_1)\left(\frac{\tau_{0,M_2} - \tau_{0,M_1}}{M_2 - M_1}\right) \; for \; M_1 \leq M_w < M_2 \\ \tau_{0,M_2} \; for \; M_w \geq M_2 \end{cases} \quad (3.15)$$

Table 3.1 Variation of anelastic attenuation parameter and seismic source parameter for East Anatolian Fault with period according to Kotha et al. (2022) study.

Period(s)	$\delta c3_r$	$\delta L2L_l$
PGA	-0.00621	-0.13755
PGV	-0.03465	0.06295
0.01	-0.00648	-0.13838
0.025	-0.01332	-0.1605
0.04	-0.04903	-0.20295
0.05	-0.05617	-0.23946
0.07	-0.00093	-0.30816
0.1	-0.0089	-0.26519
0.15	-0.05195	-0.21267
0.2	-0.07252	-0.13864
0.25	-0.04548	-0.12138
0.3	-0.01483	-0.07765
0.35	-0.01802	-0.02888
0.4	-0.02023	0.012709
0.45	0.011713	0.031298
0.5	0.023611	0.073667
0.6	0.055866	0.104542
0.7	0.005166	0.157727
0.75	-0.00045	0.147329
0.8	0.013103	0.144947
0.9	0.016665	0.16071
1	0.010981	0.173444
1.2	0.066352	0.196937
1.4	0.073414	0.202372
1.6	0.03762	0.202576
1.8	-0.00815	0.158931
2	-0.00669	0.169673
2.5	-0.05497	0.162175
3	-0.08009	0.211931
3.5	-0.1802	0.181723
4	-0.15896	0.171109
4.5	-0.0185	0.111226
5	-0.0268	0.119359
6	0.074597	0.060161
7	0.084648	0.037712
8	0.0745	0.035908

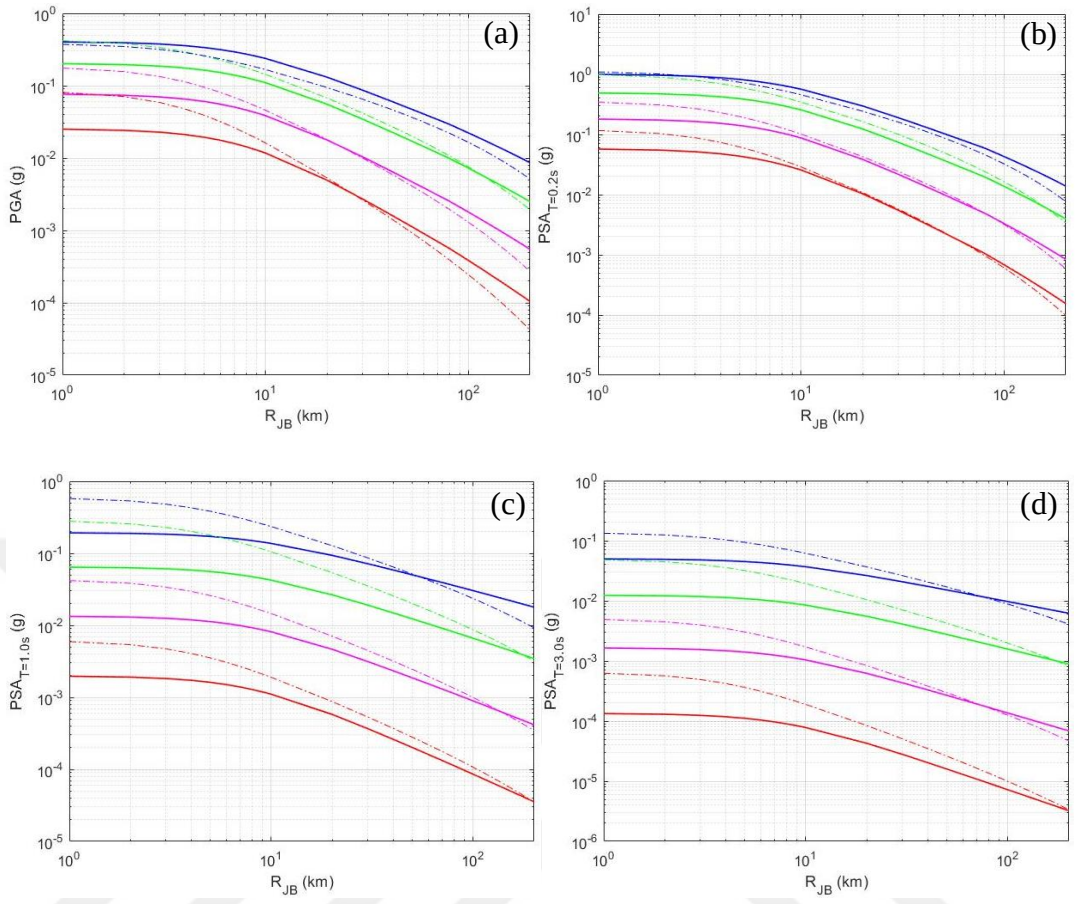

Figure 3.3 Comparison of East Anatolian Fault Specific Kotha et al. (2022) suggested GMPM (represented by dash-dot lines) with Kale et al. (2015) suggested GMPM (represented by solid lines) for Turkey for strike-slip, M_w: 4.0 (represented by red line), 5.0 (represented by pink line), 6.0 (represented by green line) and 7.0 (represented by dark blue line), V_{S30}: 800 m/s scenarios. (a) gives variation of PGA with R_{JB}, (b) gives variation of PSA at T=0.2s with R_{JB}, (c) gives variation of PSA at T=1.0s with R_{JB}, (d) gives variation of PSA at T=3.0s with R_{JB}.

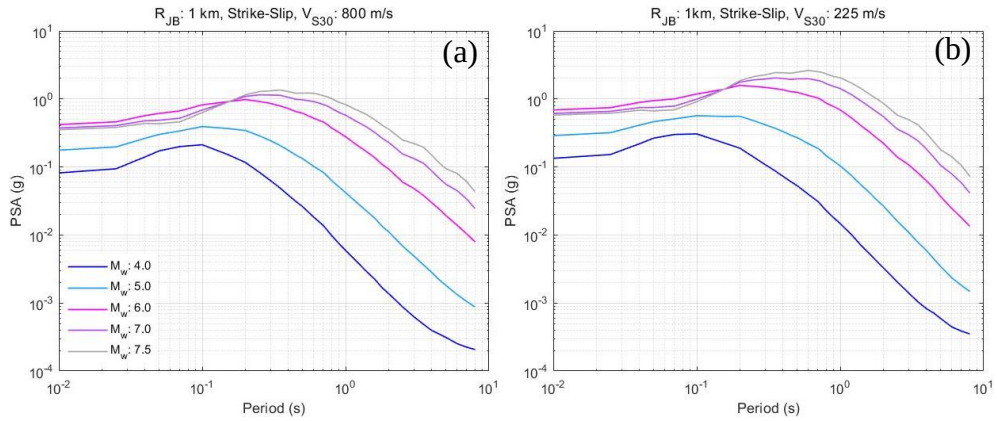

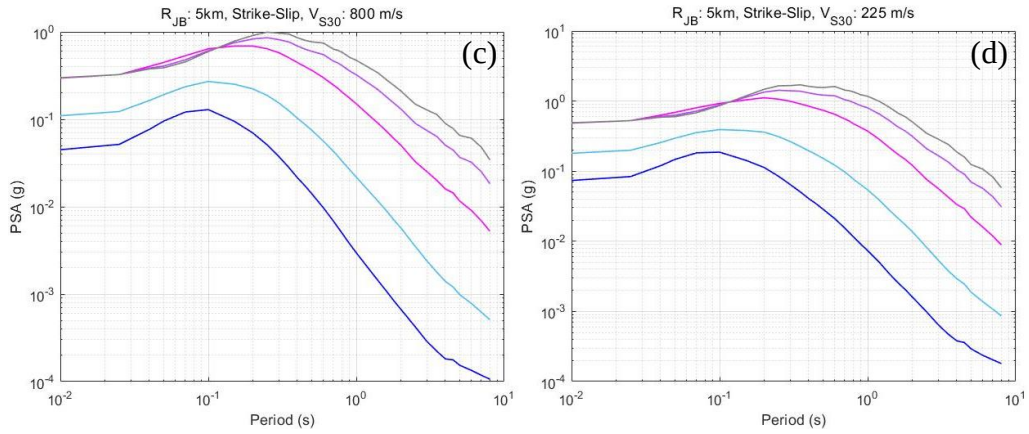

Figure 3.4 Kotha et al. (2022) suggested GMPM for strike-slip, M_w: 4.0, 5.0, 6.0, 7.0 and 7.5, V_{S30}: 800 m/s and 225 m/s, R_{JB}: 1km and 5km scenarios.

Figure 3.3 and 3.4 show that magnitude oversaturation problem of Kotha et al. (2020) is not fully solved by Kotha et al. (2022). Only after R_{JB}>5km that decrease of short period spectral accelerations cannot be seen with increasing magnitude. Distant-dependent decay rates are higher for Kotha et al. (2022) in comparison to Kale et al. (2015). Results shown represent region specific Kotha et al. (2022) model for East Anatolian Fault Zone. According to Figure 3.3, Kotha et al. (2022) predicts higher PSA values than Kale et al. (2015) for near-fault zones for all scenarios considered. As Beyer and Bommer (2006) suggests the conversion factor of 1.0 for all periods considered in this study between RotD50 and geometric mean PGA and PSA no conversion was applied to the Kotha et al. (2022) GMPM results while preparing Figures 3.3 and 3.4. Strong motion database for the Kale et al. (2015) GMPM does not include events with Mw<4.0. This probably has an influence on the predictions of this model for M_w~4.0 events. It should also be emphasized that Kale et al. (2015) GMPM models nonlinear response of soil.

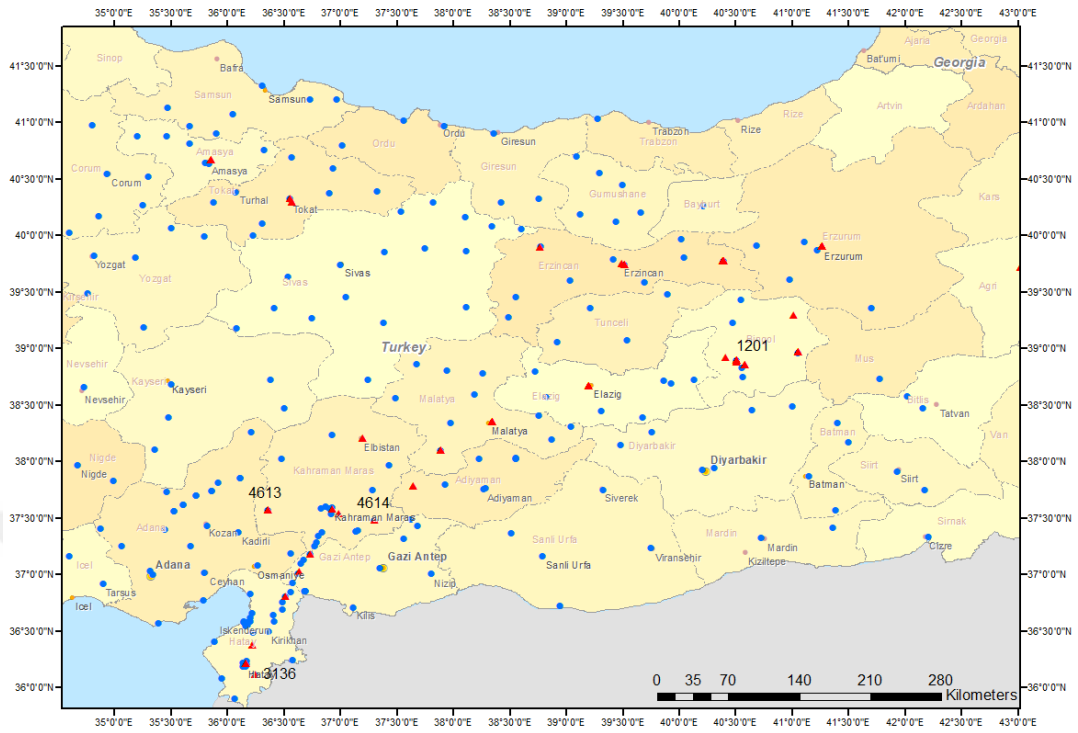

Figure 3.5 Distribution of station sites for which δS2S and or δL2L parameters are computed within the scope of the Kotha et al. (2022) study (red symbol). Distribution of station sites at which 06.02.2023 Kahramanmaraş Earthquake is recorded as well as many aftershocks of this Earthquake (blue symbol). Stations with station codes 1201, 3136, 4613 and 4614 of AFAD are selected for this study.

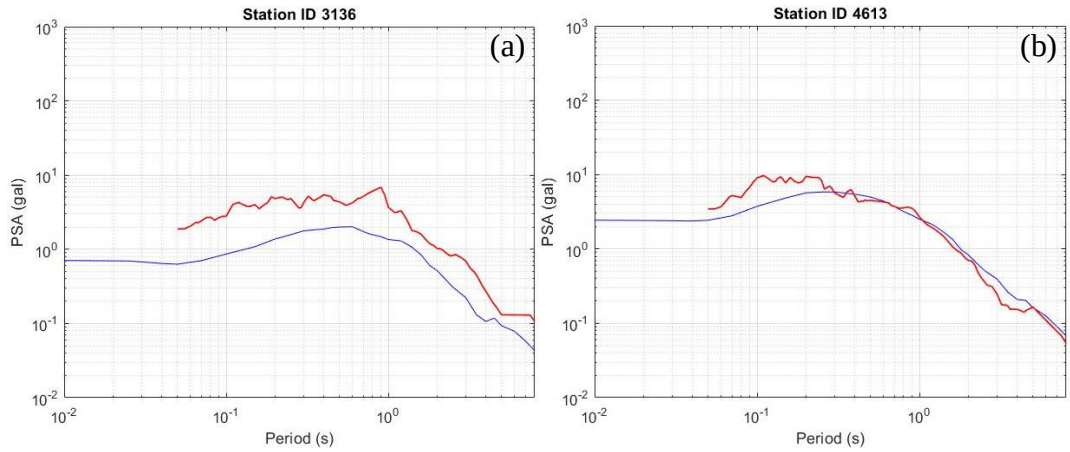

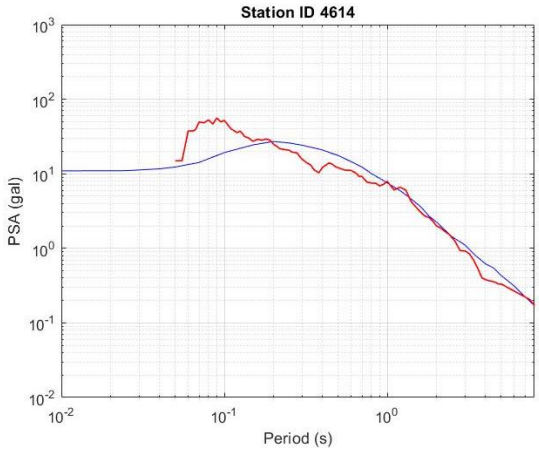

Figure 3.6 Comparison of region-specific median estimates of Kotha et al. (2022) (blue line) for the 07.02.2023 03:13 M_w5.4 aftershock for (a) R_{JB}:226km and V_{S30}:344m/s, (b) R_{JB}:118km and V_{S30}:613m/s, (c) R_{JB}:48km and V_{S30}:672m/s with recorded spectra (red line) at AFAD stations 3136, 4613 and 4614. Region specific computations were done for region: East Anatolian and source: TRTC004.

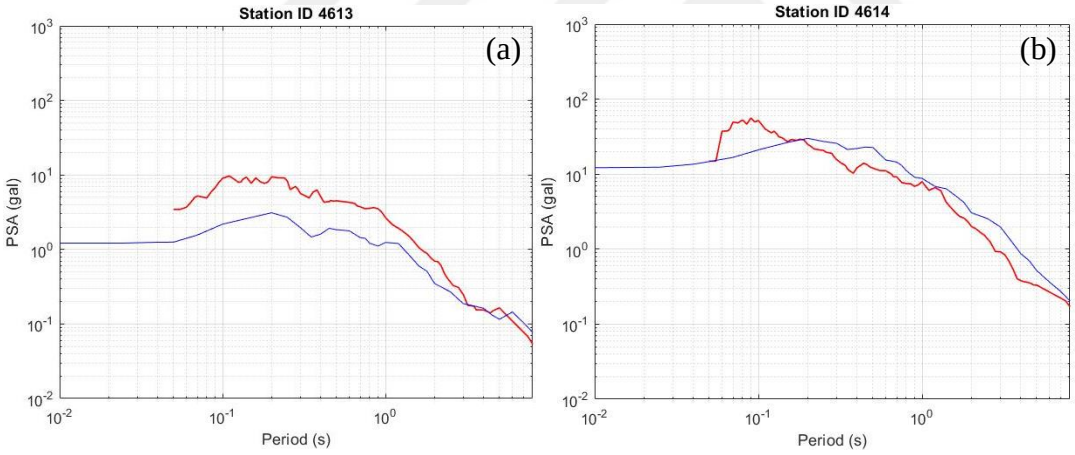

Figure 3.7 Comparison of site-specific median estimates of Kotha et al. (2022) (blue line) for the 07.02.2023 03:13 M_w 5.4 aftershock for (a) AFAD station site 4613 at R_{JB}:118km and (b) AFAD station site 4614 at R_{JB}:48km with recorded spectra (red line) at these stations. Site specific computations were done for sites 4613 with 3 records M_w 4.3-5.4 and R_{epi}:20-40km and 4614 with 1 record M_w 5.3 and R_{epi}:200km, region: East Anatolian and source: TRTC004.

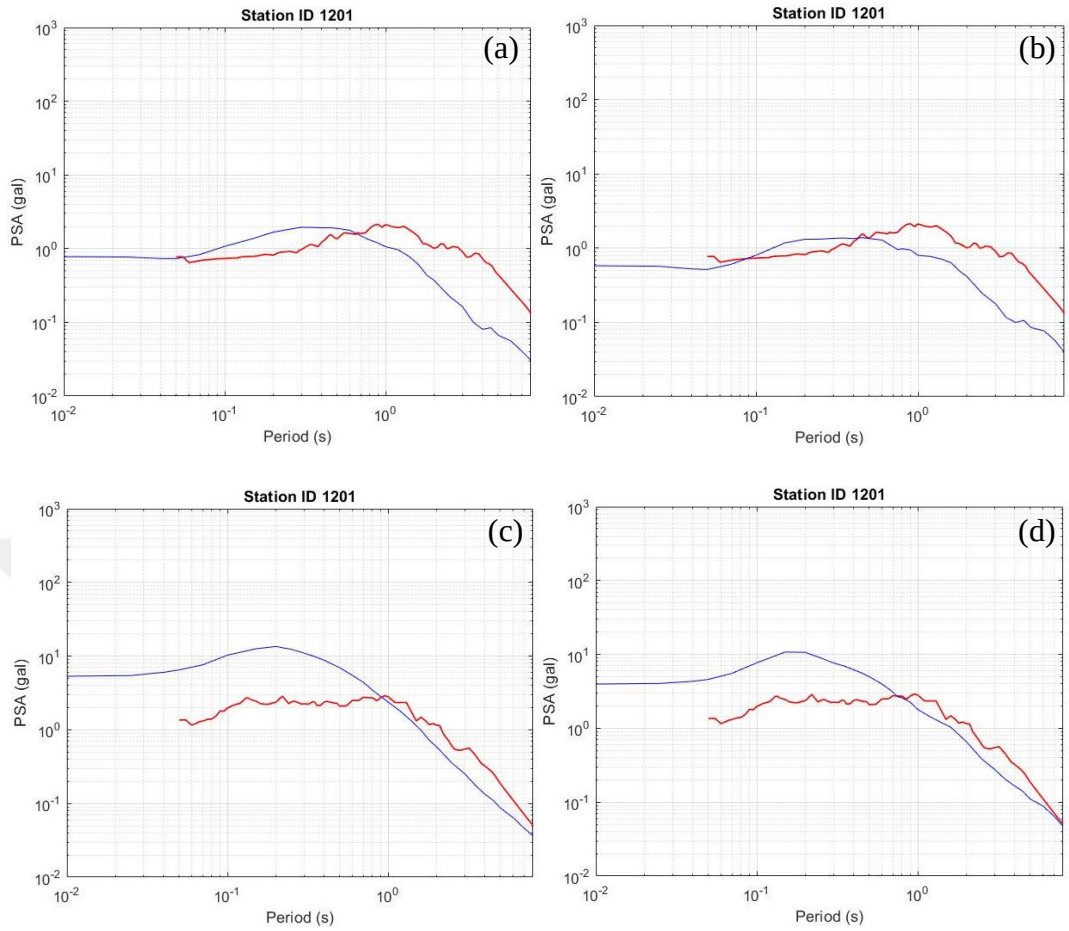

Figure 3.8 Comparison of (a) region-specific median estimate of Kotha et al. (2022) for the 07.02.2023 07:11 M_w5.3 aftershock at AFAD station site 1201 at R_{JB}:185km with recorded response spectrum at this station, (b) site-specific median estimate of Kotha et al. (2022) for the 07.02.2023 07:11 M_w5.3 aftershock at AFAD station site 1201 at R_{JB}:185km with recorded response spectrum at this station, (c) region-specific median estimate of Kotha et al. (2022) for the 17.02.2023 04:36 M_w4.8 aftershock at AFAD station site 1201 at R_{JB}:41km with recorded response spectrum at this station and (d) site-specific median estimate of Kotha et al. (2022) for the 17.02.2023 04:36 M_w4.8 aftershock at AFAD station site 1201 at R_{JB}:41km with recorded response spectrum at this station. Site specific computations were done for site 1201 with 18 records M_w 4.0-6.5 and R_{epi}:10-140km, region: East Anatolian and source: TRTC004. Blue lines represent Kotha et al. (2022) model and red lines represent recorded response spectra. For the station site 1201, both AFAD and Kotha et al. (2022) databases give the V_{S30} value of 529 m/s.

This specific aftershock was chosen deliberately so that it is well contained by the magnitude range of Kotha et al. (2022) GMPM. The mainshock of 06.02.2023 event was on purposes not included in the analysis as it is not within the magnitude range of GMPM under consideration. For the 2 stations selected, region specific estimations match the recorded spectra well. For station site 3136 computed spectral acceleration values remain below the recorded acceleration for all periods considered. This station is at R_{JB} value of 226km, a rather distant station. For this station GMPM suggested decay is more than what is observed in the case of this specific event at the site of interest. Also, V_{S30} value of this station site is rather low. Kotha et al. (2022) model does not consider nonlinear soil response. Including δS2S estimates within the scope of the site-specific computations did not improve the results for both of the station sites considered. The reason behind this is probably the fact that number of records utilized for estimation of this parameter is rather limited. For station site 3136, δS2S estimate was not provided. For the station site 4614, AFAD provides V_{S30} value as 541 m/s but in the Kotha et al. (2022) study database the V_{S30} value for this station is listed as 672 m/s.

A similar comparison was also conducted for the station site 1201. For this station, δS2S parameter was computed based on 10 records hence is a more accurate estimate. Figure 3.8 illustrates computed and recorded response spectra for station 1201. Two separate aftershocks of the Kahramanmaraş Earthquake were used for this comparison. 07.02.2023 07:11 and 17.02.2023 04:36 M_w 5.3 and 4.8 earthquakes. Although site-specific estimates are closer to the recorded spectra than region-specific estimates, there are marked differences between the two spectral shapes. In Kotha et al. (2022) study, Bingöl is taken to be part of the source TRTC004. This is the probable cause of the observed difference. Modelling this region as a separate source (i.e., as in the case of the Turkish Seismic Hazard Map 2014 study) would improve the computed results.

3.2 Estimating Additional Source and Site Parameters for The Kale et al. (2015) GMPM

Cagnan and Akkar (2019) computed the δS2S and δL2L values for the Kale et al.(2015) GMPM based on the Turkish strong-motion database developed within the scope of the EMME (Earthquake Model of the Middle East) project (Akkar et al., 2014). The δL2L value computed is applicable for the North Anatolian Fault Zone and the δS2S values were computed for station sites that recorded 5 or more events of the Akkar et al. (2014) database. In order to calculate the δL2L value for the Elazığ region, which is located near the East Anatolian Fault Zone, relevant data of the European Strong Motion Database (Luzi et al. (2018)) was used together with the Turkish Strong Motion Database (Akkar et al. (2014)). Residuals in a statistical framework are the differences between observed and predicted values of data. These can also be referred to as errors. In the context of this study, residuals were obtained by taking the logarithmic difference of observed and computed data (Eq. 3.16), and also these residuals are referred to as total residuals.

$$Total\ residual = \log(observed) - \log(computed) \tag{3.16}$$

Total residuals (Δ_{es}) consist of the sum of both the between-event (δB_e) and within-event (δW_{es}) components (Eq. 3.17) (Eq. 1 in Cagnan & Akkar, 2019).

$$\Delta_{es} = \delta W_{es} + \delta B_e \tag{3.17}$$

The distributions of between-event residuals obtained from the TSMD2014 and ESMD2018 databases with magnitude are shown in Figure 3.9 for PGA, SA0.2 and SA1.0 GMIMs. To merge the data obtained from these two databases, it was ensured that they originated from the same statistical distribution. For this purpose, Two-Sample Kolmogorov-Smirnov test (N.V. Smirnov,1939) was conducted on the available data using the MATLAB software program (1994-2023 The Mathworks, Inc. R2022b). As a result, it was observed that the data came from the same normal distribution, and these two datasets were combined. This enhanced the available data quantitatively for the East Anatolian Fault Zone δL2L calculation as well as δS2S calculation for the selected station sites.

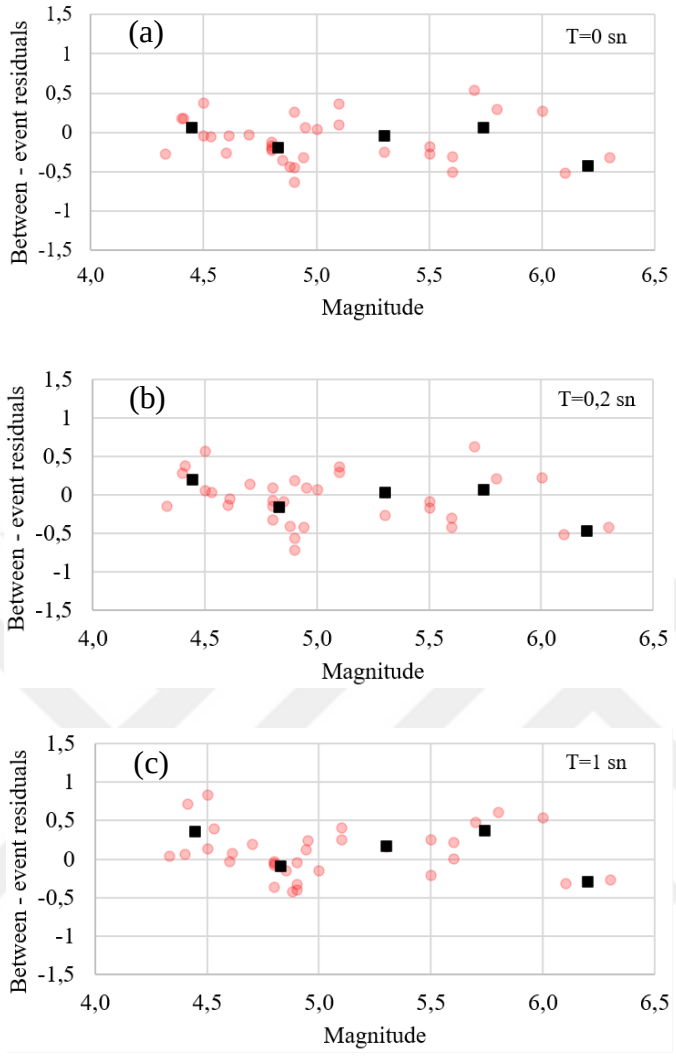

Figure 3.9 Magnitude dependent distribution of between-event residuals after merging the TSMD2014 and EMSD2018 databases for (a) peak ground acceleration (PGA), (b) spectral acceleration at 0.2s period (SA0.2) and (c) spectral acceleration at 1.0s period (SA1.0). Black square dots represent mean value of between-event residuals for corresponding magnitude bins.

Table 3.2 Ground motion records utilized in the δL2L calculation

	Earthquake ID	M	Station ID	R_{JB} (KM)
TSMD2014	140	6	53	22
	143	5,8	53	30,2
	621	4,5	2503	38,1
	648	5,1	231	49,5
	1634	4,6	2495	65,1

Table 3.2 (Cont'd)

TSMD2014	1666	4,8	2503	49,1
	2746	4,8	2488	43,2
	2826	6,3	229	3,4
	2898	4,9	229	11,9
	2909	4,8	229	19
	2997	5,5	231	38,5
	3171	4,7	2503	60,3
	3179	4,9	2488	36,7
	3282	5,6	231	30
	3532	5,1	231	57,1
	3576	5	2206	118,2
	3695	5,5	229	134,3
	3703	4,8	2503	79,6
	3738	4,4	2343	123,6
	4747	6,1	2436	188
	4748	5,6	229	39,5
ESMD2018	TK-2003-0109	4,9	TK-1201	5,6
	TK-2004-0013	4,6	TK-1201	325,4
	TK-2007-0008	4,9	TK-1201	233,2
	TK-2007-0024	5,3	TK-1201	239,1
	EMSC-20101114_0000105	4,9	GE-CSS	52,8
	EMSC-20120919_0000033	5,0	KO-KRTD	61,8
	EMSC-20121113_0000120	4,9	KO-KRTD	62,1
	EMSC-20121114_0000001	4,4	KO-KRTD	61,8
	EMSC-20140609_0000007	4,5	KO-KHMN	232,5
	EMSC-20150108_0000051	4,5	KO-CMRD	111
	EMSC-20150210_0000009	4,3	KO-CMRD	155,7
	TK-1997-0003	5,7	TK-3102	261,1

Subsequently, the between-event residuals obtained based on by using Equation 3.20 below were used to calculate δL2L values for each individual period utilizing Equation 3.18 as described in the paper by Cagnan and Akkar (2019) (Equation 6 in the article). Simultaneously, the τ_{ss} value was determined by applying Equation 3.19 from the aforementioned Cagnan and Akkar (2019) paper (Equation 7 in article). The resulting δL2L and τ_{ss} values have been presented in Table 3.3.

$$\delta L2L = \frac{1}{NE}\sum_{e=1}^{NE} \delta B_e \quad (3.18)$$

$$\tau_{ss} = \sqrt{\frac{\sum_{e=1}^{NE}(\delta B_e - \delta L2L)^2}{(NE-1)}} \quad (3.19)$$

In Equation 3.18 and 3.19, NE signifies the number of earthquakes linked to the source region under consideration, δB_e denotes the between-events residuals, δL2L represents the average between-events residuals, and τ_{ss} denotes the source-corrected between-event standart deviation.

Table 3.3 Source term and source-corrected between-event standard deviation for East Anatolian Fault with period.

Period(s)	δL2L	τ_{ss}
0	-0,09579	0,292524
0,01	-0,09868	0,292346
0,04	-0,11237	0,298517
0,05	-0,1211	0,301358
0,1	-0,09298	0,355988
0,15	-0,05339	0,361273
0,2	-0,04217	0,327237
0,3	0,004204	0,310024
0,4	0,039969	0,332597
0,5	0,050263	0,352034
0,6	0,059357	0,327045
0,7	0,101855	0,328106
0,75	0,099545	0,325632
0,8	0,107426	0,330601
0,9	0,092218	0,33836
1	0,090149	0,32282
1,2	0,054663	0,303908
1,4	0,062329	0,302332
1,6	0,051542	0,294328
1,8	0,051448	0,260814
2	0,049111	0,241827
3	0,043045	0,329209
4	0,097242	0,333356

In the subsequent stage, the δS2S data was computed by examining the stations in close proximity to the Elazığ province and the earthquakes with a magnitude of 4.5 or greater, which were recorded by a minimum of 5 stations. After conducting these

investigations, four stations within the region, specifically stations 2301, 2302, 2304, and 2307, were chosen (Figure 3.10). These are earthquake recording stations of AFAD (Republic of Turkey, Ministry of Interior, Disaster and Emergency Management Presidency). The raw data for earthquakes with a magnitude of 4.5 or higher, recorded by these stations, were obtained from the AFAD website (https://tadas.afad.gov.tr). During the process of retrieving the data, it was subjected to filtering using the Butterworth filter settings (R. Paolucci et al. 2011, Record Processing in ITACA, the New Italian Strong-Motion Database). A fourth-order filtering was applied to all selected earthquakes. For the east-west/north-south directions, a low-pass cutoff frequency of 0.06 Hz and a high-pass cutoff frequency of 25 Hz were chosen, while for the up-down direction, a low-pass cutoff frequency of 0.06 Hz and a high-pass cutoff frequency of 20 Hz were selected. The triggering type was chosen as normal. The earthquakes for which data were acquired are presented in Table 3.3.

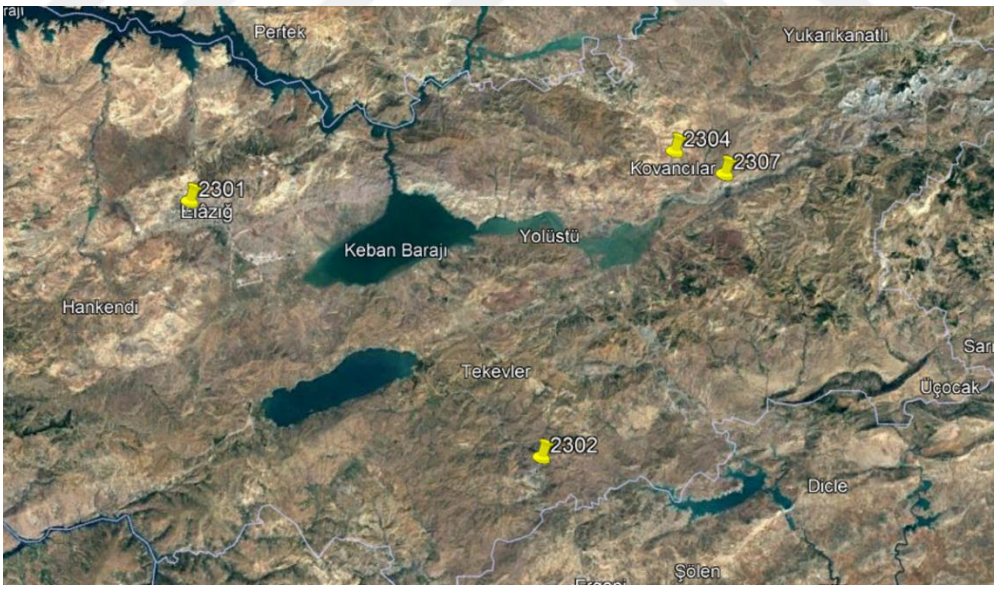

Figure 3.10 Selected strong-motion stations

Table 3.4 Selected earthquakes, recorded by 2302, 2304, 2307 stations, from AFAD website. (Note: Since δS2S data for station 2301 is taken from the study of Cagnan&Akkar

(2019), a separate calculation for δS2S data for this station has not been performed. Therefore, earthquake records were not selected for station 2301.)

Station 2302			Station 2304			Station 2307		
EQ ID	**M**	**R_{JB}/R_{EPI} (Km)**	**EQ ID**	**M**	**R_{JB}/R_{EPI} (Km)**	**EQ ID**	**M**	**R_{JB}/R_{EPI} (Km)**
462966	4,5	R_{JB}=43,99	462966	4,5	R_{JB}=69,86	462966	4,5	R_{JB}=73,85
462093	4,5	R_{JB} =30,73	457806	4,5	R_{EPI}=70,36	462093	4,5	R_{JB} =55,72
458247	4,5	R_{EPI}=81,49	441177	4,5	R_{EPI}=61,26	457806	4,5	R_{EPI}=74,50
457806	4,5	R_{EPI}=45,70	339526	4,5	R_{EPI}=77,89	457759	4,5	R_{EPI}=70,90
457759	4,5	R_{EPI}=41,44	319551	4,5	R_{EPI}=69,31	441177	4,5	R_{EPI}=64,15
441177	4,5	R_{EPI}=99,44	469577	5	R_{JB} =74,38	356410	4,5	R_{EPI}=99,98
457780	4,6	R_{EPI}=85.45	458439	5,1	R_{EPI}=74,43	339526	4,5	R_{EPI}=73,78
457765	4,6	R_{EPI}=56,17	505564	5,2	R_{EPI}=61,46	319551	4,5	R_{EPI}=69,63
515810	4,7	R_{EPI}=78,83	436571	5,2	R_{EPI}=74,51	457765	4,6	R_{EPI}=86,30
489285	4,7	R_{JB} =93,90	319064	5,3	R_{EPI}=67,40	455571	4,9	R_{EPI}=86,64
467386	4,9	R_{EPI}=79,29	133752	5,3	R_{EPI}=27,25	469577	5	R_{JB} =78,42
455571	4,9	R_{EPI}=57,49	457758	6,8	R_{JB} =74,40	458439	5,1	R_{EPI}=78,32
469577	5	R_{JB} =48,24				505564	5,2	R_{EPI}=61,07
458439	5,1	R_{EPI}=47,50				436571	5,2	R_{EPI}=78,51
523936	5,2	R_{JB} =94,31				491958	5,3	R_{JB} =70,10
436571	5,2	R_{EPI}=48,37				319064	5,3	R_{EPI}=67,50
491958	5,3	R_{JB} =47,36				133752	5,3	R_{EPI}=30,43
133752	5,3	R_{EPI}=18,63				457758	6,8	R_{JB} =78,39
457758	6,8	R_{JB} =47,56						

The data for these earthquakes, including moment magnitude, Joyner and Boore distance (R_{JB})/Epicentral distance (R_{EPI}), soil conditions (V_{S30}), and fault mechanism were utilized as input for the GMPM by Kale et al. (2015) and based on this GMPM relevant GMIM values were computed using the MATLAB software program. As a result of this analysis, both the existing observed data and calculated data related to the selected earthquakes were obtained, thus total residuals were obtained. Additionally, as a result of the analysis, τ (between-event sigma) and ϕ (within-event sigma) values were also obtained.

Total residuals were incorporated into Equation 3.20 to calculate the between-event residuals (Eq. 11 in Kotha et al., 2017).

$$\delta B_e = \frac{\tau^2 \sum_{s=1}^{n_e} (\log(GM_{e,s}) - \log(\mu_{e,s}))}{n_e \tau^2 + \phi^2} \quad (3.20)$$

In Equation 3.20, the variable "n_e" represents the total count of accessible recordings for event "e". The variable "$GM_{e,s}$" denotes the observed ground motion for event "e" that has been recorded at station "s". Log($\mu_{e,s}$) represents the corresponding predicted median value; the variables " τ " and " ϕ " represent the between-event and within-event standard deviations, respectively, as derived from the Kale et al. (2015) GMPM.

Subsequently, the obtained between-event residuals were input into Equation 3.17 to calculate within-event residuals. The calculated within-event residuals, when placed into Equation 3.21, were used to individually calculate δS2S values for each station (eq. 12 in Kotha et al., 2017).

$$\delta S2S = \frac{\phi_{S2S}^2 \sum_{e=1}^{n_s} \delta W_{es}}{n_s \phi_{S2S}^2 + \phi_0^2 + \tau^2} \quad (3.21)$$

In Equation 3.21, ϕ_{S2S} represents site-to-site variability, and these values are period-dependent. Since we had ϕ_{S2S} values for specific periods as a result of the Cagnan and Akkar (2019) study, linear interpolation was employed to determine the ϕ_{S2S} value for intermediate periods. n_s, represents the number of records utilized, while τ represents the between-event standard deviation of the Kale et al. (2015) GMPM. ϕ_0, represents the event-corrected single-station standard deviation coefficient, which is dependent on magnitude and was determined based on the criteria in Equation 3.22.

$$\phi_{SS} = \phi_0 = \begin{Bmatrix} \phi_{ss1} & for\ M < M_{c1} \\ \phi_{ss1} + (\phi_{ss2} - \phi_{ss1})(\frac{M - M_{c1}}{M_{c2} - M_{c1}}) & for\ M_{c1} \le M \le M_{c2} \\ \phi_{ss2} & M > M_{c2} \end{Bmatrix} \quad (3.22)$$

In Equation 3.22, M_{c1}=6 and M_{c2}=6.5. Depending on the magnitude of each earthquake, ϕ_{SS} was calculated using the ϕ_{ss1} and ϕ_{ss2} values from table 3 in Cagnan & Akkar (2019). Linear interpolation was applied for intermediate periods. Since the magnitudes of the earthquakes used in the analysis did not exceed 6, except for one

earthquake, according to Equation 3.22, $\phi_0=\phi_{ss1}$. For earthquake ID 457758 with a magnitude of 6.8, $\phi_0=\phi_{ss1}$ was also assumed. Thus, the ϕ_0 in Equation 3.21 was calculated. The obtained ϕ_{S2S}, τ, and ϕ_0 values are inserted into Equation 3.21 to calculate the δS2S value according to Kotha et al. (2017)'s work. As a result, the calculated δS2S and ϕ_{SS} values are provided in Table 3.4.

Table 3.5 δS2S and ϕ_{SS} values computed for Kale et al. (2015) GMPM within the scope of this study.

	KALE 2015			
PERIOD	**δS2S 2302**	**δS2S 2304**	**δS2S 2307**	**ϕss**
0	-0,412076	-0,416708	-0,527194	0,4612
0,05	-0,612034	-0,493452	-0,541611	0,4918
0,055	-0,656634	-0,510608	-0,552856	0,49184
0,06	-0,561059	-0,426585	-0,633959	0,49188
0,065	-0,559024	-0,405709	-0,640867	0,49192
0,067	-0,53873	-0,386567	-0,643673	0,491936
0,07	-0,527861	-0,380534	-0,628967	0,49196
0,075	-0,505133	-0,363806	-0,645318	0,492
0,1	-0,383187	-0,385078	-0,630785	0,4823
0,15	-0,267624	-0,330713	-0,704308	0,4635
0,2	-0,278722	-0,353608	-0,638768	0,4785
0,3	-0,10242	-0,429779	-0,594235	0,5006
0,4	0,0159803	-0,519044	-0,442591	0,5249
0,5	0,0841633	-0,497249	-0,33579	0,5133
0,75	0,1038946	-0,38216	-0,224671	0,5165
1	0,1445043	-0,352233	-0,182359	0,5142
1,5	0,1011129	-0,150607	-0,132613	0,5148
2	0,1877325	-0,230391	-0,151264	0,5559
3	0,0944675	-0,182432	0,0022763	0,5571
4	0,1057616	-0,029381	-0,041274	0,4754

In the next section, non-ergodic probabilistic seismic hazard assessment will be explicated using the Ground Motion Prediction Models (GMPM) described in this section and the OpenQuake platform (Pagani et al., 2023).

CHAPTER 4

NONERGODIC PROBABILISTIC SEISMIC HAZARD ASSESSMENT

In this study, seismic sources used within the scope of the European Seismic Hazard Model 2020 (ESHM2020) are adopted to model seismic hazard for the 4 selected station sites. Details of the model developed within the scope of the ESHM2020 project are given in Danciu et al. (2021). In ESHM2020, both area seismic sources and fault sources are used. Seismicity that cannot be associated with a fault source is modelled by using smoothed seismicity. The selected station sites are under the influence of the East Anatolian Fault Zone mainly. The ESHM2020 models the East Anatolian Fault Zone with the area source TRAS481 (Figure 1) and the fault source TRCF002-T (Figure 2). Variation of the a- and b-values describing change of seismic activity rate of regional seismic area sources are given in Figures 3 and 4. These are computed based on an earthquake catalogue that covers the period 1000-2014. In ESHM2020, uncertainty associated with the computed a- and b-values is reflected by adopting a logic tree scheme with 3 branches representing each parameter: average value branch, upper bound value branch and lower bound value branch. To each branch, a corresponding weight is assigned. This logic tree scheme is adopted in the current study as well. Maximum moment magnitude value assigned to seismic sources play an important role on the seismic hazard results as well. Variation of this value for the regional area seismic sources is given in Figure 5 and for the regional fault sources in Figure 7. ESHM2020 suggests that for the region of interest M_w=8.0 is an upper bound. Slip rate of fault sources is an important parameter defining seismic activity of these sources. Figure 6 gives variation of the slip rate for the regional fault sources. In ESHM2020, the on average slip rate value of 7 mm/year is adopted for the East Anatolian Fault Zone. As in the case of a-value, b-value and maximum M_w parameters, for the slip rate of fault sources a logic tree scheme is adopted and uncertainty associated with this parameter is reflected to the hazard

results. Slip rate is modelled for the East Anatolian Fault Zone as a range of 5.4-8.9 mm/year in ESHM2020.

In ESHM2020 model, the weights assigned to possible fault mechanisms for the area sources associated with the East Anatolian Fault Zone are as the following: for TRAS481 34% strike-slip, 33% normal, 33% reverse and for LBAS341 85% strike-slip, 15% normal. On the other hand, the Turkish Seismic Hazard Map 2014 (Akkar et al., 2014) study represents the East Anatolian Fault Zone with 2 area sources to which assigned fault mechanism weights are as the following: 85% strike-slip and 15% reverse. The Turkish Seismic Hazard Map 2014 study assigned slip rates to the fault sources representing the East Anatolian Fault Zone changing in the range 5-15 mm/year. Despite the outlined differences, in the current study ESHM2020 seismic source model is adopted with its original parameters and seismic hazard assessment runs were completed based on this source model.

In the current study, all the seismic hazard assessment runs were performed in the OpenQuake platform (Pagani et al., 2023). For a total of 5 cases, seismic hazard assessment runs were completed at the 4 selected station sites: case 1 original Kale et al. (2015) attenuation relationship with site characteristics represented with the V_{s30} values given by AFAD to represent ergodic case, case 2 original Kotha et al. (2016) attenuation relationship with site characteristics represented with the V_{s30} values given by AFAD and adjustment factors suggested for Turkey to represent ergodic case, case 3 nonergodic Kale et al. (2015) attenuation relationship with East Anatolian Fault δL2L parameter and δS2S site parameters computed for the 4 selected station sites to represent partially nonergodic case without path effects considered, case 4 nonergodic Kotha et al. (2020) attenuation relationship with relevant source (δL2L) and path (δc3r) parameters but site characteristics represented with the V_{s30} values given by AFAD to represent partially nonergodic case without site specific effects considered, case 5 nonergodic Kotha et al. (2020) attenuation relationship with relevant source (δL2L), anelastic attenuation/path (δc3r) and site (δS2S) parameters to represent fully nonergodic case.

For station 2301, Kotha et al. (2017) approach is followed to obtain δL2L and δS2S parameters that made carrying out nonergodic seismic hazard assessment possible for this station site. In Kotha et al. (2020) study, nonlinear mixed effects approach first suggested by Stafford (2014) was applied to compute δL2L, δc3r and δS2S parameters for station 2301. The two approaches yield reasonably close results hence Kotha et al. (2017) approach can be employed to obtain first approximations of parameters like δL2L, δc3r and δS2S as applying the nonlinear mixed effects approach and developing a specific nonergodic GMPM for every site of interest is not feasible. For station site 2301, waiving the ergodic assumption influences the spectral acceleration results around 0.1s and 1.0s the most, yielding higher responses.

Waiving the ergodic assumption not always reduce the seismic hazard results. Depending on the characteristics may not influence the results considerably, decrease or increase the hazard results. For the station site 2302, nonergodic 475 years return period uniform hazard spectra exceeds its ergodic counterpart around 0.5s but is below its ergodic counterpart around 0.001s. But for the station sites 2304 and 2307, nonergodic 475 years return period uniform hazard spectra is below its ergodic counterpart around both 0.001s and 0.5s. Hence the influence of the ergodic assumption on the uniform hazard spectra is site dependent and influenced by the return period of interest as well.

Influence of δL2L and δc3r parameters (i.e., partial nonergodic approach) on seismic hazard results also studied for the station sites 2302,2304 and 2307 as computed by Kotha et al. (2020) following the nonlinear mixed effects approach. In the period range of 0.001s-2s, these partially nonergodic uniform hazard spectra exceed their ergodic counterparts. For this comparison site influences are taken into account through site functions of Kotha et al. (2020) and Kotha et al. (2016) studies and are dependent on the specific V_{S30} values of the station sites. With reducing V_{S30} values and increasing nonlinearity Kotha et al. (2020) and Kotha et al. (2016) site functions differ from one another more.

All of these observations can be seen in Figures 10-25 below.

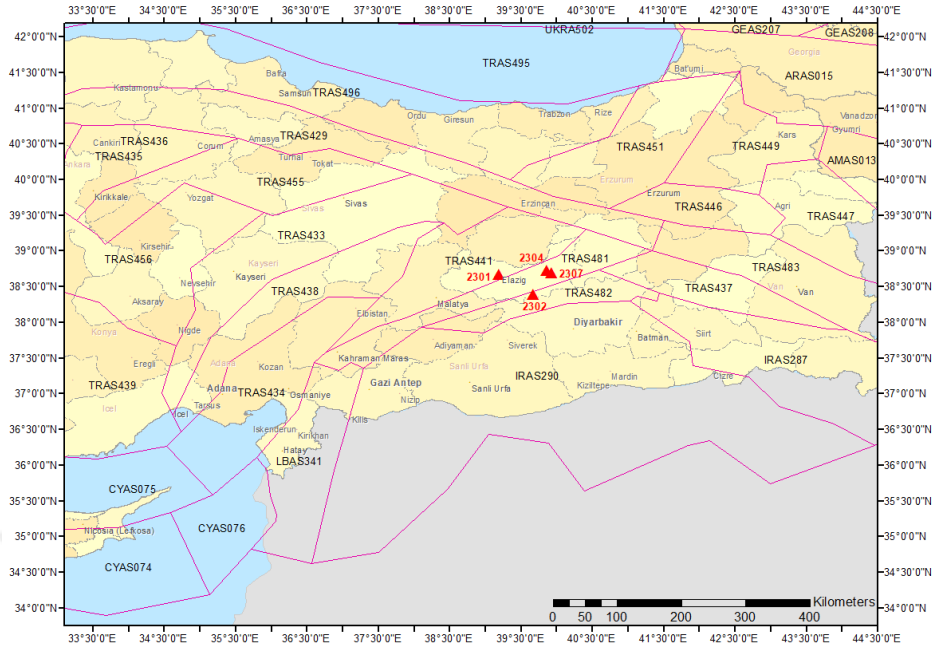

Figure 4.1 Area seismic sources of European Seismic Hazard Model 2020 in relation to the selected station sites of AFAD (i.e., 2301, 2302, 2304, 2307). TRAS481 and LBAS341 are the area seismic sources representing the East Anatolian Fault Zone.

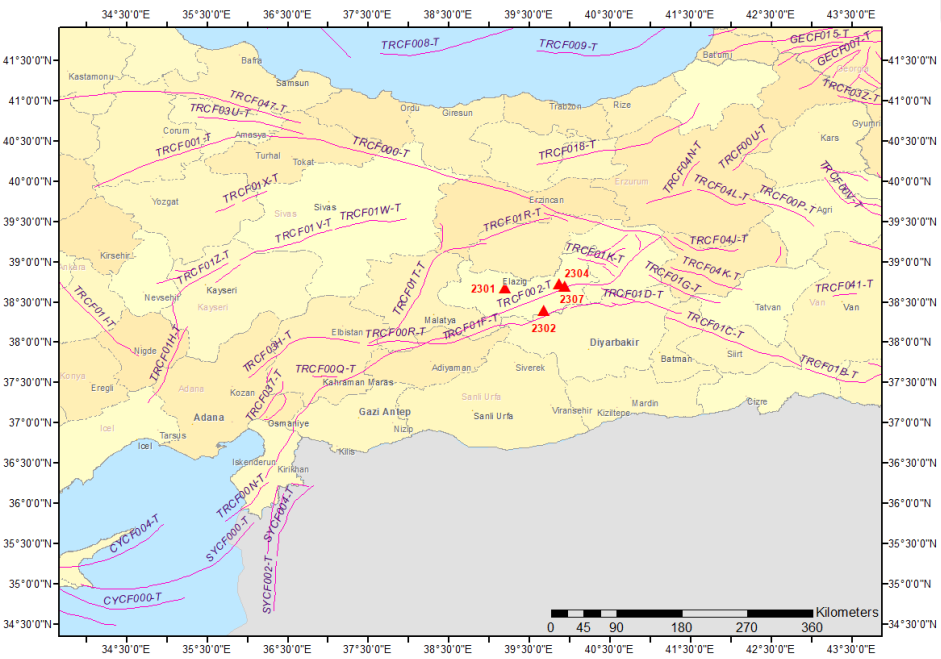

Figure 4.2 Fault sources of European Seismic Hazard Model 2020 in relation to the selected station sites of AFAD (i.e., 2301, 2302, 2304, 2307). TRCF002-T is the fault source representing the East Anatolian Fault Zone.

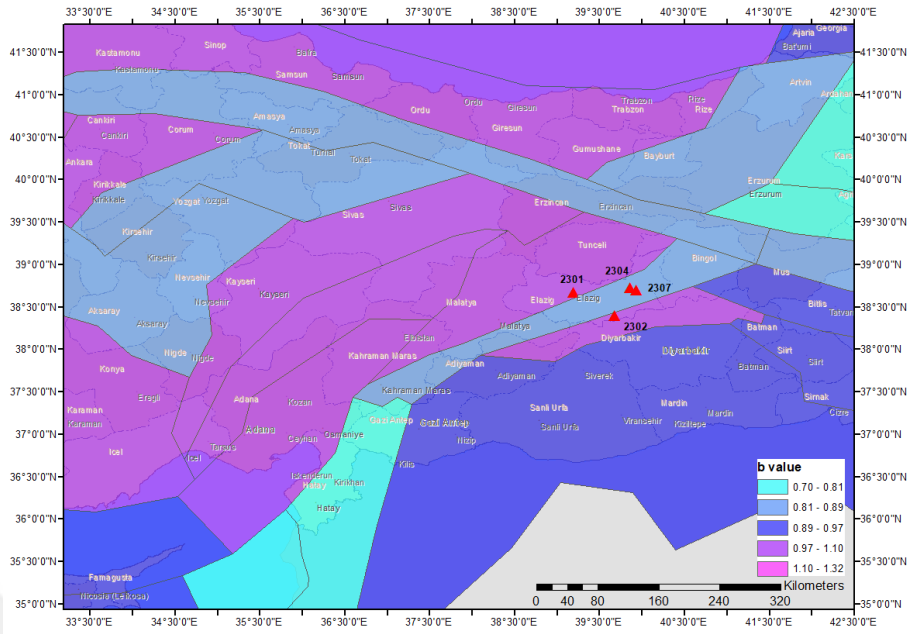

Figure 4.3 Guttenberg-Richter Earthquake Recurrence Model b-value assigned to the area seismic sources of European Seismic Hazard Model 2020 in relation to the selected station sites of AFAD (i.e., 2301, 2302, 2304, 2307). ESHM2020 models uncertainty associated with b-values by using 3 b-values and corresponding weights assigned to them: upper, mid and lower. Given b-values of this figure are the middle b-values.

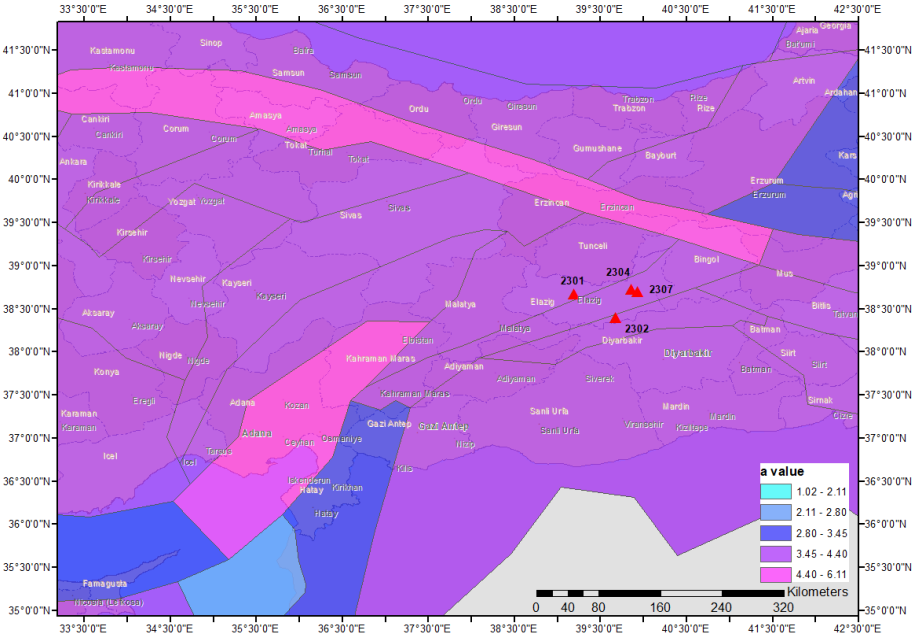

Figure 4.4 Guttenberg-Richter Earthquake Recurrence Model a-value assigned to the area seismic sources of European Seismic Hazard Model 2020 in relation to the selected station

sites of AFAD (i.e., 2301, 2302, 2304, 2307). ESHM2020 models uncertainty associated with a-values by using 3 a-values and corresponding weights assigned to them: upper, mid and lower. Given a-values of this figure are the middle a-values.

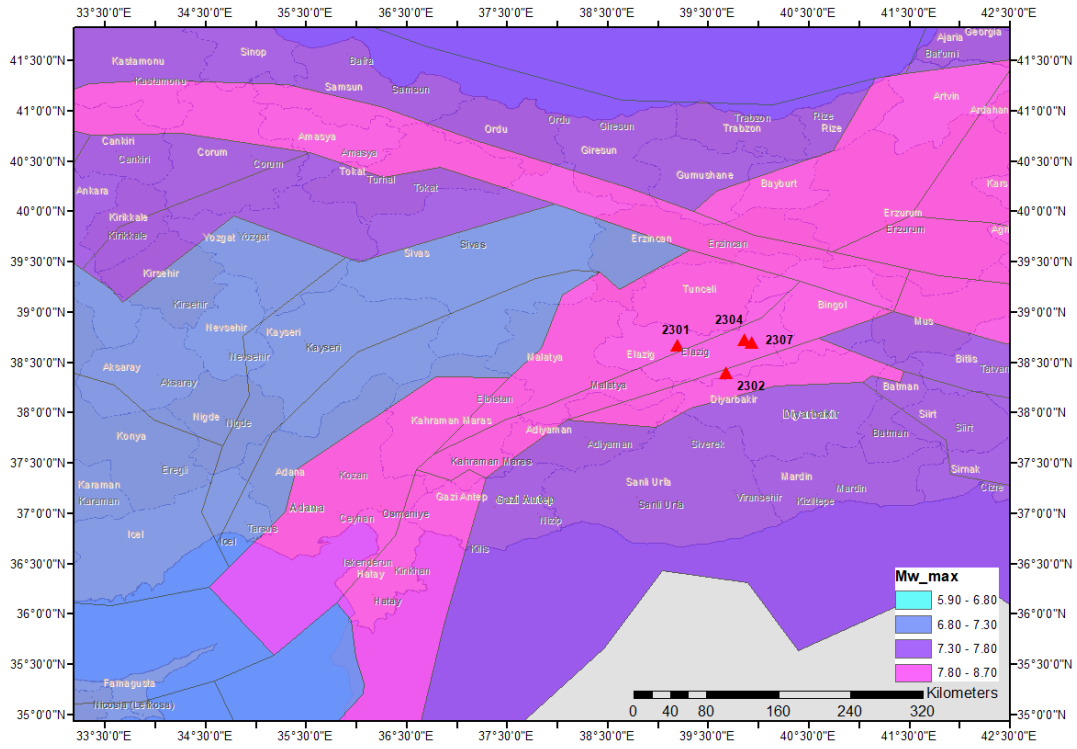

Figure 4.5 Maximum M_w value assigned to the area seismic sources of European Seismic Hazard Model 2020 in relation to the selected station sites of AFAD (i.e., 2301, 2302, 2304, 2307). ESHM2020 models uncertainty associated with maximum M_w values by using 3 M_w values and corresponding weights assigned to them: upper, mid and lower. Given M_w -values of this figure are the middle M_w values.

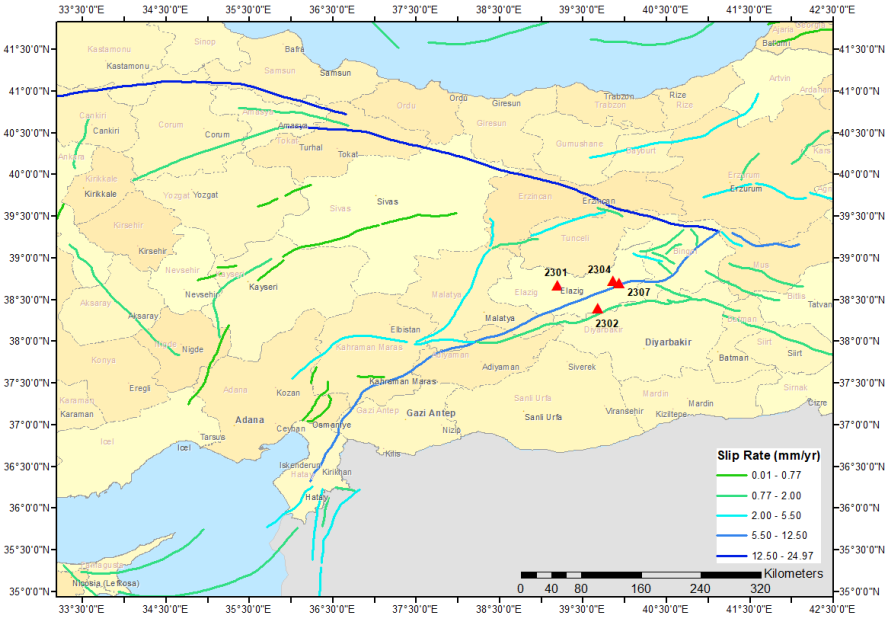

Figure 4.6 Slip rates assigned to the fault sources of European Seismic Hazard Model 2020 in relation to the selected station sites of AFAD (i.e., 2301, 2302, 2304, 2307). ESHM2020 models uncertainty associated with slip rate values by using 3 slip rate values and corresponding weights assigned to them: upper, mid and lower. Given slip rate values of this figure are the middle slip rate values.

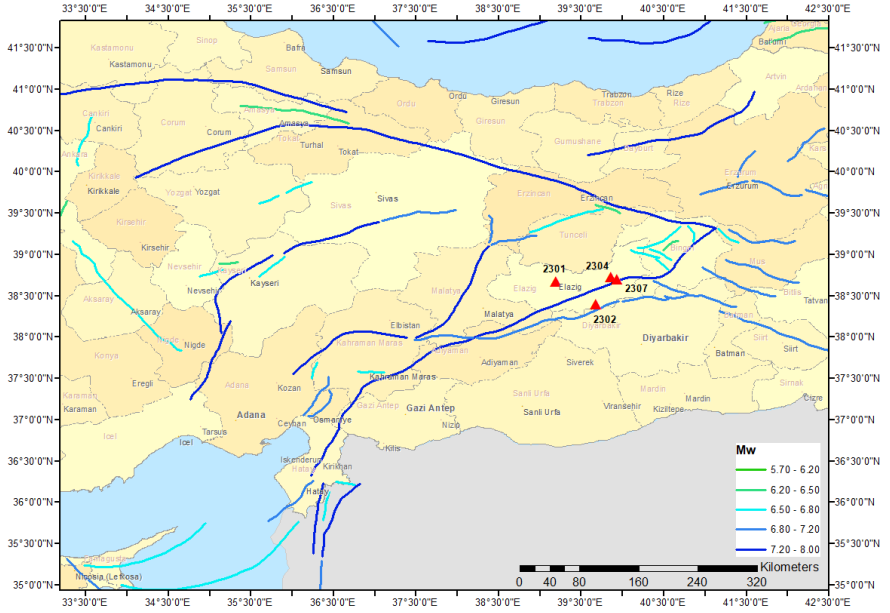

Figure 4.7 Maximum M_w value assigned to the fault sources of European Seismic Hazard Model 2020 in relation to the selected station sites of AFAD (i.e., 2301, 2302, 2304, 2307).

ESHM2020 models uncertainty associated with maximum M_w values by using 3 M_w values and corresponding weights assigned to them: upper, mid and lower. Given M_w values of this figure are the middle M_w values.

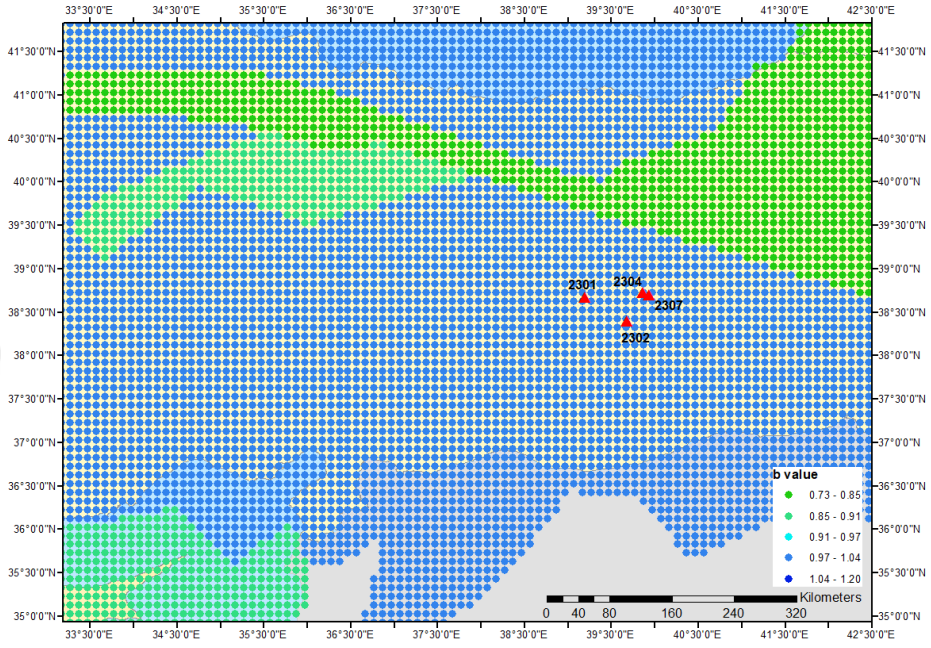

Figure 4.8 Guttenberg-Richter Earthquake Recurrence Model b-value assigned to the smoothed seismic sources of European Seismic Hazard Model 2020 in relation to the selected station sites of AFAD (i.e., 2301, 2302, 2304, 2307).

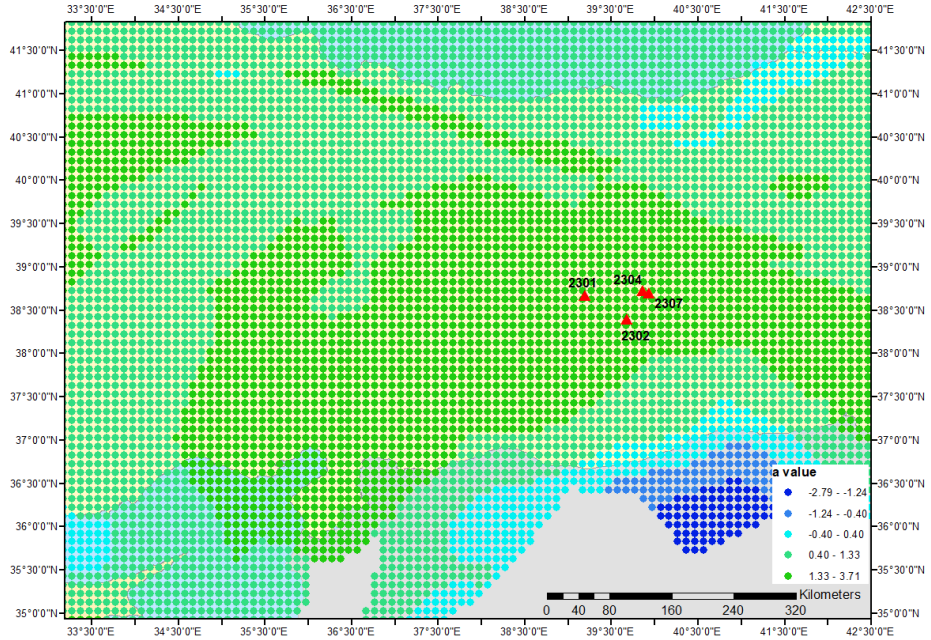

Figure 4.9 Guttenberg-Richter Earthquake Recurrence Model a-value assigned to the smoothed seismic sources of European Seismic Hazard Model 2020 in relation to the selected station sites of AFAD (i.e., 2301, 2302, 2304, 2307).

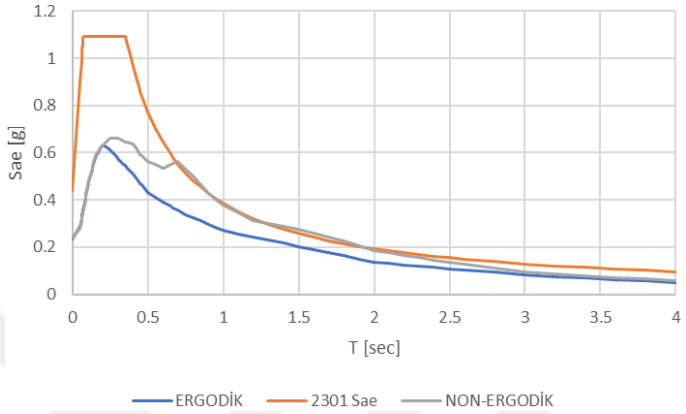

Figure 4.10 Comparison of uniform hazard spectra obtained for station site 2301 representing case 1 and case 3 seismic hazard assessment results for 475 years return period. Computed horizontal elastic design spectra for this site is given as well to allow comparison as prepared according to TBDY2018.

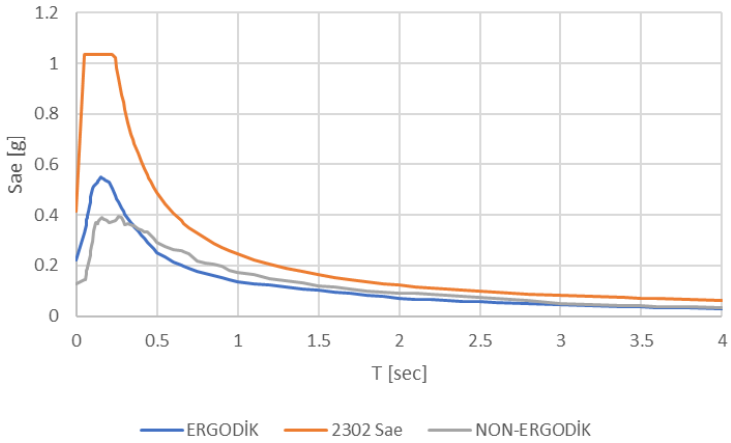

Figure 4.11 Comparison of uniform hazard spectra obtained for station site 2302 representing case 1 and case 3 seismic hazard assessment results for 475 years return period. Computed horizontal elastic design spectra for this site is given as well to allow comparison as prepared according to TBDY2018.

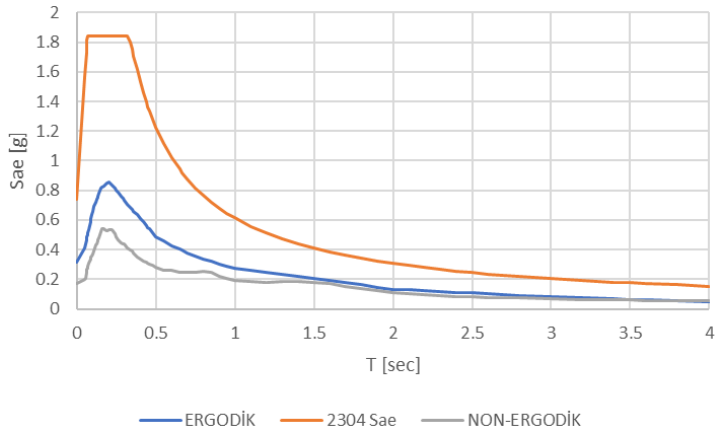

Figure 4.12 Comparison of uniform hazard spectra obtained for station site 2304 representing case 1 and case 3 seismic hazard assessment results for 475 years return period. Computed horizontal elastic design spectra for this site is given as well to allow comparison as prepared according to TBDY2018.

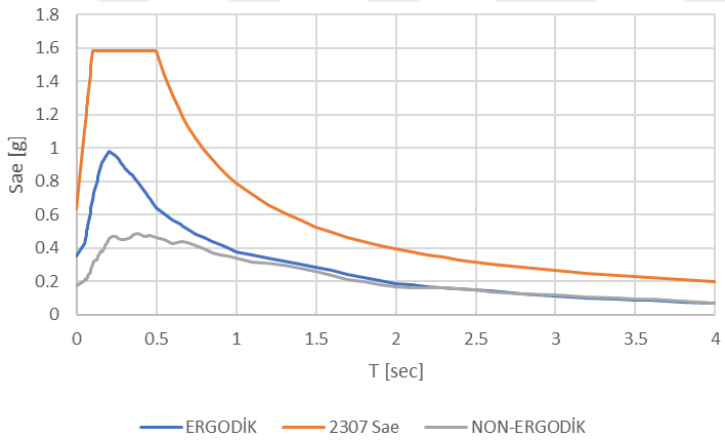

Figure 4.13 Comparison of uniform hazard spectra obtained for station site 2307 representing case 1 and case 3 seismic hazard assessment results for 475 years return period. Computed horizontal elastic design spectra for this site is given as well to allow comparison as prepared according to TBDY2018.

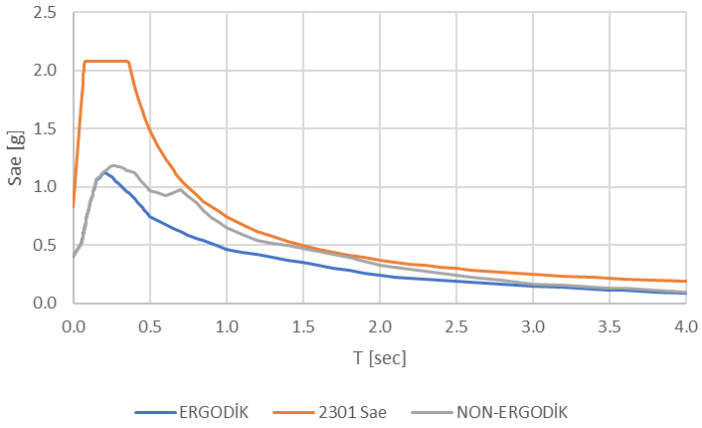

Figure 4.14 Comparison of uniform hazard spectra obtained for station site 2301 representing case 1 and case 3 seismic hazard assessment results for 2475 years return period. Computed horizontal elastic design spectra for this site is given as well to allow comparison as prepared according to TBDY2018.

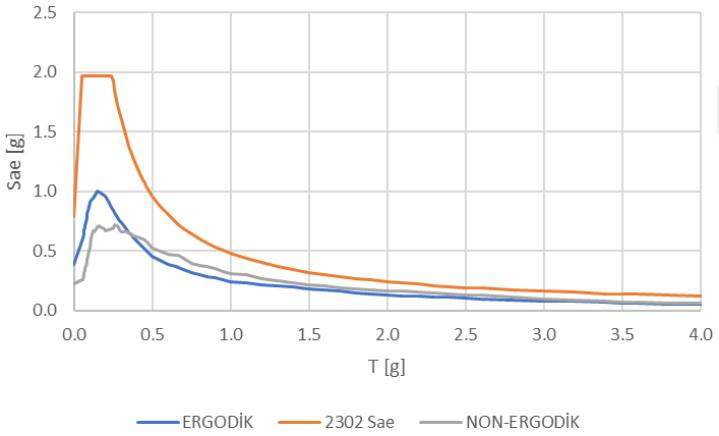

Figure 4.15 Comparison of uniform hazard spectra obtained for station site 2302 representing case 1 and case 3 seismic hazard assessment results for 2475 years return period. Computed horizontal elastic design spectra for this site is given as well to allow comparison as prepared according to TBDY2018.

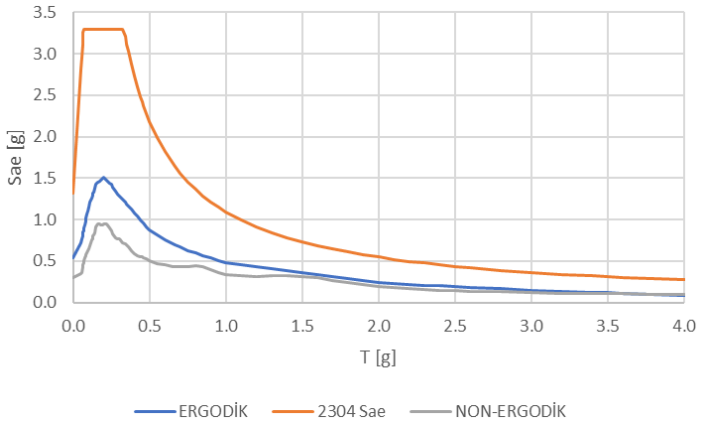

Figure 4.16 Comparison of uniform hazard spectra obtained for station site 2304 representing case 1 and case 3 seismic hazard assessment results for 2475 years return period. Computed horizontal elastic design spectra for this site is given as well to allow comparison as prepared according to TBDY2018.

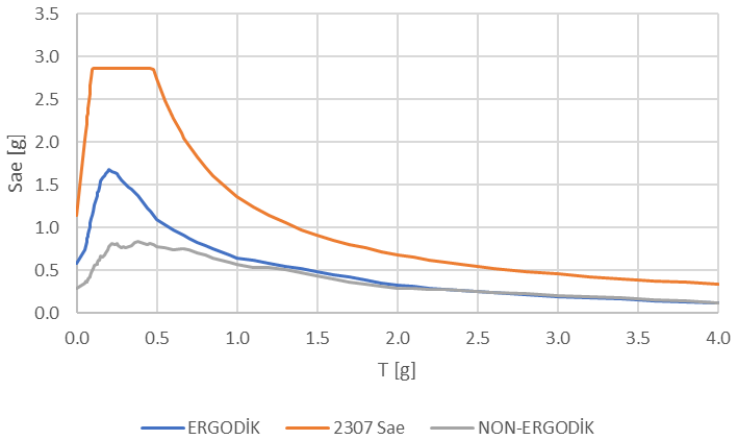

Figure 4.17 Comparison of uniform hazard spectra obtained for station site 2307 representing case 1 and case 3 seismic hazard assessment results for 2475 years return period. Computed horizontal elastic design spectra for this site is given as well to allow comparison as prepared according to TBDY2018.

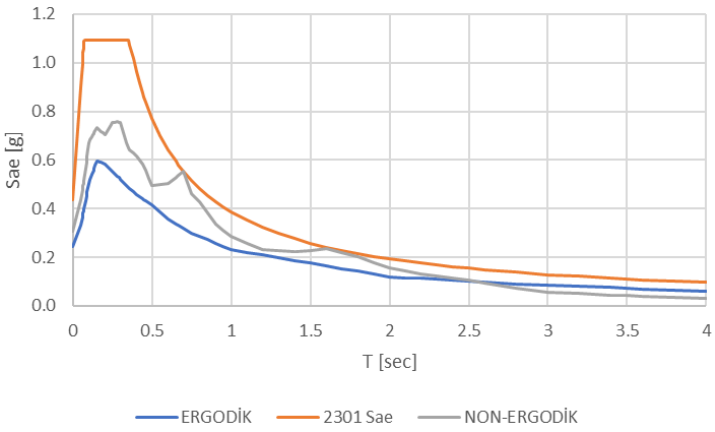

Figure 4.18 Comparison of uniform hazard spectra obtained for station site 2301 representing case 2 and case 5 seismic hazard assessment results for 475 years return period. Computed horizontal elastic design spectra for this site is given as well to allow comparison as prepared according to TBDY2018.

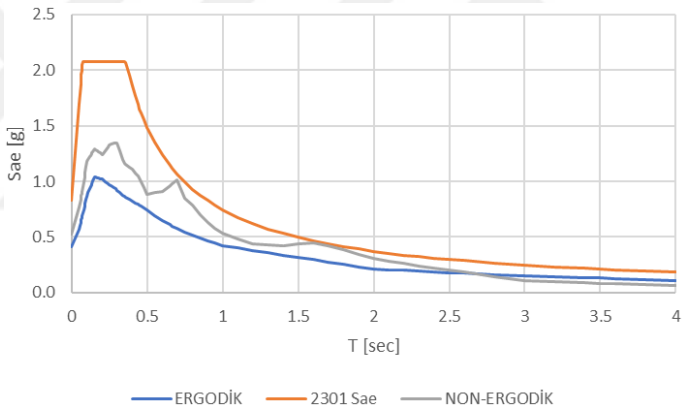

Figure 4.19 Comparison of uniform hazard spectra obtained for station site 2301 representing case 2 and case 5 seismic hazard assessment results for 2475 years return period. Computed horizontal elastic design spectra for this site is given as well to allow comparison as prepared according to TBDY2018.

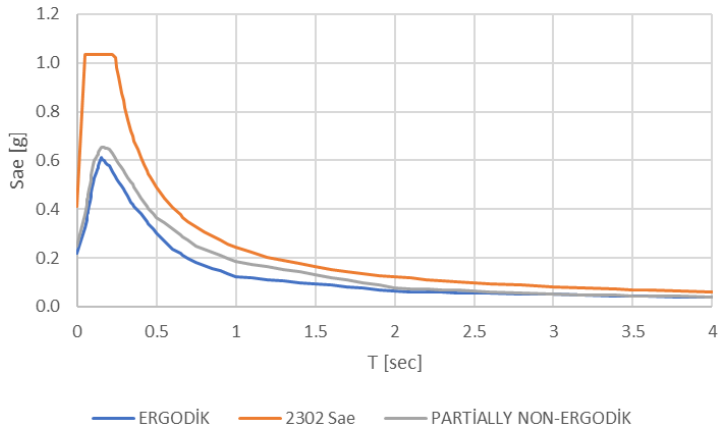

Figure 4.20 Comparison of uniform hazard spectra obtained for station site 2302 representing case 2 and case 4 seismic hazard assessment results for 475 years return period. Computed horizontal elastic design spectra for this site is given as well to allow comparison as prepared according to TBDY2018.

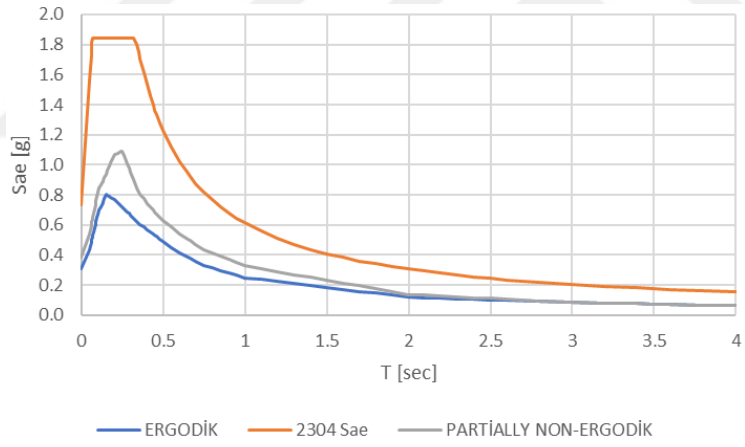

Figure 4.21 Comparison of uniform hazard spectra obtained for station site 2304 representing case 2 and case 4 seismic hazard assessment results for 475 years return period. Computed horizontal elastic design spectra for this site is given as well to allow comparison as prepared according to TBDY2018.

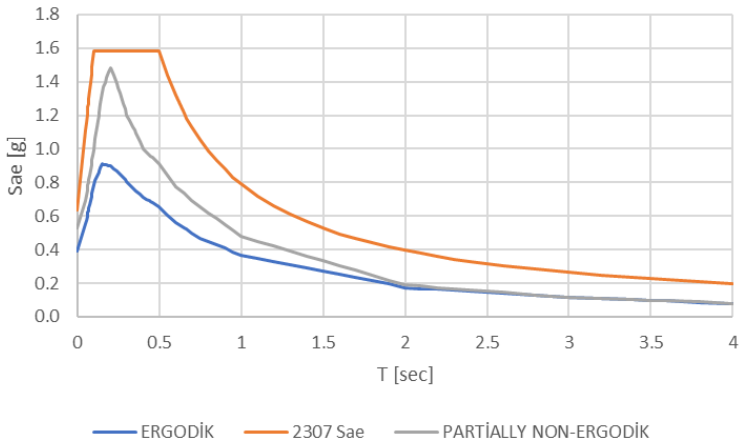

Figure 4.22 Comparison of uniform hazard spectra obtained for station site 2307 representing case 2 and case 4 seismic hazard assessment results for 475 years return period. Computed horizontal elastic design spectra for this site is given as well to allow comparison as prepared according to TBDY2018.

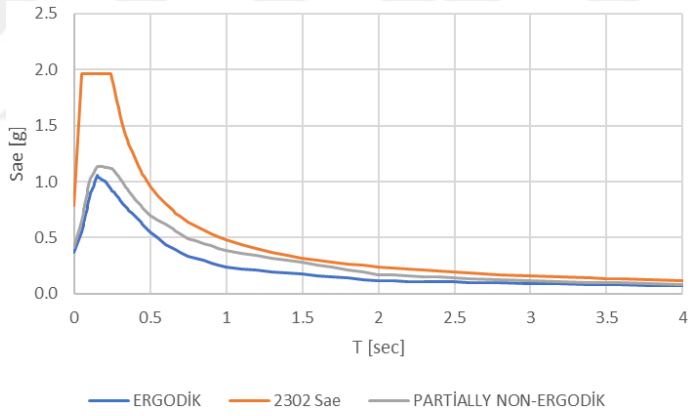

Figure 4.23 Comparison of uniform hazard spectra obtained for station site 2302 representing case 2 and case 4 seismic hazard assessment results for 2475 years return period. Computed horizontal elastic design spectra for this site is given as well to allow comparison as prepared according to TBDY2018.

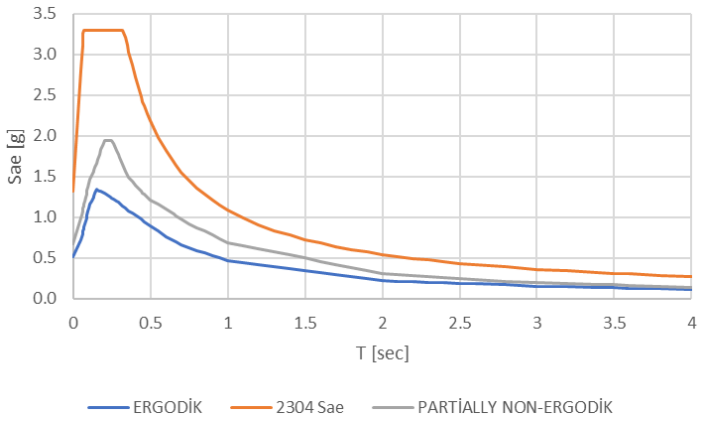

Figure 4.24 Comparison of uniform hazard spectra obtained for station site 2304 representing case 2 and case 4 seismic hazard assessment results for 2475 years return period. Computed horizontal elastic design spectra for this site is given as well to allow comparison as prepared according to TBDY2018.

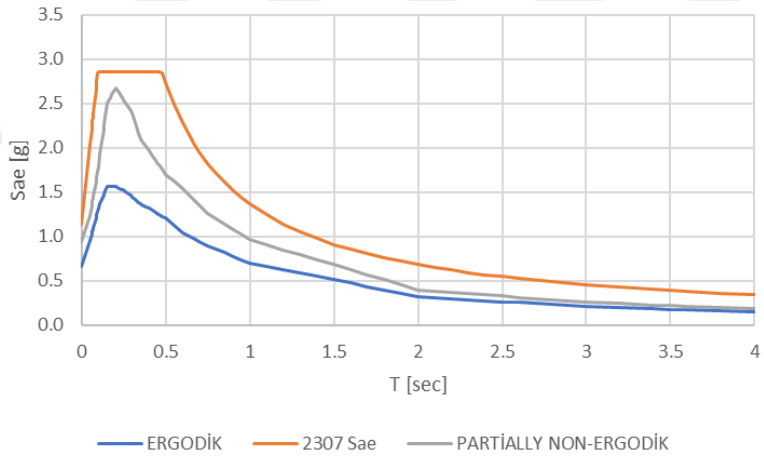

Figure 4.25 Comparison of uniform hazard spectra obtained for station site 2307 representing case 2 and case 4 seismic hazard assessment results for 2475 years return period. Computed horizontal elastic design spectra for this site is given as well to allow comparison as prepared according to TBDY2018.

In the subsequent section, the modeling of reinforced concrete buildings, for which the design has been carried out, will be elucidated. This will be accomplished through the utilization of the Sap2000 (Computers and Structures, Inc. v21.1.0) program.

CHAPTER 5

MODELLING

5.1 Modelling Nonlinear Behaviour of the Selected Structures

The SAP2000 (Computers and Structures, Inc. v21.1.0) structural analysis program was used to model the buildings. While modelling the selected buildings, beams, and columns are modelled as reinforced concrete frame elements, slabs are modelled as shell elements, and slabs are assumed to be infinitely rigid (Figure 5.1).

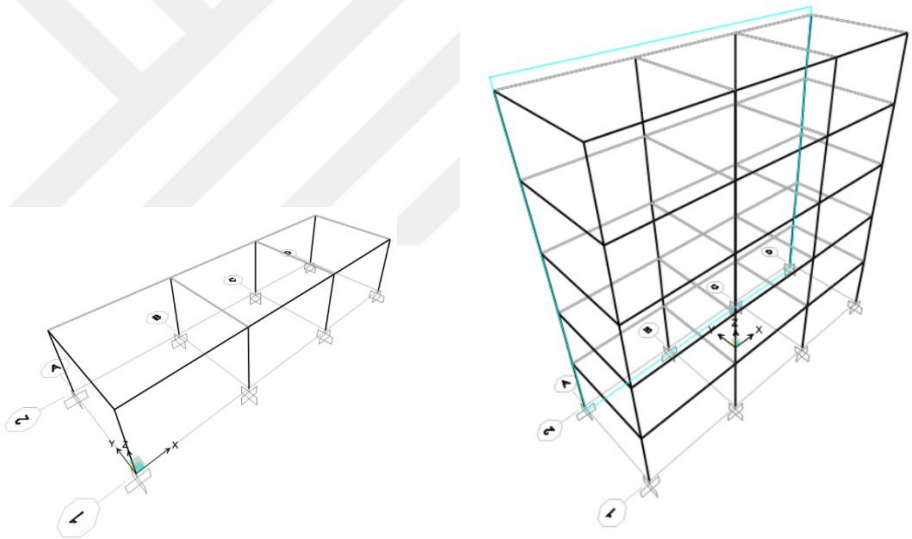

a) b)

Figure 5.1 The Sap2000 Model of a) Low-rise building b) Mid-Rise building

No specific foundation design has been carried out in this study. Fixed supports are defined at the ends of the ground floor columns to represent the foundation. Besides, brick walls in the selected buildings were not explicitly modelled. However, wall loads were defined on beams as part of defined dead load to represent weight of brick walls.

Beam and column reinforcements (Chapter 2, Figure 2.4-2.5) were modelled using the section designer tool of the Sap2000 program (Figure 5.2).

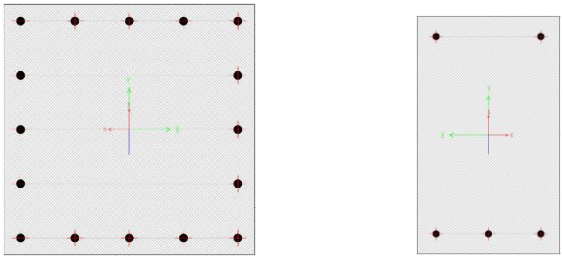

a) b)

Figure 5.2 Section designer view of a) a representative column section b) The mid-span section of a representative beam

The Sap2000 program accepts the modelled structural materials as linear elastic when analysis type is defined as such. However; while reinforced concrete elements show linear elastic behaviour up to a so defined yield point, these elements show plastic behaviour afterwards (Figure 5.3). In order to define this nonlinear behaviour, plastic hinges were added to the end points of the modelled load-bearing columns and beams, as described in TBEC (2018).

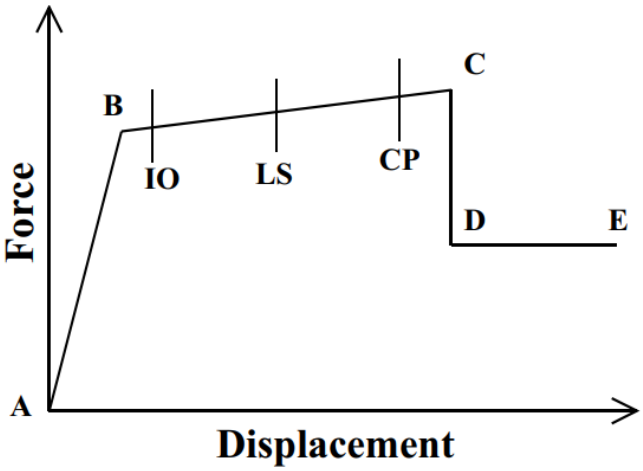

Figure 5.3 Force vs. Displacement curve, this type of curve can also be developed for Moment vs. Rotation (CSI Analysis Reference Manual, 2021, p.149).

Point A is the zero point. Point B in the figure represents yielding point. Up to this point, elastic deformation is observed at the hinge. Beyond this point, plastic deformation begins. Point C represents ultimate capacity of the element. If the deformation surpasses this point, a significant decrease occurs in the element's strength capacity. Point D indicates the remaining strength during analysis. Lastly, Point E represents the failure.

Beams are elements that are subjected to mainly bending. They are not exposed to axial loads as much as columns. Therefore, it is expected that beams may experience deformations due to flexural effects. To address this, moment plastic hinges were placed at the ends of the beams. Columns, on the other hand, are subjected to higher axial loads compared to beams. They are also exposed to bi-axial bending moments and shear forces. Thus, adding P-M-M hinges resulted in more realistic nonlinear material behaviour.

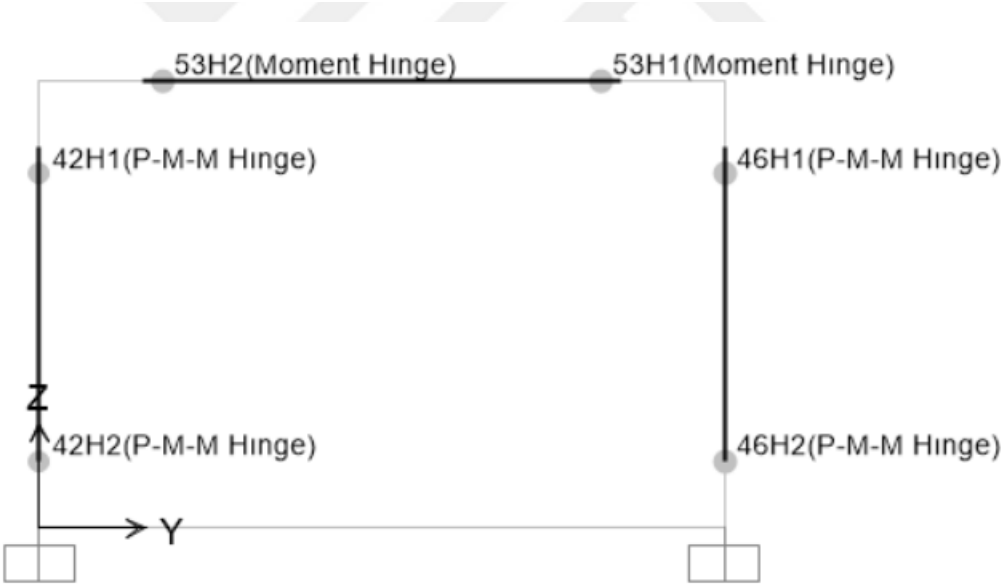

Figure 5.4 Moment and P-M-M hinges on the beams and columns, respectively.

Plastic deformation zone, called plastic hinge length (L_p), is taken to be equal to half of the cross-sectional dimension (h) along the active loading direction according to TBEC (2018).

The stiffness of columns and beams has been reduced as specified in the code (Table 5.1). The columns' effective section stiffness was scaled down by a factor of 0.7, and the beams' effective section stiffness was similarly decreased by multiplying it by 0.35. Besides all these, it should be underlined that P-Δ effects were not considered in the analysis.

Table 5.1 Effective Section Rigidity Multiplier Coefficients (Table 4.2 TBEC, 2018)

Reinforced Concrete System Element	Effective Section Rigidity Multiplier	
Shell-Slab (in-plane)	Axial	Shear
Shell	0,50	0,50
Basement Shell	0,80	0,50
Slab	0,25	0,25
Shell-Slab (out of plane)	Bending	Shear
Shell	0,25	1,00
Basement Shell	0,50	1,00
Slab	0,25	1,00
Frame Element	Bending	Shear
Tie Beam	0,15	1,00
Frame Beam	0,35	1,00
Frame Column	0,70	1,00
Shell (Equivalent Bar)	0,50	0,50

5.2 Materials

In the building models, concrete with a class of C30/37 and reinforcement of S420 have been utilized. The properties of the materials are provided below.

- Concrete Class C30/37

  Properties of Material:

  Weight per Unit Volume = 24,9926 KN

  Mass per Unit Volume = 2,5485 KN

  Modulus of Elasticity, E = 32000000 KN/m^2

  Poisson ratio, ν = 0,2

Coefficient of Thermal Expansion, α = 0,00001000 1/C

Shear Modulus, G = 13333333 KN/m^2

- Rebar Class S420

  Properties of Material:

  Weight per Unit Volume = 76,9729 KN

  Mass per Unit Volume = 7,849 KN

  Modulus of Elasticity, E = 199900000 KN/m^2

  Coefficient of Thermal Expansion, A =0 ,00001170 1/C

  Minimum Yield Stress, F_y = 413685,5 KN/m^2

  Minimum Tensile Stress, F_u = 620528,2 KN/m^2

  Expected Yield Stress, F_{ye} = 455054 KN/m^2

  Expected Tensile Stress, F_{ue} = 682581 KN/m^2

5.3 Loads and Load Combinations

The loads acting on the modelled buildings can be categorized into dead loads, live loads, and earthquake loads. The dead loads include the self-weight of the elements, wall and coating loads, and floor coating loads. The snow load and location changing loads (i.e., weight of occupants) were accounted for in the category of live loads. The snow load was only considered on the roof slab. The earthquake load was applied as a lateral load. Except for the earthquake load, all the other loads were applied to the models as distributed loads in the vertical direction (Figure 5.5).

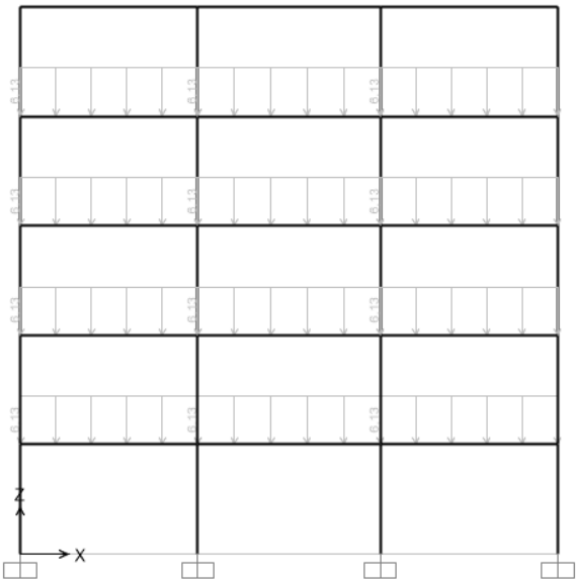

Figure 5.5 Example of distributed loads representing weight of brick walls acting on beams

Vertical and horizontal loads and load combinations acting on the modelled buildings are discussed in the following sections.

5.3.1 Loads

5.3.1.1 Vertical Loads (Dead Load & Live Load)

Dead loads and live loads values are taken from TS ISO 9194 (1997) and TS 498 (1997) specifications, respectively.

Slab

- Self load (G) 3,75 KN/m^2
- Coating Load (G) 2,01 KN/m^2
    - Marble coating (2cm) 0,56 KN/m^2
    - Levelling 1,05 KN/m^2
    - Plaster 0,4 KN/m^2
- Live load (Q) 2,00 KN/m^2

Roof slab

- Self load (G) 3,75 KN/m^2
- Coating load (G) 1,45 KN/m^2
  - Levelling 1,05 KN/m^2
  - Plaster 0,4 KN/m^2
- Snow load (Q) 1,50 KN/m^2

  (According to TS 498 (1997), Elazığ > 1000m altitude, III. Region, snow load 1,35 KN/m^2, increase snow load by 10%)
- Live load (Q) 1,50 KN/m^2

Outside Beam

- Self load (G) 3,75 KN/m
- 25 cm Autoclaved aerated concrete block wall load (G) 6,125 KN/m
  - Double-Brick (25cm) 4,375 KN/m
  - Outside Plaster (2cm) 1,00 KN/m
  - Inside Plaster (1,5 cm) 0,75 KN/m

Inside Beam

- Self load (G) 3,75 KN/m
- 10 cm Autoclaved aerated concrete block wall load (G) 3,25 KN/m
  - Single-Brick (10cm) 1,75 KN/m
  - Inside Plaster (1,5 cm) 0,75 KN/m
  - Inside Plaster (1,5 cm) 0,75 KN/m

5.3.1.2 Lateral Loads

Earthquake loading was obtained by selecting real earthquake records based on the response spectral acceleration spectra calculated using ergodic and non-ergodic PHSA. The selected earthquake records and their details are provided in chapter 6.

5.3.2 Load Combinations

Load combinations have been taken into account as defined by TS500 (2000) and TBEC (2018). The combinations are given in Table 5.2.

Table 5.2 Load Combinations Considered in the Models

COMB 1	1,4G + 1,4Q	(Eq 6.3 in TS500)
COMB 2	G + Q + EQ	(Eq 6.7 in TS500)
COMB 3	0,9G + EQ	(Eq 6.8 in TS500)
COMB 4	G + nQ + 0,2S + EQ	(Eq 4.11 in TEC18)

Vertical earthquake loading effects have been neglected in the study. The earthquake forces acting in horizontal directions have been considered in the combinations. "n" is the live load participation factor. According to TBEC (2018) Table 4.2, “n” has been determined as 0.3 (Table 5.3).

Table 5.3 Live Loads Participation Ratio

Buildings Usage Purpose	n
Warehouse, storehouse, etc.	0.80
School, dormitory, sport complex, cinema, theatre, concert hall, sanctuary, restaurant, shop, etc.	0.60
Residance, office, hotel, hospital, car park, etc.	0.30

5.4 Hysteresis Behaviour of Modelled Buildings

Hysteresis involves the dissipation of energy as a result of deformation or displacement, in contrast to viscosity, where energy dissipation occurs through the deformation rate. The hysteretic behaviour can have an impact on nonlinear time-history analysis results that involve load reversals and cyclic loading characteristics. Various hysteresis models exist to describe the behaviour of different materials (e.g. Elastic hysteresis model, isotropic hysteresis model, etc.). These models mainly differ in the amount of energy they dissipate during a specific deformation cycle and how their energy dissipation behaviour changes as the deformation increases.

In the moment and P-M-M hinges used in the modelled buildings, and Takeda hysteresis model has been employed. In this model, the amount of energy decreases with larger deformations. (Figure 5.6, https://docs.csiamerica.com/help-files/sap/Menus/Assign/Takeda_Hysteresis_Model.htm).

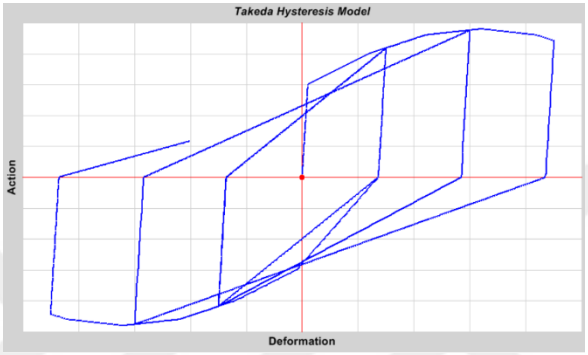

Figure 5.6 Takeda Hysteresis Model

5.5 Damping Models

Damping is the process of distributing and reducing vibrational energy of the structure. During structural analysis, various models are available to describe this effect (e.g. Rayleigh damping, Modal damping, etc.). In this study, the modal damping approach with mass and stiffness proportionality was adopted. To achieve this, the dominant periods in the X and Y directions of the buildings and the damping ratios were input into the program, creating a period-dependent model specific to the structure. The calculated data based on the periods is provided in Table 5.4.

Table 5.4 Damping Model Coefficients

		Period (sec)	Damping Ratio	Mass Proportional Coefficient (1/sec)	Stiffness Proportional Coefficient (sec)
Low-rise Building	X direction	0,1207	0,05	2,9453	0.00083
	Y direction	0,0926			
Mid-rise Building	X direction	0,5785	0,05	0,5589	0,00447
	Y direction	0,5457			

In the next section, the seismic forces and results of nonlinear analysis under various loads of buildings modeled using the Sap2000 program are discussed. This includes the methods employed for selecting earthquake records.

CHAPTER 6

NONLINEAR TIME HISTORY ANALYSIS AND RESULTS

6.1 Selected Ground Motions and Selection Process

In this section, earthquake records selected for the nonlinear time history analysis phase (NLTHA) will be discussed, along with the carried out nonlinear time history analyses and obtained outcomes. In order to conduct the analysis, it is necessary to select earthquake records that will affect the building models designed according to the design criteria explained in Chapter 2 and modelled in the SAP2000 program, as described in Chapter 5. The selection of earthquake records is based on the uniform hazard spectra obtained as a result of probabilistic seismic hazard assessment carried out by utilizing the OpenQuake program, as detailed in Chapter 4. In the NLTHA, uniform hazard spectra calculated for a return period of 2475 years were employed.

The earthquake records utilized in the analysis are actual records selected from the Pacific Earthquake Engineering Research Center (PEER) strong ground motion database. These records were chosen based on various criteria established for each station location and building model. These criteria that were established based on the dominant earthquake scenario for the selected locations are presented in Table 6.1.

Table 6.1 The Ground-Motion Selection Criteria

		2301	**2302**	**2304**	**2307**
Search Parameters	Magnitude	7-7,5	7-7,5	7-7,5	7-7,5
	R_{rup} (km)	0-50	0-50	0-40	0-30
	V_{s30} (m/s)	360-760	450-1100	360-760	180-360
	Pulse	NO	NO	NO	NO
Suite	Spectral Ord.	GeoMean	GeoMean	GeoMean	GeoMean
	Damping Ratio	5%	5%	5%	5%
	Suite Average	Geometric	Geometric	Geometric	Geometric
Scaling	Scaling Method	Minimize MSE	Minimize MSE	Minimize MSE	Minimize MSE
Weight Function		It depends on building type (Low-rise or Mid-rise building)			

In all the selected records, moment magnitudes fall within the range of 7 to 7.5. Rupture distances have been chosen as close to the main seismic source as possible (i.e., East Anatolian Fault). The V_{s30} values reflect the soil conditions at the station locations. Earthquake records lacking strong velocity pulses in the ground motion velocity-time graph were chosen. This approach effectively eliminated the fault rupture directivity effect. A phenomenon known as "directivity" occurs when a fault ruptures, producing an earthquake's ground motion that is more noticeable in the direction of the rupture than it is in the directions that are farther from the epicenter. Great care has been taken to ensure that the best match between the spectral accelerations of the selected records and the target spectral acceleration occurs within the range of periods chosen based on the 1st vibrational periods of modelled buildings. Therefore, weight function values of Table 6.1 have been assigned with this consideration in mind. Following the criteria described above for the selection of records, once the chosen records were determined, the scaling factor for each earthquake record was established through the method of logarithmic minimization of the difference between the spectral accelerations of the selected records and the target spectral acceleration (i.e., using the Mean Squared Error, MSE).

In accordance with TBEC18, a maximum of three records from a single earthquake event can be selected, resulting in the selection of a total of 11 strong motion records to perform NLTHA for each building model. Thus, a total of 220 earthquake records were selected from PEER for 2 different PSHA results (i.e., based on nonergodic Kale et al., 2015 and Kotha et al., 2022 GMPMs), 4 station sites, and 2 building types. The earthquake records selected from PEER strong motion database are provided in Table 6.2.

Tablo 6.2 Selected Ground-Motion Records From PEER

Tablo 6.2a Selected Ground-Motion Records From PEER strong motion site for station site 2301

	Earthquake Name	Year	Magnitude	Mechanism	Rjb (km)	Rrup (km)	Vs30 (m/sec)
KALE ERGODIC 2301 MID-RISE	"Duzce_ Turkey"	1999	7.14	strike slip	45.16	45.16	411.91
	"Manjil_ Iran"	1990	7.37	strike slip	12.55	12.55	723.95
	"Hector Mine"	1999	7.13	strike slip	41.81	43.05	382.93
	"Hector Mine"	1999	7.13	strike slip	10.35	11.66	726.0
	"Hector Mine"	1999	7.13	strike slip	31.06	31.06	379.32
	"Landers"	1992	7.28	strike slip	45.34	45.34	436.14
	"Landers"	1992	7.28	strike slip	26.95	26.95	367.84
	"Landers"	1992	7.28	strike slip	27.05	27.05	425.02
	"Darfield_ New Zealand"	2010	7.0	strike slip	43.6	43.6	638.39
	"Darfield_ New Zealand"	2010	7.0	strike slip	30.63	30.63	481.62
	"El Mayor-Cucapah_ Mexico"	2010	7.2	strike slip	31.79	32.22	503.0
KALE ERGODIC 2301 LOW-RISE	**Earthquake Name**	**Year**	**Magnitude**	**Mechanism**	**Rjb (km)**	**Rrup (km)**	**Vs30 (m/sec)**
	"Duzce_ Turkey"	1999	7.14	strike slip	23.41	23.41	517.0
	"Manjil_ Iran"	1990	7.37	strike slip	12.55	12.55	723.95
	"Hector Mine"	1999	7.13	strike slip	41.81	43.05	382.93
	"Hector Mine"	1999	7.13	strike slip	10.35	11.66	726.0
	"Hector Mine"	1999	7.13	strike slip	31.06	31.06	379.32
	"Landers"	1992	7.28	strike slip	45.34	45.34	436.14
	"Landers"	1992	7.28	strike slip	26.95	26.95	367.84
	"Landers"	1992	7.28	strike slip	27.05	27.05	425.02
	"Darfield_ New Zealand"	2010	7.0	strike slip	43.6	43.6	638.39
	"Darfield_ New Zealand"	2010	7.0	strike slip	30.63	30.63	481.62
	"El Mayor-Cucapah_ Mexico"	2010	7.2	strike slip	31.79	32.22	503.0

Tablo 6.2b Selected Ground-Motion Records From PEER strong motion site for station site 2302

	Earthquake Name	Year	Magnitude	Mechanism	Rjb (km)	Rrup (km)	Vs30 (m/sec)
KALE ERGODIC 2302 MID-RISE	"Landers"	1992	7.28	strike slip	41.43	41.43	635.01
	"Duzce_ Turkey"	1999	7.14	strike slip	4.17	4.17	551.3
	"Duzce_ Turkey"	1999	7.14	strike slip	11.46	11.46	481.0
	"Duzce_ Turkey"	1999	7.14	strike slip	8.03	8.03	638.39
	"Manjil_ Iran"	1990	7.37	strike slip	12.55	12.55	723.95
	"Hector Mine"	1999	7.13	strike slip	10.35	11.66	726.0
	"Hector Mine"	1999	7.13	strike slip	42.06	42.06	635.01
	"El Mayor-Cucapah_ Mexico"	2010	7.2	strike slip	43.64	45.47	523.99
	"Darfield_ New Zealand"	2010	7.0	strike slip	43.6	43.6	638.39
	"Darfield_ New Zealand"	2010	7.0	strike slip	30.63	30.63	481.62
	"El Mayor-Cucapah_ Mexico"	2010	7.2	strike slip	31.79	32.22	503.0
KALE ERGODIC 2302 LOW-RISE	**Earthquake Name**	**Year**	**Magnitude**	**Mechanism**	**Rjb (km)**	**Rrup (km)**	**Vs30 (m/sec)**
	"Landers"	1992	7.28	strike slip	41.43	41.43	635.01
	"Duzce_ Turkey"	1999	7.14	strike slip	4.17	4.17	551.3
	"Duzce_ Turkey"	1999	7.14	strike slip	11.46	11.46	481.0
	"Duzce_ Turkey"	1999	7.14	strike slip	8.03	8.03	638.39
	"Manjil_ Iran"	1990	7.37	strike slip	12.55	12.55	723.95
	"Hector Mine"	1999	7.13	strike slip	10.35	11.66	726.0
	"Hector Mine"	1999	7.13	strike slip	42.06	42.06	635.01
	"El Mayor-Cucapah_ Mexico"	2010	7.2	strike slip	43.64	45.47	523.99
	"Darfield_ New Zealand"	2010	7.0	strike slip	43.6	43.6	638.39
	"Darfield_ New Zealand"	2010	7.0	strike slip	30.63	30.63	481.62
	"El Mayor-Cucapah_ Mexico"	2010	7.2	strike slip	31.79	32.22	503.0

Tablo 6.2c Selected Ground-Motion Records From PEER strong motion site for station site 2304

	Earthquake Name	Year	Magnitude	Mechanism	Rjb (km)	Rrup (km)	Vs30 (m/sec)
KALE ERGODIC 2304 MID-RISE	"Duzce_ Turkey"	1999	7.14	strike slip	4.17	4.17	551.3
	"Duzce_ Turkey"	1999	7.14	strike slip	11.46	11.46	481.0
	"Duzce_ Turkey"	1999	7.14	strike slip	8.03	8.03	638.39
	"Manjil_ Iran"	1990	7.37	strike slip	12.55	12.55	723.95
	"Hector Mine"	1999	7.13	strike slip	10.35	11.66	726.0
	"Hector Mine"	1999	7.13	strike slip	31.06	31.06	379.32
	"Landers"	1992	7.28	strike slip	26.95	26.95	367.84
	"Landers"	1992	7.28	strike slip	27.05	27.05	425.02
	"Darfield_ New Zealand"	2010	7.0	strike slip	30.63	30.63	481.62
	"Darfield_ New Zealand"	2010	7.0	strike slip	29.86	29.86	389.54
	"El Mayor-Cucapah_ Mexico"	2010	7.2	strike slip	31.79	32.22	503.0
KALE ERGODIC 2304 LOW-RISE	**Earthquake Name**	**Year**	**Magnitude**	**Mechanism**	**Rjb (km)**	**Rrup (km)**	**Vs30 (m/sec)**
	"Duzce_ Turkey"	1999	7.14	strike slip	4.17	4.17	551.3
	"Duzce_ Turkey"	1999	7.14	strike slip	11.46	11.46	481.0
	"Duzce_ Turkey"	1999	7.14	strike slip	8.03	8.03	638.39
	"Manjil_ Iran"	1990	7.37	strike slip	12.55	12.55	723.95
	"Hector Mine"	1999	7.13	strike slip	10.35	11.66	726.0
	"Hector Mine"	1999	7.13	strike slip	31.06	31.06	379.32
	"Landers"	1992	7.28	strike slip	26.95	26.95	367.84
	"Landers"	1992	7.28	strike slip	27.05	27.05	425.02
	"Darfield_ New Zealand"	2010	7.0	strike slip	30.63	30.63	481.62
	"Darfield_ New Zealand"	2010	7.0	strike slip	29.86	29.86	389.54
	"El Mayor-Cucapah_ Mexico"	2010	7.2	strike slip	31.79	32.22	503.0

Tablo 6.2d Selected Ground-Motion Records From PEER strong motion site for station site 2307

	Earthquake Name	Year	Magnitude	Mechanism	Rjb (km)	Rrup (km)	Vs30 (m/sec)
KALE ERGODIC 2307 MID-RISE	"Landers"	1992	7.28	strike slip	21.78	21.78	359.0
	"Landers"	1992	7.28	strike slip	26.96	26.96	355.42
	"Landers"	1992	7.28	strike slip	26.84	26.84	344.67
	"Duzce_ Turkey"	1999	7.14	strike slip	0.0	6.58	281.86
	"Duzce_ Turkey"	1999	7.14	strike slip	9.14	9.14	338.0
	"El Mayor-Cucapah_ Mexico"	2010	7.2	strike slip	13.21	15.91	242.05
	"El Mayor-Cucapah_ Mexico"	2010	7.2	strike slip	27.42	27.91	210.51
	"El Mayor-Cucapah_ Mexico"	2010	7.2	strike slip	27.81	28.3	276.25
	"Darfield_ New Zealand"	2010	7.0	strike slip	17.64	17.64	204.0
	"Darfield_ New Zealand"	2010	7.0	strike slip	13.37	16.47	295.74
	"Darfield_ New Zealand"	2010	7.0	strike slip	21.31	24.34	263.2
KALE ERGODIC 2307 LOW-RISE	**Earthquake Name**	**Year**	**Magnitude**	**Mechanism**	**Rjb (km)**	**Rrup (km)**	**Vs30 (m/sec)**
	"Landers"	1992	7.28	strike slip	21.78	21.78	359.0
	"Landers"	1992	7.28	strike slip	26.96	26.96	355.42
	"Landers"	1992	7.28	strike slip	26.84	26.84	344.67
	"Duzce_ Turkey"	1999	7.14	strike slip	0.0	6.58	281.86
	"Duzce_ Turkey"	1999	7.14	strike slip	9.14	9.14	338.0
	"El Mayor-Cucapah_ Mexico"	2010	7.2	strike slip	18.21	19.47	242.05
	"El Mayor-Cucapah_ Mexico"	2010	7.2	strike slip	27.42	27.91	210.51
	"El Mayor-Cucapah_ Mexico"	2010	7.2	strike slip	27.81	28.3	276.25
	"Darfield_ New Zealand"	2010	7.0	strike slip	17.64	17.64	204.0
	"Darfield_ New Zealand"	2010	7.0	strike slip	13.37	16.47	295.74
	"Darfield_ New Zealand"	2010	7.0	strike slip	21.31	24.34	263.2

Tablo 6.2e Selected Ground-Motion Records From PEER strong motion site for station site 2301

	Earthquake Name	Year	Magnitude	Mechanism	Rjb (km)	Rrup (km)	Vs30 (m/sec)
KALE NONERGODIC 2301 MID-RISE	"Landers"	1992	7.28	strike slip	11.03	11.03	379.32
	"Duzce_ Turkey"	1999	7.14	strike slip	0.21	0.21	529.18
	"Duzce_ Turkey"	1999	7.14	strike slip	23.41	23.41	517.0
	"Hector Mine"	1999	7.13	strike slip	41.81	43.05	382.93
	"Hector Mine"	1999	7.13	strike slip	10.35	11.66	726.0
	"Hector Mine"	1999	7.13	strike slip	31.06	31.06	379.32
	"Landers"	1992	7.28	strike slip	40.67	40.67	368.2
	"Landers"	1992	7.28	strike slip	26.95	26.95	367.84
	"Darfield_ New Zealand"	2010	7.0	strike slip	43.6	43.6	638.39
	"Darfield_ New Zealand"	2010	7.0	strike slip	30.63	30.63	481.62
	"Darfield_ New Zealand"	2010	7.0	strike slip	29.86	29.86	389.54
KALE NONERGODIC 2301 LOW-RISE	**Earthquake Name**	**Year**	**Magnitude**	**Mechanism**	**Rjb (km)**	**Rrup (km)**	**Vs30 (m/sec)**
	"Landers"	1992	7.28	strike slip	11.03	11.03	379.32
	"Duzce_ Turkey"	1999	7.14	strike slip	23.41	23.41	517.0
	"Hector Mine"	1999	7.13	strike slip	41.81	43.05	382.93
	"Hector Mine"	1999	7.13	strike slip	10.35	11.66	726.0
	"Hector Mine"	1999	7.13	strike slip	31.06	31.06	379.32
	"Landers"	1992	7.28	strike slip	40.67	40.67	368.2
	"Landers"	1992	7.28	strike slip	26.95	26.95	367.84
	"Darfield_ New Zealand"	2010	7.0	strike slip	43.6	43.6	638.39
	"Darfield_ New Zealand"	2010	7.0	strike slip	30.63	30.63	481.62
	"Darfield_ New Zealand"	2010	7.0	strike slip	29.86	29.86	389.54
	"El Mayor-Cucapah_ Mexico"	2010	7.2	strike slip	31.79	32.22	503.0

Tablo 6.2f Selected Ground-Motion Records From PEER strong motion site for station site 2302

	Earthquake Name	Year	Magnitude	Mechanism	Rjb (km)	Rrup (km)	Vs30 (m/sec)
KALE NONERGODIC 2302 MID-RISE	"Landers"	1992	7.28	strike slip	41.43	41.43	635.01
	"Duzce_ Turkey"	1999	7.14	strike slip	25.78	25.88	782.0
	"Duzce_ Turkey"	1999	7.14	strike slip	23.41	23.41	517.0
	"Duzce_ Turkey"	1999	7.14	strike slip	34.3	34.3	535.24
	"Manjil_ Iran"	1990	7.37	strike slip	12.55	12.55	723.95
	"Hector Mine"	1999	7.13	strike slip	10.35	11.66	726.0
	"Hector Mine"	1999	7.13	strike slip	42.06	42.06	635.01
	"El Mayor-Cucapah_ Mexico"	2010	7.2	strike slip	43.64	45.47	523.99
	"Darfield_ New Zealand"	2010	7.0	strike slip	43.6	43.6	638.39
	"Darfield_ New Zealand"	2010	7.0	strike slip	30.63	30.63	481.62
	"El Mayor-Cucapah_ Mexico"	2010	7.2	strike slip	31.79	32.22	503.0
KALE NONERGODIC 2302 LOW-RISE	**Earthquake Name**	**Year**	**Magnitude**	**Mechanism**	**Rjb (km)**	**Rrup (km)**	**Vs30 (m/sec)**
	"Landers"	1992	7.28	strike slip	41.43	41.43	635.01
	"Duzce_ Turkey"	1999	7.14	strike slip	25.78	25.88	782.0
	"Duzce_ Turkey"	1999	7.14	strike slip	23.41	23.41	517.0
	"Duzce_ Turkey"	1999	7.14	strike slip	34.3	34.3	535.24
	"Manjil_ Iran"	1990	7.37	strike slip	12.55	12.55	723.95
	"Hector Mine"	1999	7.13	strike slip	10.35	11.66	726.0
	"Hector Mine"	1999	7.13	strike slip	42.06	42.06	635.01
	"El Mayor-Cucapah_ Mexico"	2010	7.2	strike slip	43.64	45.47	523.99
	"Darfield_ New Zealand"	2010	7.0	strike slip	43.6	43.6	638.39
	"Darfield_ New Zealand"	2010	7.0	strike slip	30.63	30.63	481.62
	"El Mayor-Cucapah_ Mexico"	2010	7.2	strike slip	31.79	32.22	503.0

Tablo 6.2g Selected Ground-Motion Records From PEER strong motion site for station site 2304

	Earthquake Name	Year	Magnitude	Mechanism	Rjb (km)	Rrup (km)	Vs30 (m/sec)
KALE NONERGODIC 2304 MID-RISE	"Duzce_ Turkey"	1999	7.14	strike slip	0.21	0.21	529.18
	"Duzce_ Turkey"	1999	7.14	strike slip	11.46	11.46	481.0
	"Duzce_ Turkey"	1999	7.14	strike slip	23.41	23.41	517.0
	"Manjil_ Iran"	1990	7.37	strike slip	12.55	12.55	723.95
	"Hector Mine"	1999	7.13	strike slip	10.35	11.66	726.0
	"Hector Mine"	1999	7.13	strike slip	31.06	31.06	379.32
	"Landers"	1992	7.28	strike slip	26.95	26.95	367.84
	"Landers"	1992	7.28	strike slip	27.05	27.05	425.02
	"Darfield_ New Zealand"	2010	7.0	strike slip	30.63	30.63	481.62
	"Darfield_ New Zealand"	2010	7.0	strike slip	29.86	29.86	389.54
	"El Mayor-Cucapah_ Mexico"	2010	7.2	strike slip	31.79	32.22	503.0
KALE NONERGODIC 2304 LOW-RISE	**Earthquake Name**	**Year**	**Magnitude**	**Mechanism**	**Rjb (km)**	**Rrup (km)**	**Vs30 (m/sec)**
	"Duzce_ Turkey"	1999	7.14	strike slip	0.21	0.21	529.18
	"Duzce_ Turkey"	1999	7.14	strike slip	11.46	11.46	481.0
	"Duzce_ Turkey"	1999	7.14	strike slip	23.41	23.41	517.0
	"Manjil_ Iran"	1990	7.37	strike slip	12.55	12.55	723.95
	"Hector Mine"	1999	7.13	strike slip	10.35	11.66	726.0
	"Hector Mine"	1999	7.13	strike slip	31.06	31.06	379.32
	"Landers"	1992	7.28	strike slip	26.95	26.95	367.84
	"Landers"	1992	7.28	strike slip	27.05	27.05	425.02
	"Darfield_ New Zealand"	2010	7.0	strike slip	30.63	30.63	481.62
	"Darfield_ New Zealand"	2010	7.0	strike slip	29.86	29.86	389.54
	"El Mayor-Cucapah_ Mexico"	2010	7.2	strike slip	31.79	32.22	503.0

Tablo 6.2h Selected Ground-Motion Records From PEER strong motion site for station site 2307

	Earthquake Name	Year	Magnitude	Mechanism	Rjb (km)	Rrup (km)	Vs30 (m/sec)
KALE NONERGODIC 2307 MID-RISE	"Landers"	1992	7.28	strike slip	21.78	21.78	359.0
	"Landers"	1992	7.28	strike slip	26.96	26.96	355.42
	"Landers"	1992	7.28	strike slip	26.84	26.84	344.67
	"Duzce_ Turkey"	1999	7.14	strike slip	0.0	6.58	281.86
	"Duzce_ Turkey"	1999	7.14	strike slip	9.14	9.14	338.0
	"El Mayor-Cucapah_ Mexico"	2010	7.2	strike slip	18.21	19.47	242.05
	"El Mayor-Cucapah_ Mexico"	2010	7.2	strike slip	14.8	17.32	242.05
	"El Mayor-Cucapah_ Mexico"	2010	7.2	strike slip	19.12	20.46	231.23
	"Darfield_ New Zealand"	2010	7.0	strike slip	9.38	12.52	295.74
	"Darfield_ New Zealand"	2010	7.0	strike slip	24.55	24.55	206.0
	"Darfield_ New Zealand"	2010	7.0	strike slip	24.36	26.93	344.02
KALE NONERGODIC 2307 LOW-RISE	**Earthquake Name**	**Year**	**Magnitude**	**Mechanism**	**Rjb (km)**	**Rrup (km)**	**Vs30 (m/sec)**
	"Landers"	1992	7.28	strike slip	21.78	21.78	359.0
	"Landers"	1992	7.28	strike slip	26.96	26.96	355.42
	"Landers"	1992	7.28	strike slip	26.84	26.84	344.67
	"Duzce_ Turkey"	1999	7.14	strike slip	0.0	6.58	281.86
	"Duzce_ Turkey"	1999	7.14	strike slip	9.14	9.14	338.0
	"El Mayor-Cucapah_ Mexico"	2010	7.2	strike slip	18.21	19.47	242.05
	"El Mayor-Cucapah_ Mexico"	2010	7.2	strike slip	14.8	17.32	242.05
	"El Mayor-Cucapah_ Mexico"	2010	7.2	strike slip	19.12	20.46	231.23
	"Darfield_ New Zealand"	2010	7.0	strike slip	9.38	12.52	295.74
	"Darfield_ New Zealand"	2010	7.0	strike slip	24.55	24.55	206.0
	"Darfield_ New Zealand"	2010	7.0	strike slip	24.36	26.93	344.02

Tablo 6.2i Selected Ground-Motion Records From PEER strong motion site for station site 2301

	Earthquake Name	Year	Magnitude	Mechanism	Rjb (km)	Rrup (km)	Vs30 (m/sec)
KOTHA ERGODIC 2301 MID-RISE	"Duzce_ Turkey"	1999	7.14	strike slip	45.16	45.16	411.91
	"Manjil_ Iran"	1990	7.37	strike slip	12.55	12.55	723.95
	"Hector Mine"	1999	7.13	strike slip	41.81	43.05	382.93
	"Hector Mine"	1999	7.13	strike slip	10.35	11.66	726.0
	"Hector Mine"	1999	7.13	strike slip	42.06	42.06	635.01
	"Landers"	1992	7.28	strike slip	45.34	45.34	436.14
	"Landers"	1992	7.28	strike slip	26.95	26.95	367.84
	"Landers"	1992	7.28	strike slip	27.05	27.05	425.02
	"Darfield_ New Zealand"	2010	7.0	strike slip	43.6	43.6	638.39
	"Darfield_ New Zealand"	2010	7.0	strike slip	30.63	30.63	481.62
	"El Mayor-Cucapah_ Mexico"	2010	7.2	strike slip	31.79	32.22	503.0
KOTHA ERGODIC 2301 LOW-RISE	**Earthquake Name**	**Year**	**Magnitude**	**Mechanism**	**Rjb (km)**	**Rrup (km)**	**Vs30 (m/sec)**
	"Duzce_ Turkey"	1999	7.14	strike slip	45.16	45.16	411.91
	"Manjil_ Iran"	1990	7.37	strike slip	12.55	12.55	723.95
	"Hector Mine"	1999	7.13	strike slip	41.81	43.05	382.93
	"Hector Mine"	1999	7.13	strike slip	10.35	11.66	726.0
	"Hector Mine"	1999	7.13	strike slip	42.06	42.06	635.01
	"Landers"	1992	7.28	strike slip	45.34	45.34	436.14
	"Landers"	1992	7.28	strike slip	26.95	26.95	367.84
	"Landers"	1992	7.28	strike slip	27.05	27.05	425.02
	"Darfield_ New Zealand"	2010	7.0	strike slip	43.6	43.6	638.39
	"Darfield_ New Zealand"	2010	7.0	strike slip	30.63	30.63	481.62
	"El Mayor-Cucapah_ Mexico"	2010	7.2	strike slip	31.79	32.22	503.0

Tablo 6.2j Selected Ground-Motion Records From PEER strong motion site for station site 2301

	Earthquake Name	Year	Magnitude	Mechanism	Rjb (km)	Rrup (km)	Vs30 (m/sec)
KOTHA NONERGODIC 2301 MID-RISE	"Duzce_ Turkey"	1999	7.14	strike slip	11.46	11.46	481.0
	"Duzce_ Turkey"	1999	7.14	strike slip	45.16	45.16	411.91
	"Manjil_ Iran"	1990	7.37	strike slip	12.55	12.55	723.95
	"Hector Mine"	1999	7.13	strike slip	10.35	11.66	726.0
	"Hector Mine"	1999	7.13	strike slip	42.06	42.06	635.01
	"Landers"	1992	7.28	strike slip	45.34	45.34	436.14
	"Landers"	1992	7.28	strike slip	26.95	26.95	367.84
	"Landers"	1992	7.28	strike slip	27.05	27.05	425.02
	"El Mayor-Cucapah_ Mexico"	2010	7.2	strike slip	43.64	45.47	523.99
	"Darfield_ New Zealand"	2010	7.0	strike slip	30.63	30.63	481.62
	"El Mayor-Cucapah_ Mexico"	2010	7.2	strike slip	31.79	32.22	503.0
KOTHA NONERGODIC 230 LOW-RISE	**Earthquake Name**	**Year**	**Magnitude**	**Mechanism**	**Rjb (km)**	**Rrup (km)**	**Vs30 (m/sec)**
	"Duzce_ Turkey"	1999	7.14	strike slip	11.46	11.46	481.0
	"Duzce_ Turkey"	1999	7.14	strike slip	45.16	45.16	411.91
	"Manjil_ Iran"	1990	7.37	strike slip	12.55	12.55	723.95
	"Hector Mine"	1999	7.13	strike slip	10.35	11.66	726.0
	"Hector Mine"	1999	7.13	strike slip	42.06	42.06	635.01
	"Landers"	1992	7.28	strike slip	45.34	45.34	436.14
	"Landers"	1992	7.28	strike slip	26.95	26.95	367.84
	"Landers"	1992	7.28	strike slip	27.05	27.05	425.02
	"El Mayor-Cucapah_ Mexico"	2010	7.2	strike slip	43.64	45.47	523.99
	"Darfield_ New Zealand"	2010	7.0	strike slip	30.63	30.63	481.62
	"El Mayor-Cucapah_ Mexico"	2010	7.2	strike slip	31.79	32.22	503.0

6.2 Nonlinear Time History Analysis & Results

The acceleration-time series of the selected strong motion records were assigned as horizontal load functions in the Sap2000 program, and nonlinear time history analysis (NLTHA) was conducted on the 3D building models. Time-history analysis is utilized to assess the dynamic response of a building under loads that vary according to a specific time function. The nonlinear behavior of the structure consists of two components: geometric nonlinearity and material nonlinearity. Geometric nonlinearity considers the P-Δ effect. In the case of a sufficiently long structure, lateral displacements lead to the definition of additional load effects imposed on the vertical structural elements as a result of these displacements. This situation reduces deformation capacity while amplifying story drift. These additional load effects above a certain threshold need to be mitigated through design measures in the structural design process. In the scope of this study, the P-Δ effect has not been considered. Material nonlinearity is closely connected to the inelastic response of a constituent or system. The inelastic behavior can be identified by a correlation between force and deformation. In the models, this effect is represented using plastic hinges. The details are specified in Chapter 5.

In the analyses, the direct integration time history analysis method was employed. In this specific approach to dynamic analysis, the equations governing the stability of a structure are thoroughly integrated, considering the structure's interaction with dynamic loads. Prior to commencing the analysis, the initial condition of the structure was chosen as the starting state under the influence of vertical loads only, with a non-linear condition.

As a result of the analyses, the maximum storey displacements of building models, inter-story drift ratios, max. base shear/building weight values, and the plastic rotations of structural elements were computed and examined. The results and figures of the conducted analyses are presented below.

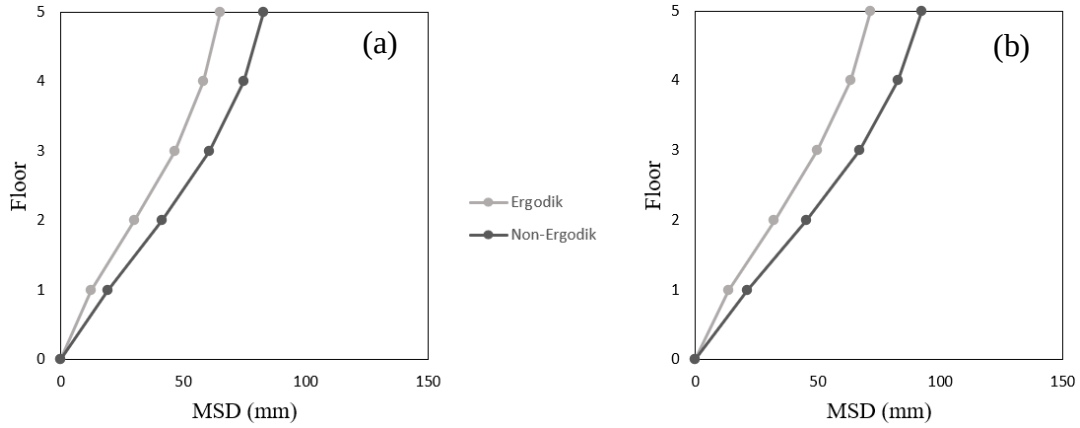

(1) Maximum storey displacements for the 5 storey building model at station site 2301 under strong motion records selected based on nonergodic and ergodic PSHA results based on Kale et al. (2015) study (a) Long. Dir. (b) Trans. Dir.

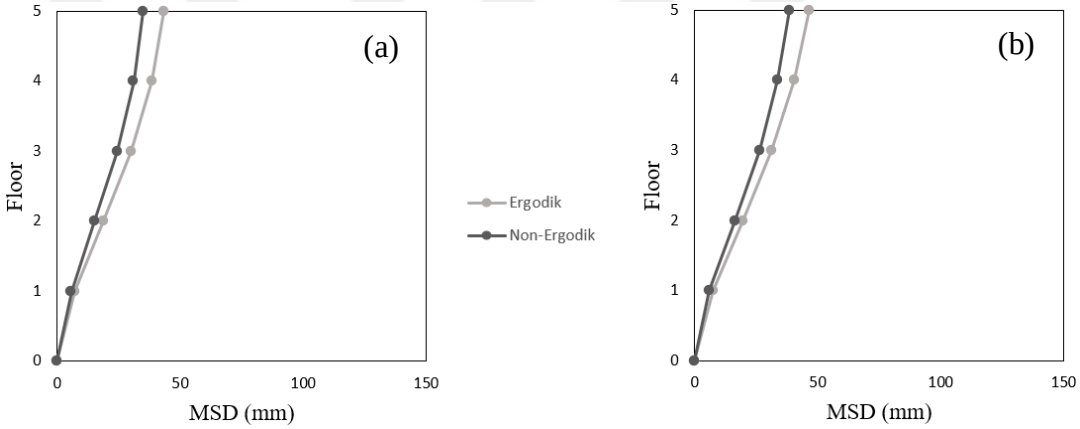

(2) Maximum storey displacements for the 5 storey building model at station site 2302 under strong motion records selected based on nonergodic and ergodic PSHA results based on Kale et al. (2015) study (a) Long. Dir. (b) Trans. Dir.

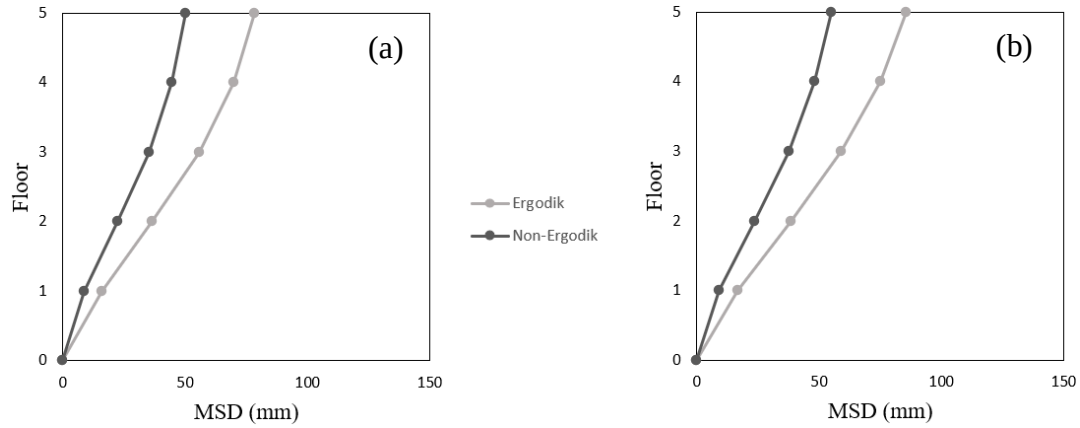

(3) Maximum storey displacements for the 5 storey building model at station site 2304

under strong motion records selected based on nonergodic and ergodic PSHA results based on Kale et al. (2015) study (a) Long. Dir. (b) Trans. Dir.

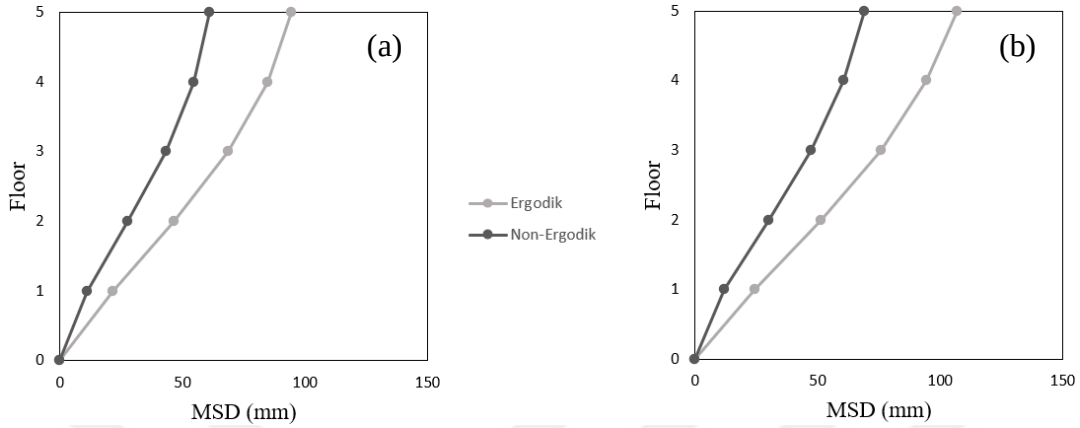

(4) Maximum storey displacements for the 5 storey building model at station site 2307 under strong motion records selected based on nonergodic and ergodic PSHA results based on Kale et al. (2015) study (a) Long. Dir. (b) Trans. Dir.

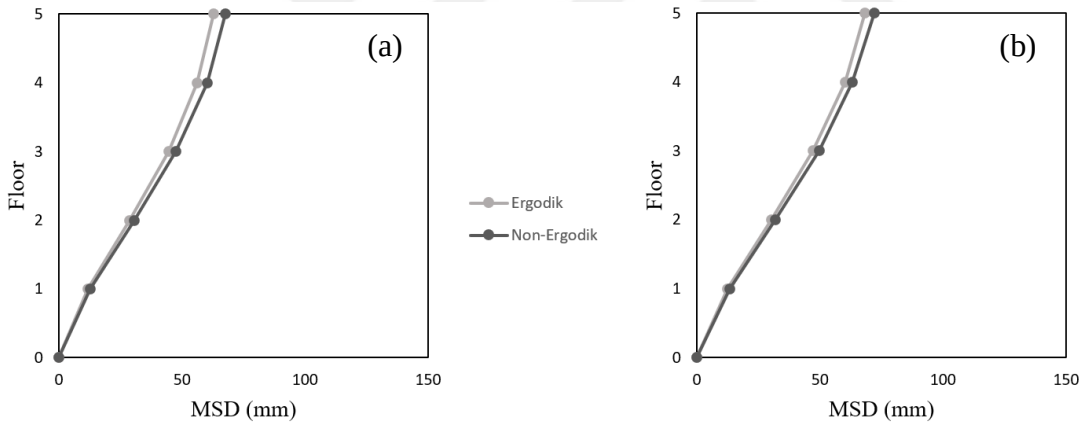

(5) Maximum storey displacements for the 5 storey building model at station site 2301 under strong motion records selected based on nonergodic and ergodic PSHA results based on Kotha et al. (2022) study (a) Long. Dir. (b) Trans. Dir.

Figure 6.1 Maximum storey displacements for the mid-rise building models

In mid-rise buildings, the maximum floor displacements in the transient direction are significantly greater with only a slight difference compared to displacements in the longitudinal direction. This situation is applicable to all cases studied. In the ergodic PSHA Kale et al. (2015) GMPM case, the highest floor displacement occurred in the building at station site 2307, while the lowest floor displacement occurred at station

site 2302. The influence of soil conditions can be observed here. Because the soil classes for station sites 2301, 2302, 2304, and 2307 are ZC, ZB, ZC, and ZD, respectively. However, in the case of the nonergodic PSHA Kale et al. (2015) GMPM case, different observations were made. The maximum floor displacements occurred at station site 2301, while the minimum occurred at station site 2302. At station site 2301 for the mid-rise building model, the Maximum Storey Displacement (MSD) values calculated using the strong motion record set selected based on ergodic PSHA and both Kale et al. (2015) and Kotha et al. (2022) GMPMs are lower than the MSD values calculated based on the counterpart non-ergodic PSHA results. This situation is reversed for the case of Kale et al. (2015) GMPM based PSHA results in the context of other station sites (2302, 2304, 2307). The difference between floor displacements according to the ergodic and non-ergodic methods, for the mid-rise building at station site 2302, is quite small when Kale et al. (2015) GMPM is used. However, it has increased progressively for the buildings at station sites 2301, 2304, and 2307. A similar observation was made for the mid-rise building at station site 2301 when Kotha et al. (2022) GMPM is used. The percentage differences between all floors with respect to ergodic and non-ergodic methods are presented in Table 6.3. The maximum floor displacements at the top floors computed for different cases summarized above are presented in Table 6.4.

Table 6.3 % differences in floor displacement relative to the ergodic and non-ergodic methods

	Kale et al.(2015)		Kale et al.(2015)		Kale et al.(2015)		Kale et al.(2015)		Kotha et al.(2022)	
	2301		2302		2304		2307		2301	
Floor	Long.	Trans.	Long.	Trans.	Long.	Trans.	Long.	Trans.	Long.	Trans.
1	52,6	56,6	20,3	18,5	44,9	44,7	48,9	50,7	9,2	7,9
2	36,5	40,7	18,8	16,2	38,8	38,4	40,5	41,6	6,6	5,8
3	30,5	34,0	18,9	16,5	36,9	36,3	37,0	37,5	6,8	5,1
4	28,1	30,5	19,0	17,0	36,3	35,7	35,9	35,8	7,3	5,2
5	27,0	29,1	18,9	17,3	36,0	35,8	35,6	35,3	7,5	5,5

Table 6.4 Maximum Displacement for the 5th storey

	Station ID	Ergodic PSHA 5th storey MSD (mm) Long. Dir.	Ergodic PSHA 5th storey MSD (mm) Trans. Dir.	Nonergodic PSHA 5th storey MSD (mm) Long. Dir.	Nonergodic PSHA 5th storey MSD (mm) Trans. Dir.
Kale et al. (2015)	2301	65,16	71,62	82,73	92,50
	2302	43,19	46,37	35,02	38,36
	2304	78,15	85,50	49,99	54,91
	2307	94,43	106,84	60,82	69,15
Kotha et al. (2022)	2301	62,82	68,40	67,56	72,16

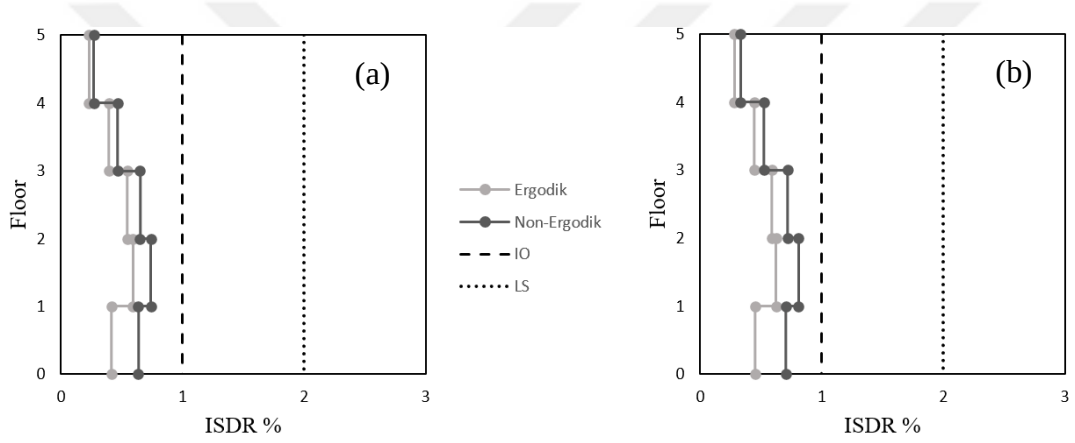

(1) Inter-storey drift ratios for the 5 storey building model at station site 2301 under strong motion records selected based on nonergodic and ergodic PSHA results based on Kale et al. (2015) study (a) Long. Dir. (b) Trans. Dir.

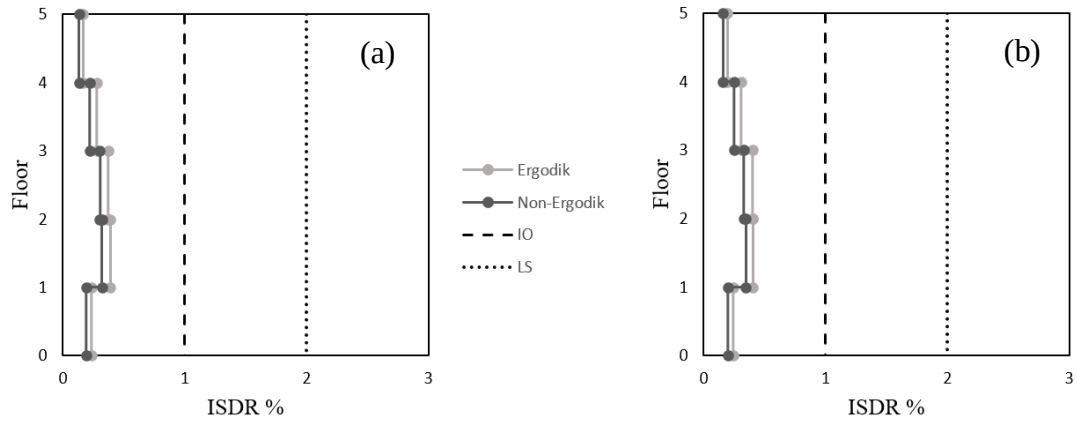

(2) Inter-storey drift ratios for the 5 storey building model at station site 2302 under strong motion records selected based on nonergodic and ergodic PSHA results based on Kale et al. (2015) study (a) Long. Dir. (b) Trans. Dir.

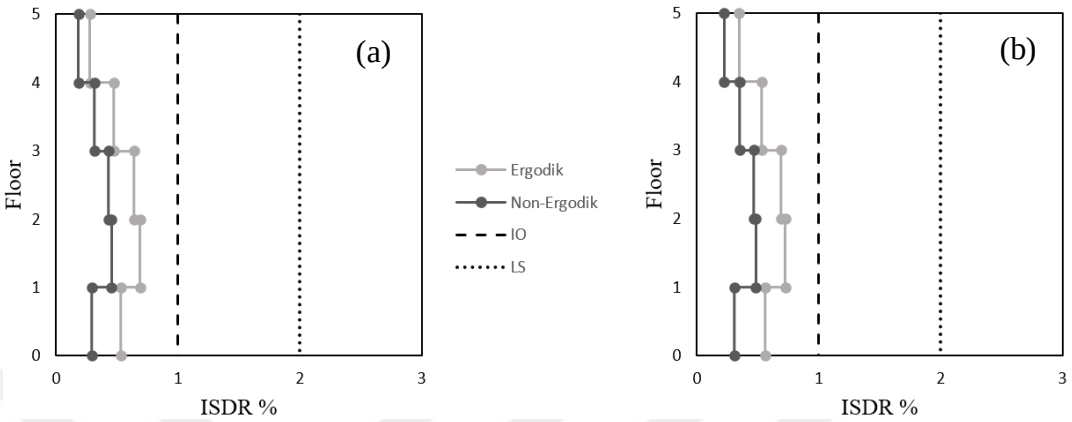

(3) Inter-storey drift ratios for the 5 storey building model at station site 2304 under strong motion records selected based on nonergodic and ergodic PSHA results based on Kale et al. (2015) study (a) Long. Dir. (b) Trans. Dir.

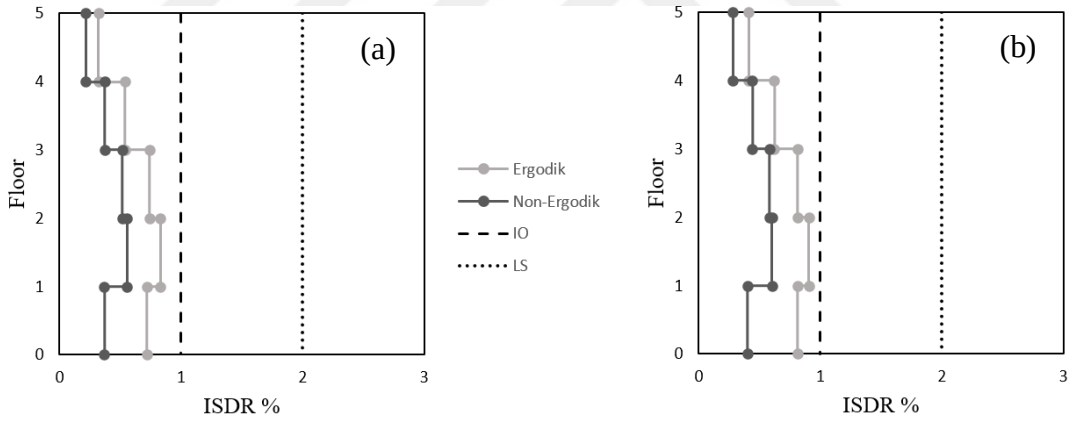

(4) Inter-storey drift ratios for the 5 storey building model at station site 2307 under strong motion records selected based on nonergodic and ergodic PSHA results based on Kale et al. (2015) study (a) Long. Dir. (b) Trans. Dir.

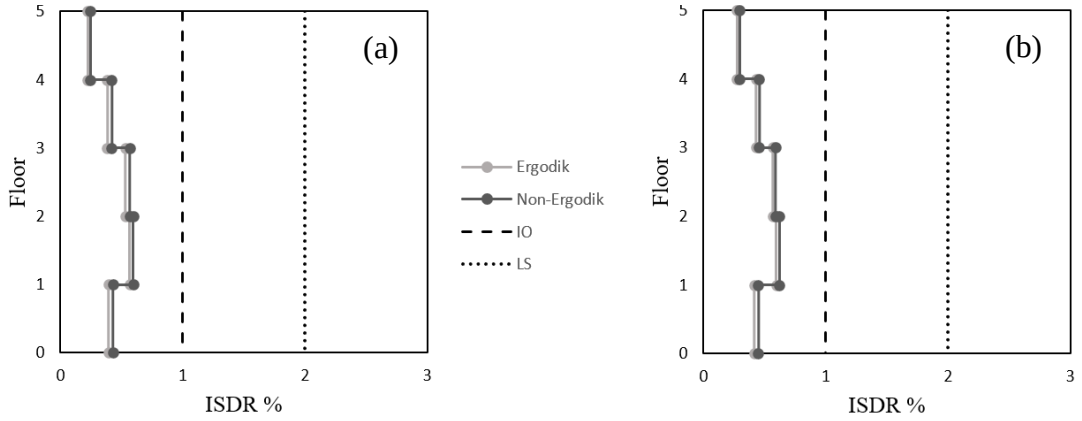

(5) Inter-storey drift ratios for the 5 storey building model at station site 2301 under strong motion records selected based on nonergodic and ergodic PSHA results based on Kotha et al. (2022) study (a) Long. Dir. (b) Trans. Dir.

Figure 6.2 Inter-storey Drift Ratio (ISDR) for the Mid-Rise building models (The acceptance criteria for inter-story drift have been adopted in accordance with ATC-40 (Applied Technology Council)).

The ISDR value is obtained by dividing the relative storey displacements by the storey height. In all methods and buildings, high ISDR values are observed on the first floors, while the ISDR values on the second floors are the highest. The highest ISDR values are provided in Table 6.5. The evaluations previously conducted for MSD based on both methods and stations are also applicable to ISDR (Inter-story Drift Ratio) values.

Table 6.5 Maximum Inter Story Drift Ratio (2nd Storey ISDR)

		Ergodic PSHA Max. ISDR (%)		Nonergodic PSHA Max. ISDR (%)	
	Station ID	Long. Dir.	Trans. Dir.	Long. Dir.	Trans. Dir.
Kale et al. (2015)	2301	0,59	0,62	0,74	0,81
	2302	0,39	0,40	0,32	0,34
	2304	0,69	0,73	0,45	0,48
	2307	0,83	0,91	0,55	0,60
Kotha et al. (2022)	2301	0,57	0,59	0,59	0,62

As a result of the NLTH analyses, the highest level of nonlinear behaviour was observed in the beams of the 1st and 2nd floors, while the most significant damage to the columns was observed on the 1st floor. The plastic rotation values of beam and column edge hinges are provided in Figure 6.2 and Figure 6.3, respectively. Furthermore, the ratio of the horizontal forces acting on the building base to the building weight is presented in Table 6.6. The building weight was calculated according to equation 6.1.

$$W = G + 0{,}3Q \tag{6.1}$$

In this equation, W, represents the building weight, G represents dead loads and Q represents live loads.

Table 6.6 Base Shear/ Weight ratios for Mid-Rise Building Models

		Ergodic PSHA Base Shear/ Weight		Nonergodic PSHA Base shear/ Weight	
	Station ID	Long. Dir.	Trans. Dir.	Long. Dir.	Trans. Dir.
Kale et al. (2015)	2301	0,41	0,40	0,49	0,48
	2302	0,30	0,28	0,26	0,25
	2304	0,46	0,45	0,34	0,33
	2307	0,51	0,50	0,40	0,39
Kotha et al. (2022)	2301	0,40	0,38	0,41	0,40

The most significant damage in the 1st storey reinforcement columns was observed as a result of the analyses conducted in the scope of ergodic PSHA, specifically when utilizing Kale et al. (2015) GMPM for station sites 2304, 2307, and in the scope of non-ergodic PSHA when utilizing Kale et al. (2015) GMPM for station site 2301. This situation corresponds with the data presented in Table 6.5 regarding the base shear/weight ratios.

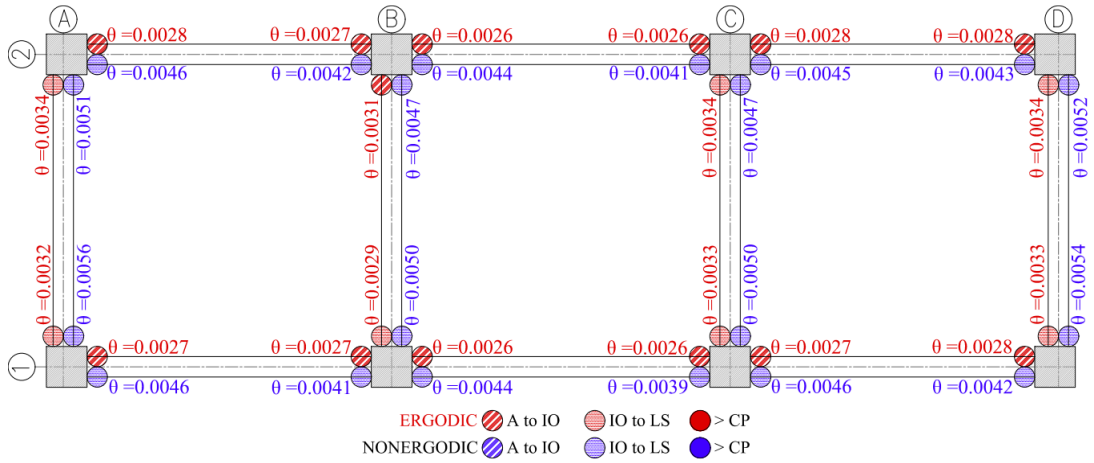

(1) Plastic hinge rotations for the 5 storey building model at station site 2301 under strong motion records selected based on nonergodic and ergodic PSHA results utilizing Kale et al. (2015) GMPM (The small circles represent hinges) While the beams along the long direction of the building remain at the A-IO level, these beams are at the IO-LS level in the non-ergodic PSHA case. As for the beams in the short direction, except for one, they are at the IO-LS level in both cases.

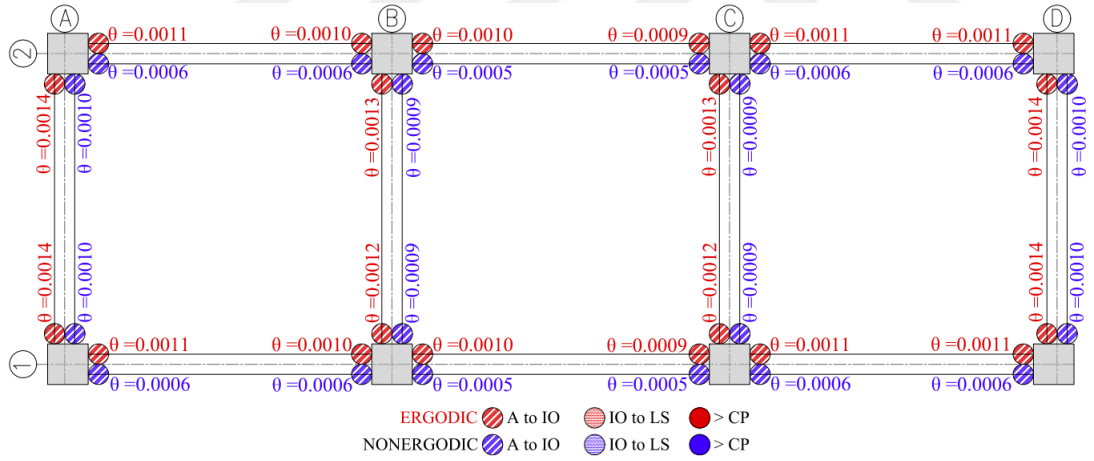

(2) Plastic hinge rotations for the 5 storey building model at station site 2302 under strong motion records selected based on nonergodic and ergodic PSHA results utilizing Kale et al. (2015) GMPM (The small circles represent hinges) In both methods, nearly an equal degree of plastic rotation has occurred in the beams along the long and short directions of the building. All beams are at the A-IO level.

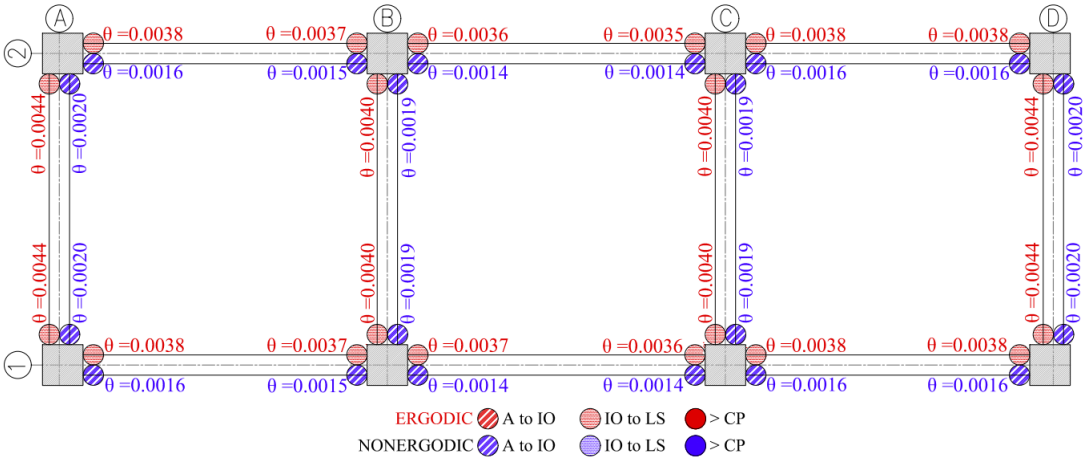

(3) Plastic hinge rotations for the 5 storey building model at station site 2304 under strong motion records selected based on nonergodic and ergodic PSHA results utilizing Kale et al. (2015) GMPM (The small circles represent hinges) In the ergodic PSHA case, the beams along the long and transverse directions of the building have generated a greater degree of plastic rotation compared to the non-ergodic PSHA case. In the ergodic PSHA case, all beams are at the IO-LS level, whereas in the non-ergodic PSHA case, they are at the A-IO level.

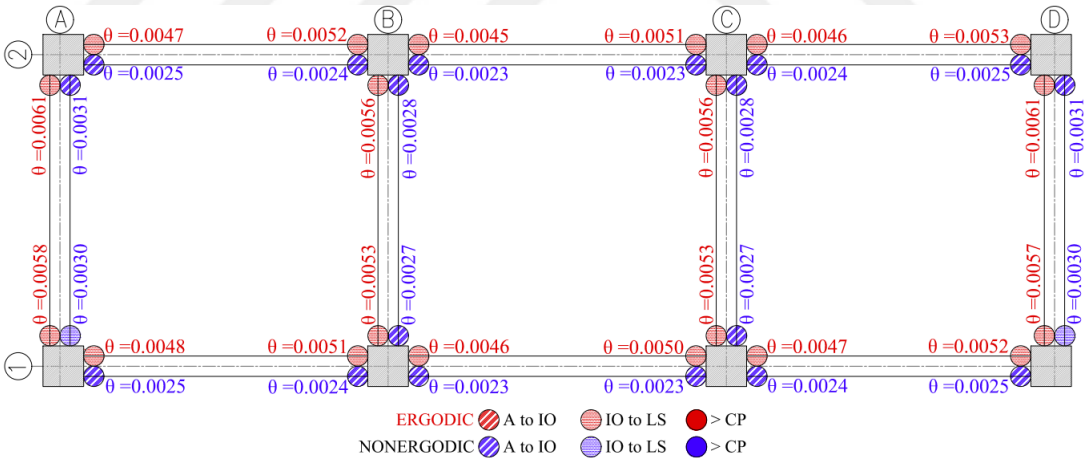

(4) Plastic hinge rotations for the 5 storey building model at station site 2307 under strong motion records selected based on nonergodic and ergodic PSHA results utilizing Kale et al. (2015) GMPM (The small circles represent hinges) Similar to the situation at station site 2304, the beams along the longitudinal and transverse directions of the building have produced a greater degree of plastic rotation compared to the non-ergodic PSHA case. In the ergodic PSHA case, all beams are

at the IO-LS level, whereas in the non-ergodic PSHA case, two of the hinges are at the IO-LS level, while the rest are at the A-IO level.

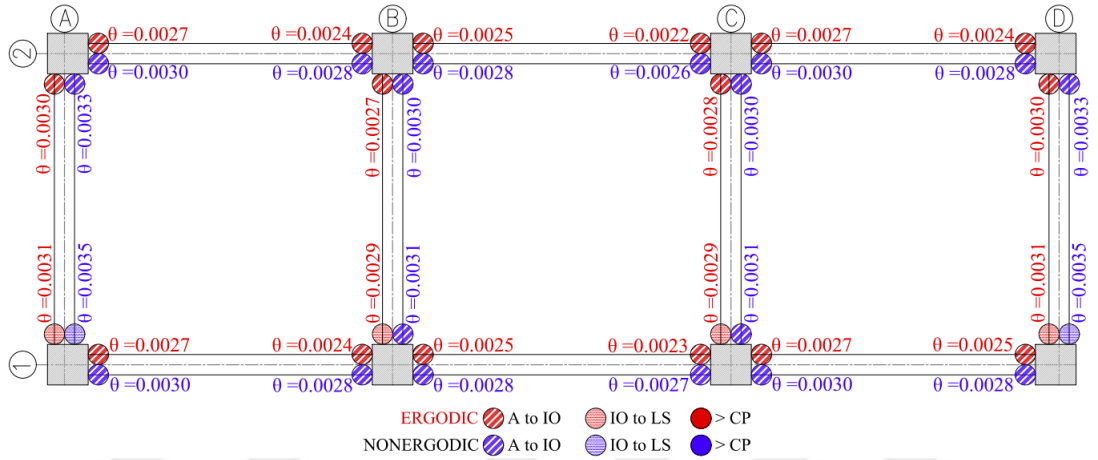

(5) Plastic hinge rotations for the 5 storey building model at station site 2301 under strong motion records selected based on nonergodic and ergodic PSHA results utilizing Kotha et al. (2022) GMPM (The small circles represent hinges) In both ergodic and non-ergodic PSHA cases, there are not significant differences observed in terms of beam plastic rotations . In general, all beams are at the A-IO level. For both cases, at one end of the external beams in the transverse direction, the hinges are at the IO-LS level, whereas for the internal beams in the transverse direction, the hinges are at the IO-LS level in the ergodic PSHA case and at the A-IO level in the non-ergodic PSHA case.

Figure 6.3 1st Floor Plastic Rotations (Radians) of Hinges for Mid-Rise Building Models

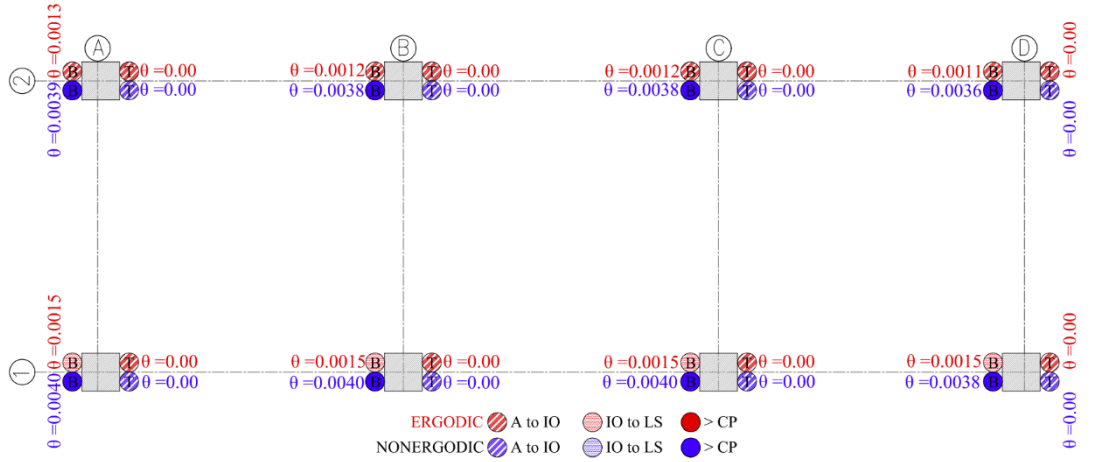

(1) Plastic hinge rotations for the 5 storey building model at station site 2301 under strong motion records selected based on nonergodic and ergodic PSHA results utilizing Kale et al. (2015) GMPM (The small circles represent hinges, B:Bottom Hinge, T:Top Hinge) In the ergodic PSHA case, four columns are at the A-IO level, while the other four columns are at the IO-LS level. However, in the non-ergodic PSHA case, all columns are at the >CP level.

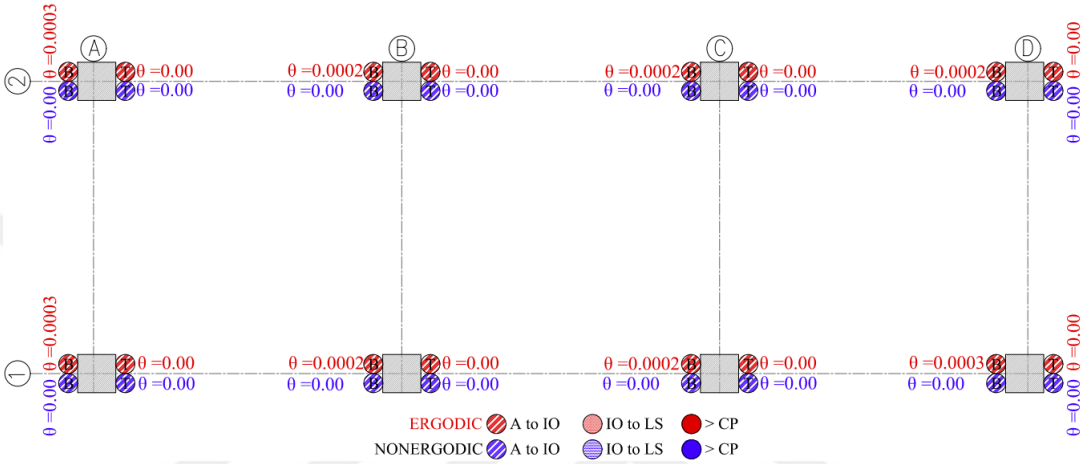

(2) Plastic hinge rotations for the 5 storey building model at station site 2302 under strong motion records selected based on nonergodic and ergodic PSHA results utilizing Kale et al. (2015) GMPM (The small circles represent hinges, B:Bottom Hinge, T:Top Hinge) According to both the ergodic and non-ergodic PSHA cases analyses, all columns are at the A-IO level.

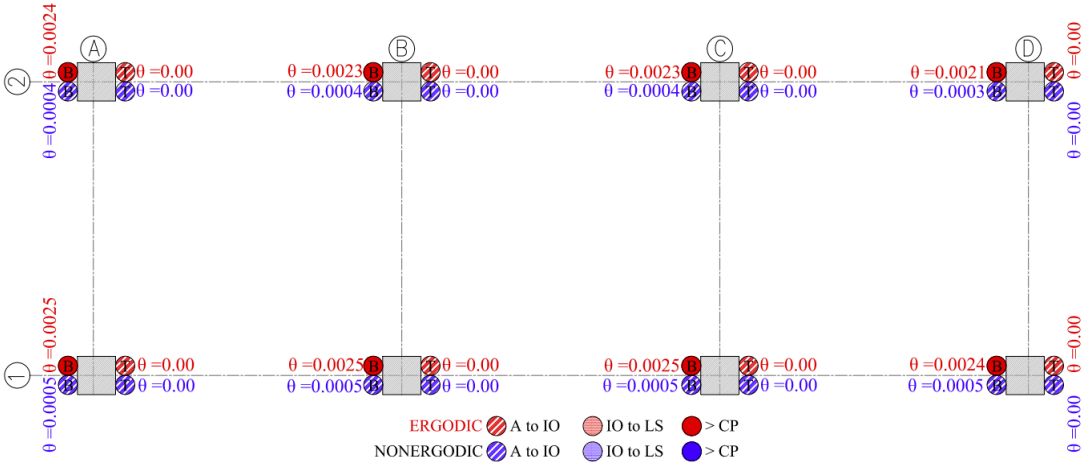

(3) Plastic hinge rotations for the 5 storey building model at station site 2304 under strong motion records selected based on nonergodic and ergodic PSHA results utilizing Kale et al. (2015) GMPM (The small circles represent hinges, B:Bottom

Hinge, T:Top Hinge) While all columns are at the >CP level in the ergodic PSHA case, in the non-ergodic PSHA case, they are at the A-IO level.

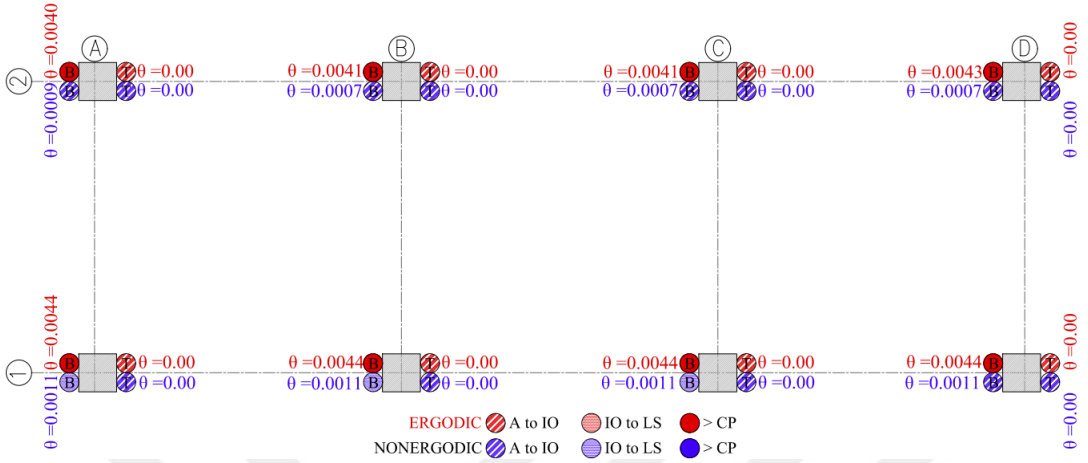

(4) Plastic hinge rotations for the 5 storey building model at station site 2307 under strong motion records selected based on nonergodic and ergodic PSHA results utilizing Kale et al. (2015) GMPM (The small circles represent hinges, B:Bottom Hinge, T:Top Hinge) For the ergodic PSHA case, all columns are at the >CP level. However, as a result of the non-ergodic PSHA case, it was observed that five columns are at the A-IO level, while three columns are at the IO-LS level.

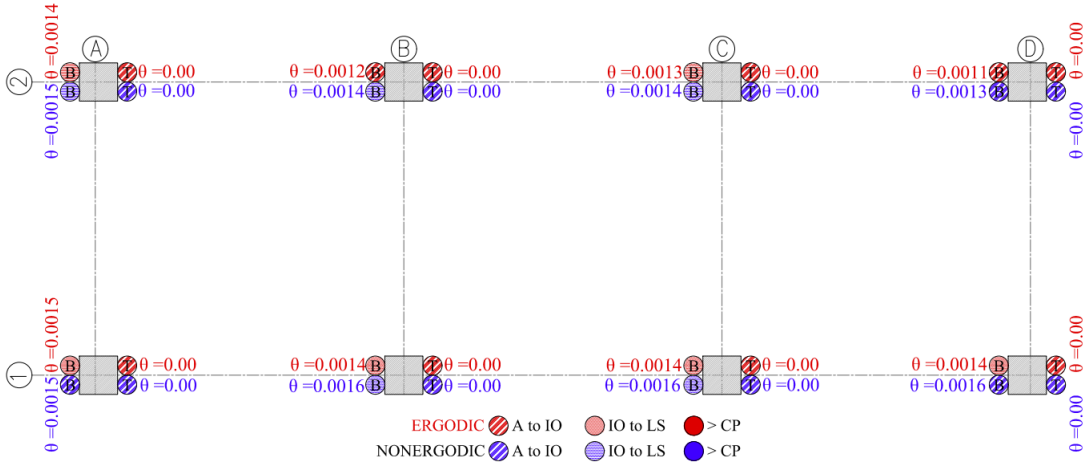

(5) Plastic hinge rotations for the 5 storey building model at station site 2301 under strong motion records selected based on nonergodic and ergodic PSHA results utilizing Kotha et al. (2022) GMPM (The small circles represent hinges) No significant difference in nonlinear behavior was observed in both PSHA cases. In the ergodic PSHA case, two columns are at the A-IO level, while six columns are at

the IO-LS level. In the non-ergodic PSHA case, this situation has changed, with three columns at the A-IO level and five columns at the IO-LS level.

Figure 6.4 1st Floor Plastic Rotations (Radians) of Hinges for Mid-Rise Building Models

When examining the values of ISDR, it is observed that the highest value is attained on the 2nd floors (Table 6.5). Examining the beams and columns on these levels, it is observed that the beams sustain more damage than the first floor beams, and that the columns do not exhibit plastic rotation. The plastic rotation figures for the columns and beams of the relevant floor are provided in Appendix C. Upon examining the 3rd, 4th, and 5th floors, it is observed that the damage condition of reinforced concrete elements decreases progressively as one ascends, with no damage observed in the structural elements on the 4th and 5th floors.

High values of MSD and ISDR were not observed in low-rise buildings. Due to the low-rise nature of the structure, a substantial difference in altering the damage condition of a building related to displacements has not been observed between ergodic and non-ergodic PSHA cases. According to the ergodic and non-ergodic PSHA cases by utilizing Kale et al. (2015) and Kotha et al. (2022) GMPMs, all structural elements and buildings are below the IO level at all station sites. For these reasons, the results, graphics, and figures of low-rise buildings have not been presented in this chapter. All results and graphics are provided in Appendix A.

Within the scope of this section, a comparative analysis of building performance has also been conducted based on different regulations, such as ASCE41-17, ATC40, TBEC18, in accordance with their performance limits. Before making comparisons, it is necessary to discuss the methods of obtaining the plastic rotation values of the regulations. According to TBEC18, regardless of the column-beam distinction, axial loads on sections create significant differences when calculating plastic rotation values. Furthermore, the geometric characteristics of the reinforced concrete element play a significant role in the calculation, along with the content of the reinforcement. However, according to ASCE SEI 41-17, when calculating the plastic rotation values of beams, the design shear force acting on the beam is considered instead of axial load. The beam's geometric properties, reinforcement content, material properties

etc. are taken into account in the calculation. In the case of column plastic rotation values, the design axial load, design shear force, and design moment, as well as transverse reinforcement, are all taken into account, along with the geometric and material properties of the column. According to ATC 40, while the calculation of beam plastic rotation values exhibits similarities with ASCE SEI 41-17, the determination of column plastic rotation values involves considerations such as axial load, shear force, section properties, material properties etc. Table 6.7 provides acceptance criteria calculated in accordance with the regulations for the maximum moments, shear forces, and axial loads acting on the column and beam, based on the results of nonlinear analysis. In fact, these criteria vary for each structural element. However, for the purpose of comparison, the values have been calculated based on the worst-case scenario.

Table 6.7 Acceptance criteria based on plastic rotation values calculated according to different regulations for structural elements.

		IO	LS	CP
TBEC18	COLUMN	0	0,017	0,022
	BEAM	0	0,008	0,011
ASCE SEI 41-17	COLUMN	0,004	0,014	0,019
	BEAM	0,005	0,015	0,020
ATC 40	COLUMN	0,004	0,008	0,018
	BEAM	0,005	0,009	0,019

While TBEC18 does not accept plastic rotation values for the immediate occupancy (IO) level, both ASCE SEI 41-17 and ATC 40 regulations acknowledge a specified limit for such values. For this level, the TBEC18 regulation remains highly conservative. Similarly, when looked at in a general sense for beams, the TBEC18 regulation remains highly conservative. When examining columns, TBEC18 and ASCE SEI 41-17 regulations exhibit similarities, while the ATC 40 regulation remains on the safer side for the life safety (LS) level.

A comprehensive assessment of the hinge condition of the beams and columns on the first floor of the mid-rise buildings under investigation is necessary. For this purpose, the criteria specified in Section 15.8.3 of TBEC18 have been chosen as a

reference. Utilizing the values derived from the acceptance criteria for structural elements specified in the regulations, the overall performance objectives of buildings were determined according to the criteria outlined in TBEC 15.8.3. The building performances are presented in Table 6.8.

Table 6.8 According to the regulations, the performances of the buildings.

	TBEC18	**ASCE SEI 41-17**	**ATC 40**
2301 Kale et al. (2015) Ergodik	IO-LS	<IO	<IO
2301 Kale et al. (2015) Non-Ergodik	IO-LS	IO-LS	IO-LS
2302 Kale et al. (2015) Ergodik	IO-LS	<IO	<IO
2302 Kale et al. (2015) Non-Ergodik	IO-LS	<IO	<IO
2304 Kale et al. (2015) Ergodik	IO-LS	IO-LS	IO-LS
2304 Kale et al. (2015) Non-Ergodik	IO-LS	<IO	<IO
2307 Kale et al. (2015) Ergodik	IO-LS	IO-LS	IO-LS
2307 Kale et al. (2015) Non-Ergodik	IO-LS	<IO	<IO
2301 Kotha et al. (2022) Ergodik	IO-LS	<IO	<IO
2301 Kotha et al. (2022) Non-Ergodik	IO-LS	<IO	<IO

Table 6.8 shows that, in terms of building performance analysis, ASCE SEI 41-17 and ATC 40 produce conclusions that are similar, however TBEC18 takes a more conservative approach.

CHAPTER 7

CONCLUSIONS

7.1 Non-ergodic Ground Motion Prediction Models

- Kale et al. (2015), Kotha et al. (2016), Kotha et al. (2020) and Kotha et al. (2022) non-ergodic GMPMs developed for Turkey were compared. Kale et al. (2015) and Kotha et al. (2016) predictions are close. Kale et al. (2015) and Kotha et al. (2022) predictions for the East Anatolian Fault Zone are close for the 10 km-100 km range and PGA and short period PSA but deviates from one another for the long period PSA. For the long period PSA, Kotha et al. (2022) estimates are higher.
- For $R_{JB} < 5$ km and $M_w \geq 6.0$ in the case of Kotha et al. (2020) and Kotha et al. (2022) GMPMs a persistent magnitude saturation problem exists.
- Kotha et al. (2016), Kotha et al. (2020) and Kotha et al. (2022) GMPMs do not model soil nonlinearity. As a result, predictions of these models deviate from those of Kale et al. (2015) GMPM and recorded strong-motion data of the 2023 Kahramanmaraş Earthquake sequence at NEHRP D type sites.
- Recorded response spectra of 2023 Kahramanmaraş Earthquake aftershocks were compared with the computed Kotha et al. (2022) based response spectra within the scope of this study. For NEHRP C type sites, observed spectra matched well the source corrected computed spectra. However, number of records based on which the site term δS2S is computed observed to be an important parameter for the degree of agreement between the observed spectra and computed source and site corrected spectra.
- The non-ergodic sigma values computed for the Kale et al. (2015) GMPM within the scope of the Cagnan and Akkar (2019) study are lower than corresponding sigma values computed for the Kotha et al. (2022) GMPM for the period range of 0.01s-0.4s. Beyond 0.4s however non-ergodic sigma

values computed for the Kale et al. (2015) GMPM exceed the non-ergodic sigma values computed for the Kotha et al. (2022) GMPM.

- The source term δL2L computed for the Kale et al. (2015) GMPM for the East Anatolian Fault source is not a function of magnitude. The computed δL2L term is negligible suggesting that the general Kale et al. (2015) source model is applicable for the East Anatolian Fault Zone as well. This is contradictory to the source term computed for the North Anatolian Fault Zone within the scope of Cagnan and Akkar (2019) study.
- The source term δL2L computed for the Kale et al. (2015) GMPM for the East Anatolian Fault source should be recalculated with the 2023 Kahramanmaraş Earthquake sequence data. Deficiency of M_w6.5> data is expected to be the reason for the observed magnitude independency of the developed δL2L model.

As mentioned above, the δL2L value calculated specifically for the Eastern Anatolian fault is on average in Turkey, unlike the Marmara region. In light of the earthquake data in Kahramanmaraş, the δL2L value should be reevaluated. It is evident from here that obtaining more data leads to more accurate results. This situation motivates research in different earthquake regions in Turkey and around the world. It is crucial to investigate the potential effects of a earthquake in regions with high population and financial density, particularly in Turkey, such as the Marmara region, through future studies.

7.2 Hazard

- Within the scope of this study, 475 years return period and 2475 years return period uniform hazard spectra were computed for the station sites 2301, 2302, 2304, 2307 of AFAD by utilizing the ergodic Kale et al. (2015) and Kotha et al. (2022) GMPMs together with measured or inferred V_{S30} values for the station sites. Computed uniform hazard spectra were observed to be consistently lower than the design elastic acceleration spectra suggested by TBEC2018 for these sites. This shows the influence of taking into account

ground motion epistemic uncertainty in hazard assessment studies (i.e., a ground motion logic tree was developed to represent ground motion epistemic uncertainty when developing the 2014 seismic hazard map of Turkey).

- For the station site 2301, 475 years return period uniform hazard spectrum computed by utilizing the ergodic Kale et al. (2015) GMPM exceeds its counterpart computed by utilizing the ergodic Kotha et al. (2022) GMPM in the period range 0.2s-3.0s up to 15%.
- For the station site 2302, 475 years return period uniform hazard spectrum computed by utilizing the ergodic Kale et al. (2015) GMPM exceeds its counterpart computed by utilizing the ergodic Kotha et al. (2022) GMPM in the period range 1.0s-2.2s up to 10%.
- For the station site 2304, 475 years return period uniform hazard spectrum computed by utilizing the ergodic Kale et al. (2015) GMPM exceeds its counterpart computed by utilizing the ergodic Kotha et al. (2022) GMPM in the period range 0.7s-2.4s up to 10%.
- For the station site 2307, 475 years return period uniform hazard spectrum computed by utilizing the ergodic Kale et al. (2015) GMPM exceeds its counterpart computed by utilizing the ergodic Kotha et al. (2022) GMPM in the period range 0.2s-0.4s up to 10%.
- For the station site 2301, 2475 years return period uniform hazard spectrum computed by utilizing the ergodic Kale et al. (2015) GMPM exceeds its counterpart computed by utilizing the ergodic Kotha et al. (2022) GMPM in the period range 0.2s-2.5s up to 12%.
- For the station site 2302, 2475 years return period uniform hazard spectrum computed by utilizing the ergodic Kale et al. (2015) GMPM exceeds its counterpart computed by utilizing the ergodic Kotha et al. (2022) GMPM in the period range 1.0s-2.5s up to 10%.
- For the station site 2304, 2475 years return period uniform hazard spectrum computed by utilizing the ergodic Kale et al. (2015) GMPM exceeds its

counterpart computed by utilizing the ergodic Kotha et al. (2022) GMPM in the period range 0.15s-2.5s up to 15%.

- For the station site 2307, 2475 years return period uniform hazard spectrum computed by utilizing the ergodic Kale et al. (2015) GMPM exceeds its counterpart computed by utilizing the ergodic Kotha et al. (2022) GMPM in the period range 0.15s-0.3s up to 10%.
- Non-ergodic Kale et al. (2015) GMPM source and site terms were computed by following the Rodriguez-Marek et al. (2013) approach whereas Non-ergodic Kotha et al. (2022) GMPM source and site terms were computed by following NLME approach first pointed out by Stafford (2014). In the period range of 0.01s-2.8s, difference between the non-ergodic Kale et al. (2015) based uniform hazard spectrum developed for the station site 2301 for the 2475 years return period and the non-ergodic Kotha et al. (2022) based uniform hazard spectrum is up to 25%. This illustrates computationally less elaborate Rodriguez-Marek et al. (2013) approach can be used as a first approximation to conduct site and source specific seismic hazard assessment for sites of special interest.
- Although non-ergodic GMPMs have lower sigma in comparison to ergodic GMPMs, this does not always show itself as a reduction in hazard estimates. For station sites 2304 and 2307, non-ergodic uniform hazard spectra are lower than their ergodic counterparts but for station site 2301, non-ergodic uniform hazard spectrum exceeds its ergodic counterpart in the intermediate to long period range.

Based on the data obtained as discussed above, significant variations are observed in both ergodic and non-ergodic uniform hazard spectra from region to region. Therefore, in the future, with the data to be obtained from the field and advancements in technology on a daily basis, more precise regional uniform hazard spectrum calculations can be conducted throughout Turkey.

7.3 Dynamic Behaviour of Low-rise and Mid-rise Residential Buildings

- Within the scope of this work, a single record selection approach was utilized hence influence of record selection on observed dynamic behaviour of studied structures was ignored. This is a limitation of this study.
- Utilizing non-ergodic uniform hazard spectra only observed to influence the dynamic behaviour of mid-rise residential buildings studied within the scope of this thesis. In the case of selected sites, dynamic behaviour of low-rise residential building models was observed to be immune for differences arising from ergodic vs. non-ergodic hazard assessments.
- ATC40, TBEC2018, ASCE 41-17 based performance assessment approaches yielded consistent results, TBEC2018 always yielding comparatively conservative results. Depending on the site characteristics and the dominant period of the structure under investigation, detected performance level of the structure under investigation shifted one level up or dropped one level down as a result of utilizing non-ergodic uniform hazard spectra. For the station site 2301, computed performance level shifted one level up. For the station sites 2304 and 2307, computed performance level shifted one level down.
- In the case of investigated sites and structure types, the difference detected in the performance level by carrying out non-ergodic seismic hazard assessment instead of ergodic seismic hazard assessment may not be observed depending on the adopted performance assessment approach. ASCE 41-17 and ATC40 performance assessment approaches are more sensitive in comparison to TBEC2018 approach to changes in uniform hazard spectra.
- Column and beam plastic rotation values as well as maximum floor displacements were observed to be the two parameters that are the most sensitive to differences in the uniform hazard spectra because of utilizing non-ergodic hazard assessment instead of ergodic hazard assessment. ISDR and base shear were observed to be less sensitive. Detected differences between ergodic vs. non-ergodic hazard assessment based ISDR values and base shear values were observed to be the same, around 20%.

Within the scope of this study, the effects of ergodic and non-ergodic earthquake calculations were investigated on 5-story and single-story structures. It is observed that single-story structures are not affected by these different seismic calculations, while differences in performance levels are observed in multi-story structures. The examination of this situation in more detail, especially in more critical engineering structures such as nuclear power plants, dams, gas pipelines, etc., could be the subject of future studies.

REFERENCES

Abrahamson, N.A., Hollenback, J.C. (2012). Application of Single-Station Sigma Ground Motion Prediction Equations in Practice. *15 WCEE*, Lisboa

Abrahamson, N.A., Kuehn, N.M., Walling, M., Landwehr, N. (2019). Probabilistic Seismic Hazard Analysis in California Using Nonergodic Ground-Motion Models. *Bulletin of the Seismological Society of America*, Vol. 109, No. 4, pp. 1235–1249

Abrahamson, N.A., Youngs, R.R. (1992). A Stable Algorithm For Regression Analyses Using the Random Effects Model. *Bulletin of the Seismological Society of America*, Vol. 82, No. 1, pp. 505-510

Akkar, S., Sandıkkaya, M.A., Bommer, J.J. (2013). Empirical Ground-Motion Models for Point- and Extended-Source Crustal Earthquake Scenarios in Europe and the Middle East. *Bull Earthquake Eng*

Al Atik, L., Abrahamson, N. Bommer, J.J., Scherbaum,F., Cotton, F., Kuehn, N. (2010). The Variability of Ground-Motion Prediction Models and Its Components. *Seismological Research Letters*, Vol. 81, No. 5, pp.794-801

American Society of Civil Engineers (41-17), Structural Engineering Institute. *Seismic Evaluation and Retrofit of Existing Buildings*

Anderson, J.G., Brune, J.N. (1999). Probabilistic Seismic Hazard Analysis without the Ergodic Assumption. *Seismological Research Letters*, Vol. 70, No. 1, pp. 19-28

Applied Technology Council. (1996). *ATC-40 Seismic Evaluation and Retrofit of Concrete Buildings Volume 1*. California , USA

Atkinson, G.M. (2006). Single-Station Sigma. *Bulletin of the Seismological Society of America*, Vol. 96, No. 2, pp. 446–455

Beyer, K., Bommer, J.J. (2006). Relationships between Median Values and between Aleatory Variabilities for Different Definitions of the Horizontal Component of Motion. *Bulletin of the Seismological Society of America*, Vol. 96, No. 4A, pp. 1512–1522

Bindi, D., Massa, M., Luzi, L., Ameri, G. Pacor, F. Puglia, R., Augliera, P. (2014). Pan-European Ground-Motion Prediction Equations for the Average Horizontal Component of PGA, PGV, and 5 %-Damped PSA at Spectral Periods up to 3.0 s Using the RESORCE Dataset. *Bull Earthquake Eng*, Vol.12, pp.391–430

Bommer, J.J., Coppersmith, K.J., Coppersmith,R.T., Hanson, K.H., Mangongolo,A., Neveling, J., Rathje,E.M., Rodriguez-Marek, A., Scherbaum, F. Shelembe, R., Stafford, P.J., Strasser, F.O. (2015). A SSHAC Level 3 Probabilistic Seismic Hazard

Analysis for a New-Build Nuclear Site in South Africa. *Earthquake Spectra,* Vol. 31, No. 2, pp. 661–698

Brillinger, D.R., Preisler, H.K.(1985). Further Analysis of the Joyner-Boore Attenuatıon Data. *Bulletin of the Seismological Society of America*, Vol. 75, No. 2, pp. 611-614

Campbell, K.W., Bozorgnia, Y. (2003). Updated Near-Source Ground-Motion (Attenuation) Relations for the Horizontal and Vertical Components of Peak Ground Acceleration and Acceleration Response Spectra. *Bulletin of the Seismological Society of America*, Vol. 93, No. 1, pp. 314–331

Campell, K.W., Bozorgnia, Y., Kuehn, N., Gregor, N. (2022). An Evaluation of Partially Nonergodic PGA Ground-Motion Models for Japanese Megathrust Earthquake. *Earthquake Spectra,* Vol. 38, No. 4, pp. 2611–2637

Chen,Y., Tsai,C.P. (2002). A New Method for Estimation of the Attenuation Relationship with Variance Components. *Bulletin of the Seismological Society of America*, Vol. 92, No. 5, pp. 1984–1991

Chiou, B.S.J., Youngs, R.R. (2014). Update of the Chiou and Youngs NGA Model for the Average Horizontal Component of Peak Ground Motion and Response Spectra. *Earthquake Spectra,* Vol. 30, No. 3, pp. 1117–1153

Cornell, C.A. (1968). Engineering Seismic Rısk Analysis. *Bulletin of the Seismological Society of America*. Vol. 58, No. 5, pp. 1583-1606

Çağnan,Z., Akkar, S. (2019). Assessment of Aleatory and Epistemic Uncertainty for Ground-Motion Intensity Measure Prediction in Turkey. *Bulletin of the Seismological Society of America*, Vol. 109, No. 1, pp. 263–283

Çağnan,Z. (2020). On How the Ergodic Assumption İnfuences Seismic Risk. *Bulletin of Earthquake Engineering*, Vol. 19, pp.1–25

Danciu, L., Nandan, S., Reyes, C.G., Basili, R., Weatherill, G., Beauval, C., Rovida, A., Vilanova, S., Sesetyan, K., Bard, P., Cotton, F., Wiemer, S., Giardini, D. (2021). *The 2020 update of the European Seismic Hazard Model - ESHM20: Model Overview.* EFEHR Technical Report

Dawood, H.M., Rodriguez-Marek, A. (2013). A Method for Including Path Effects in Ground-Motion Prediction Equations: An Example Using the Mw 9.0 Tohoku Earthquake Aftershocks. *Bulletin of the Seismological Society of America,* Vol. 103, No. 2B, pp. 1360–1372

Kale, Ö., Akkar, S., Ansari, A., Hamzehloo, H. (2015). A Ground-Motion Predictive Model for Iran and Turkey for Horizontal PGA, PGV, and 5% Damped Response

Spectrum: Investigation of Possible Regional Effects. *Bulletin of the Seismological Society of America*, Vol. 105, No. 2A, pp. 963–980

Kohrangi, M., Reddy, K., Bazzurro, P. (2020). Impact of Partially Non-Ergodic Site-Specific Probabilistic Seismic Hazard on Risk Assessment of Single Buildings. *Earthquake Spectra*, Vol. 37, No. 1, pp. 409–427

Kohrangi, M., Kotha, S.R., Bazzurro, P. (2021). Impact of Partially Non-Ergodic Site-Specific Probabilistic Seismic Hazard on Risk Assessment of Single Buildings. *Earthquake Spectra*, Vol. 37, No.1, pp. 409–427

Ktenidou, O.J., Roumelioti, Z., Abrahamson, N., Cotton, F., Pitilakis, K., Hollender, F. (2018). Understanding Single-Station Ground Motion Variability and Uncertainty (Sigma): Lessons Learnt from EUROSEISTEST. *Bull Earthquake Eng*, Vol. 16, pp.2311–2336

Kotha, S.R., Bindi, D., Cotton,F. (2016). Partially Non-Ergodic Region Specific GMPE for Europe and Middle-East. *Bull Earthquake Eng*, Vol.14, pp.1245–1263

Kotha, S.R., Bindi, D., Cotton, F. (2017). From Ergodic to Region- and Site-Specific Probabilistic Seismic Hazard Assessment: Method Development and Application at European and Middle Eastern Sites. *Earthquake Spectra*, Vol. 33, No. 4, pp. 1433–1453

Kotha, S.R., Wetherill, G., Bindi, D., Cotton,F. (2020). A Regionally-Adaptable Ground-Motion Model for Shallow Crustal Earthquakes in Europe. *Bulletin of Earthquake Engineering*, Vol. 18, pp.4091–4125

Kotha, S.R., Weatherill, G., Bindi, D., Cotton, F. (2021). Near-Source Magnitude Scaling of Spectral Accelerations: Analysis and Update of Kotha et al. (2020) Model. *Bulletin of Earthquake Engineering*, Vol. 20, pp.1343–1370

Lanzano, G., Pacor, F., Luzi, L., D'Amico, M., Puglia, R., Felicetta, C. (2017). Systematic Source, Path and Site Effects on Ground Motion Variability: The Case Study of Northern Italy. *Bull Earthquake Eng*, Vol. 15, pp.4563–4583

Lanzano, G., Sgobba, S., Luzi, L., Puglia, R., Pacor, F., Felicetta, C., D'Amico, M., Cotton, F., Bindi, D. (2018). The Pan-European Engineering Strong Motion (ESM) Fatfle: Compilation Criteria and Data Statistics. *Bulletin of Earthquake Engineering*

Lavrentiadis, G., Abrahamson, N.A., Kuehn, N.M. (2021). A Non-Ergodic Efective Amplitude Ground-Motion Model for California. *Bulletin of Earthquake Engineering*,

Lavrentiadis, G., Abrahamson, N.A. (2023). A Non-Ergodic Spectral Acceleration Ground Motion Model for California Developed with Random Vibration Theory. *Bulletin of Earthquake Engineering*

Lin, P., Chiou, B., Abrahamson, N., Walling, M., Lee, C., Cheng, C. (2011). Repeatable Source, Site, and Path Effects on the Standard Deviation for Empirical Ground-Motion Prediction Models. *Bulletin of the Seismological Society of America*, Vol. 101, No. 5, pp. 2281–2295

Luzı, L., Pacor, F., Puglıa, R., Russo, E., D'amıco, M., Felıcetta, C., Lanzano, G., ORFEUS-ESM working group. (2018, June). *The Engineering Strong Motion Database: Web Portal and Webservices for Engineering Seismologists*. 16th European Conference on Earthquake Engineering, Thessaloniki

Macedo, J., Liu, C. (2022). A Nonergodic Ground Motion Model for Chile. *Bulletin of the Seismological Society of America,* Vol. 112, No. 5, pp.2542-2561

Marek, A.R., Montalva, G.A., Cotton, F., Bonilla, F. (2011). Analysis of Single-Station Standard Deviation Using the KiK-net Data. *Bulletin of the Seismological Society of America*, Vol. 101, No. 3, pp. 1242–1258

Marek, A.R., Rathje, E.M., Bommer, J.J., Scherbaum, F., Stafford, P.J. (2014). Application of Single-Station Sigma and Site-Response Characterization in a Probabilistic Seismic-Hazard Analysis for a New Nuclear Site. *Bulletin of the Seismological Society of America*, Vol. 104, No. 4, pp. 1601–1619

Morikawa, N., Kanno, T., Narita, A., Fujiwara, H., Okumura, T., Fukushima, Y., Guerpinar, A. (2008). Strong Motion Uncertainty Determined from Observed Records by Dense Network in Japan. *J Seismol*, Vol. 12, pp.529–546

Önder, F.M. (2022). *Towards The Non-Ergodic Ground Motion Models of Turkey: Assessment of Systematic Site, Source and Path Effects*. (Unpublished master dissertation), The Graduate School of Natural and Applied Sciences of Middle East Technical University

Pagani, M., Silva, V., Rao, A., Simionato, M., Johnson, K. (2023). *OpenQuake Engine Manual Release devel. (3.19.0)*

Paolucci, R., Pacor, F., Puglia, R., Ameri, G., Cauzzi, C., Massa, M. (2011). Record Processing in ITACA, the New Italian Strong-Motion Database

Rasmussen, C.E., Williams, C.K. (2006). Gaussian Processes for Machine Learning. Vol.1, pp.159

Resmi Gazete. (2018). *Türkiye Bina Deprem Yönetmeliği*

Rodriguez-Marek, A., Cotton, F., Abrahamson, N.A., Akkar, S., Al Atik, L., Edwards, B., Montalva, G.A., Dawood, H.M. (2013). A Model for Single-Station Standard DeviationUsing Data from Various Tectonic Regions. *Bulletin of the Seismological Society of America*, Vol. 103, No. 6, pp. 3149–3163

Sgobba, S.A., Felicetta, C., Lanzano, G., Ramadan, F., D'Amico, M.C., Pacor, F. NESS2.0: An Updated Version of the Worldwide Dataset for Calibrating and Adjusting Ground Motion Models in Near-Source, *Bulletin of the Seismological Society of America*

Smirnov, N.V. (1939). Estimate of Deviation between Emprical Distribution Functions in Two Independent Samples. *Bull Moscow University*, 2, 3616

Stafford, P.J. (2014). Crossed and Nested Mixed-Effects Approaches for Enhanced Model Development and Removal of the Ergodic Assumption in Empirical Ground-Motion Models. *Bulletin of the Seismological Society of America*, Vol. 104, No. 2, pp. 702–719

Türk Standartları Enstitüsü. (1997). *Yapı Elemanlarının Boyutlandırılmasında Alınacak Yüklerin Hesap Değerler.* Ankara, Türkiye

Türk Standartları Enstitüsü. (1997). *Yapıların Projelendirilme Esasları-Taşıyıcı Olan ve Olmayan Elemanlar Depolanmış Malzemeler-Yoğunluk*. Ankara, Türkiye

Türk Standartları Enstitüsü. (2000). *Betonarme Yapıların Tasarım ve Yapım Kuralları*. Ankara, Türkiye

Toro, G.R., Abrahamson, N.A., Schneider, J.F. (1997). Model of Strong Ground Motions from Earthquakes in Central and Eastern North America: Best Estimates and Uncertainties. *Seismological Research Letters*, Vol. 68, No. 1, pp.41-57

Villani, M., Abrahamson, N.A. (2015). Repeatable Site and Path Effects on the Ground-Motion Sigma Based on Empirical Data from Southern California and Simulated Waveforms from the CyberShake Platform. *Bulletin of the Seismological Society of America*, Vol. 105, No. 5, pp. 2681–2695

Yunatcı, A.A., Çetin, Ö. (2007, Ekim). *Olasılıksal Sismik Tehlike Analizleriyle Tümleştirilmiş, Sahaya Özel Sismik Tepki Ve Zemin Sıvılaşması Değerlendirmesi*. Altıncı Ulusal Deprem Mühendisliği Konferansı, İstanbul

Zafarani, H., Soghrat, M.R. (2017). Single-Station Sigma for the Iranian Strong Motion Stations. *Pure Appl. Geophys*, Vol. 174, pp.4077–4099

Internet

Interactive Web Application for Earthquake Hazard Maps of Turkey *Retrieved from: https://tdth.afad.gov.tr/TDTH/main.xhtml*

Turkey Acceleration Database and Analysis System *Retrieved from: https://tadas.afad.gov.tr*

Takeda Hysteresis Model *Retrieved from: https://docs.csiamerica.com/help-files/csibridge/Advanced_tab/Assign/Takeda_Hysteresis_Model.htm*

APPENDICES

A. MAXIMUM STORY DRIFT GRAPHICS, INTER-STORY DRIFT RATIO GRAPHICS, PLASTIC ROTATION FIGURES OF LOW-RISE BUILDINGS

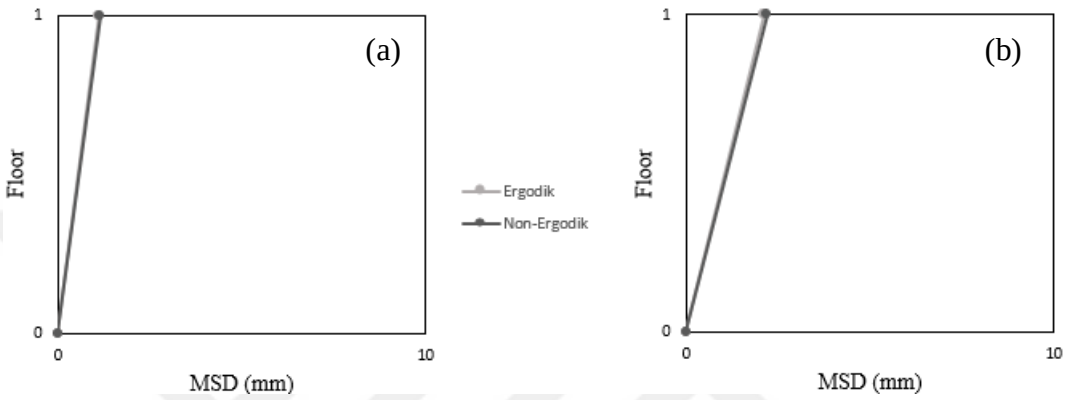

(1) Maximum storey displacements for the 1 storey building model at station site 2301 under strong motion records selected based on nonergodic and ergodic PSHA results based on Kale et al. (2015) study (a) Long. Dir. (b) Trans. Dir.

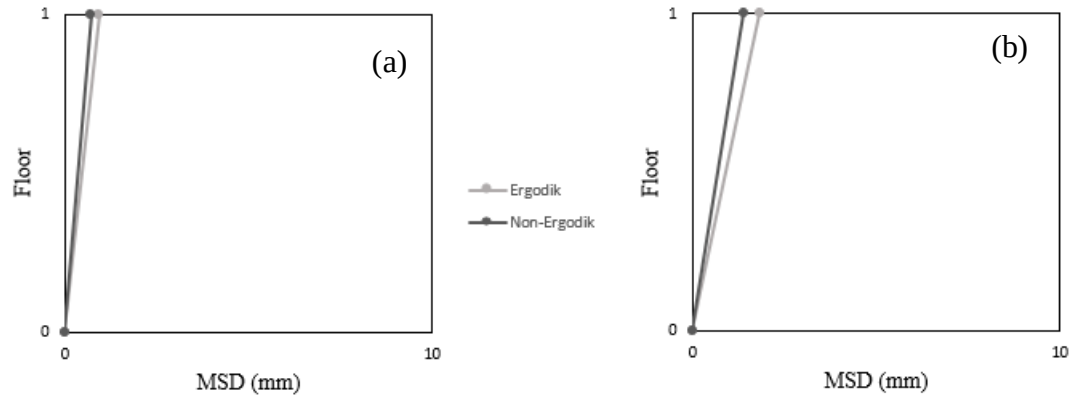

(2) Maximum storey displacements for the 1 storey building model at station site 2302 under strong motion records selected based on nonergodic and ergodic PSHA results based on Kale et al. (2015) study (a) Long. Dir. (b) Trans. Dir.

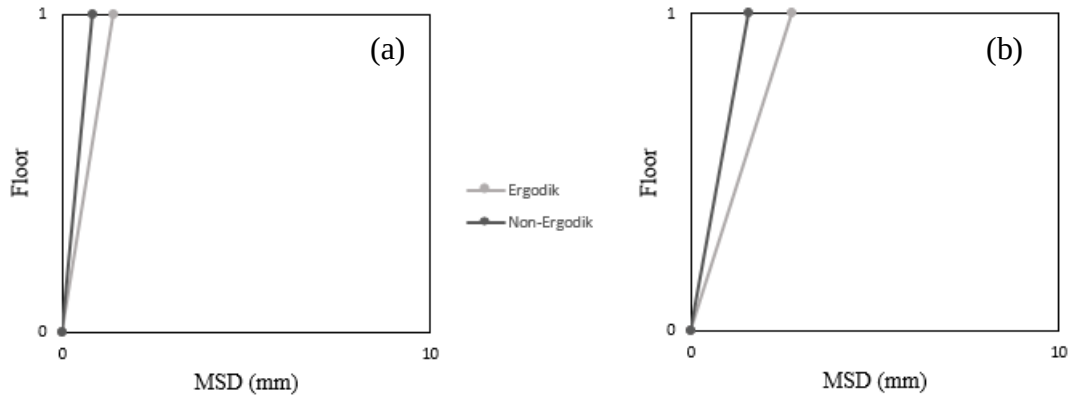

(3) Maximum storey displacements for the 1 storey building model at station site 2304 under strong motion records selected based on nonergodic and ergodic PSHA results based on Kale et al. (2015) study (a) Long. Dir. (b) Trans. Dir.

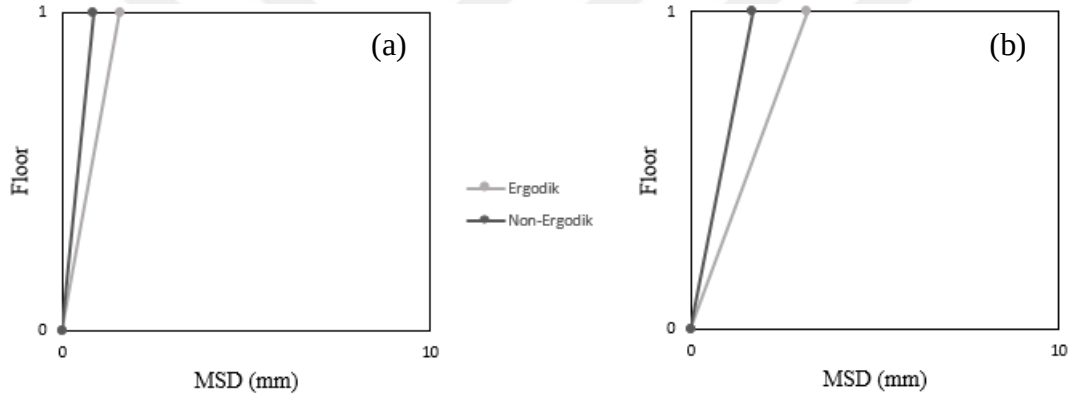

(4) Maximum storey displacements for the 1 storey building model at station site 2304 under strong motion records selected based on nonergodic and ergodic PSHA results based on Kale et al. (2015) study (a) Long. Dir. (b) Trans. Dir.

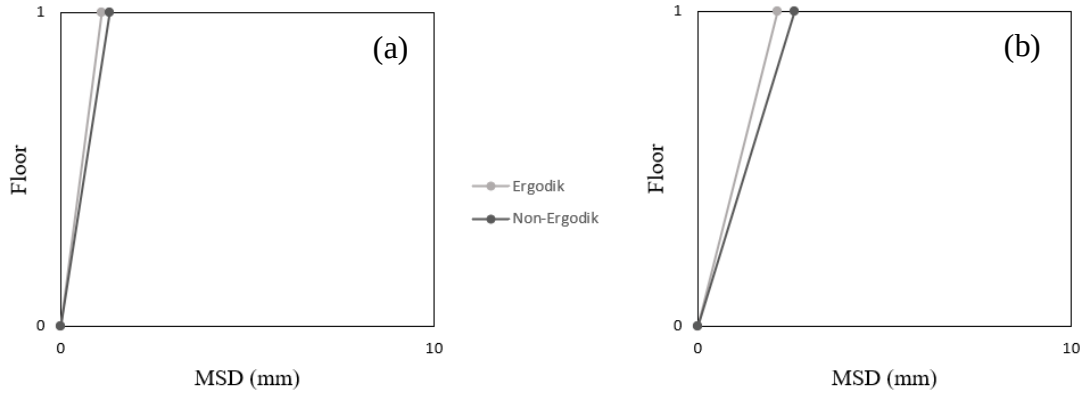

(5) Maximum storey displacements for the 1 storey building model at station site 2301 under strong motion records selected based on nonergodic and ergodic PSHA results based on Kotha et al. (2022) study (a) Long. Dir. (b) Trans. Dir.

Figure A.1 Maximum storey displacements for the Low-Rise Building Models

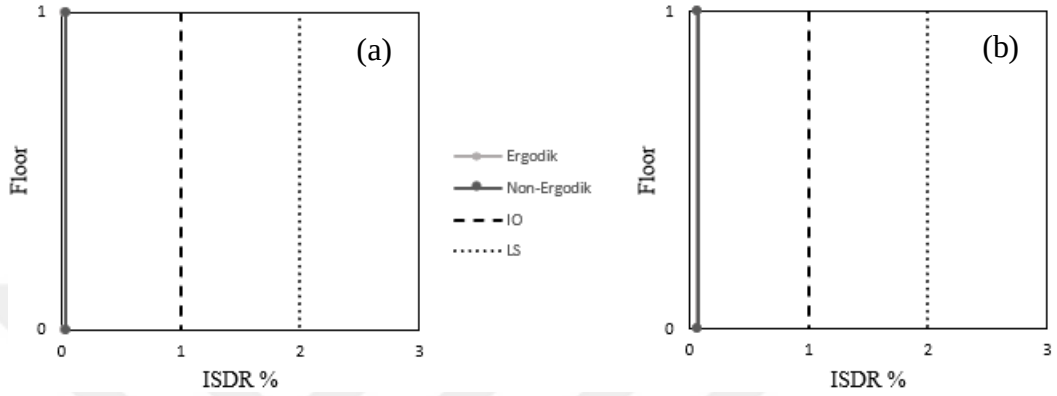

(1) Inter-storey drift ratios for the 1 storey building model at station site 2301 under strong motion records selected based on nonergodic and ergodic PSHA results based on Kale et al. (2015) study (a) Long. Dir. (b) Trans. Dir.

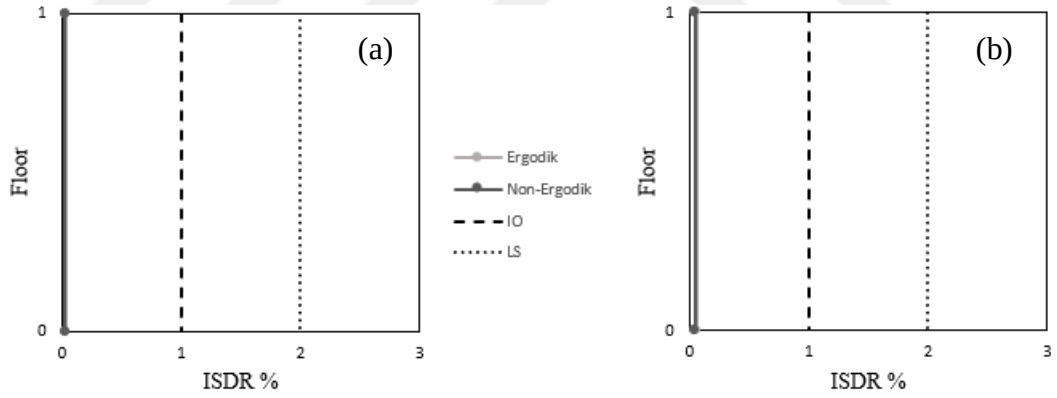

(2) Inter-storey drift ratios for the 1 storey building model at station site 2302 under strong motion records selected based on nonergodic and ergodic PSHA results based on Kale et al. (2015) study (a) Long. Dir. (b) Trans. Dir.

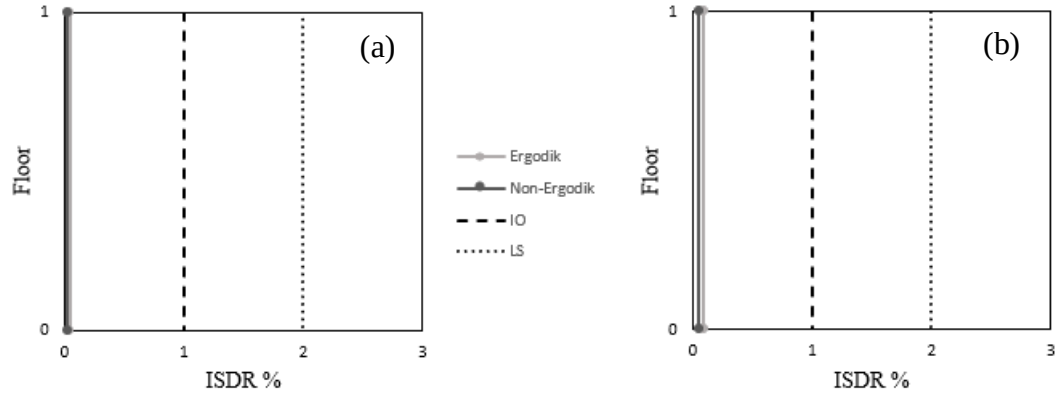

(3) Inter-storey drift ratios for the 1 storey building model at station site 2304 under strong motion records selected based on nonergodic and ergodic PSHA results based on Kale et al. (2015) study (a) Long. Dir. (b) Trans. Dir.

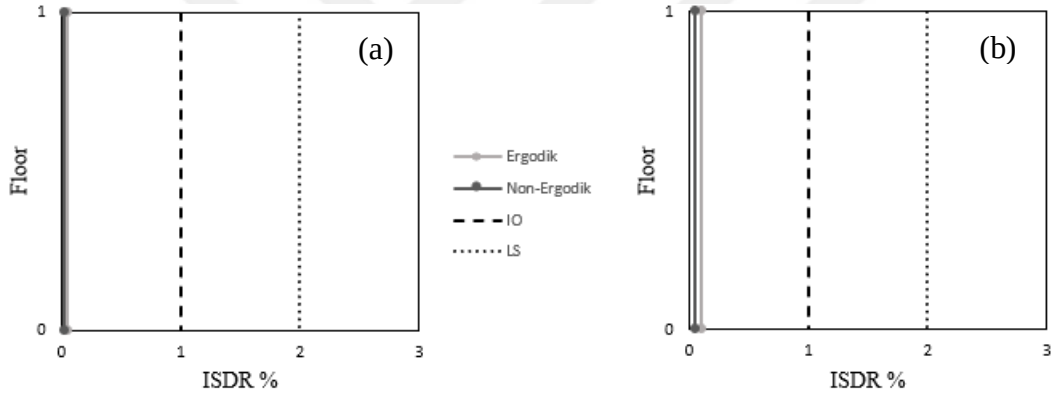

(4) Inter-storey drift ratios for the 1 storey building model at station site 2307 under strong motion records selected based on nonergodic and ergodic PSHA results based on Kale et al. (2015) study (a) Long. Dir. (b) Trans. Dir.

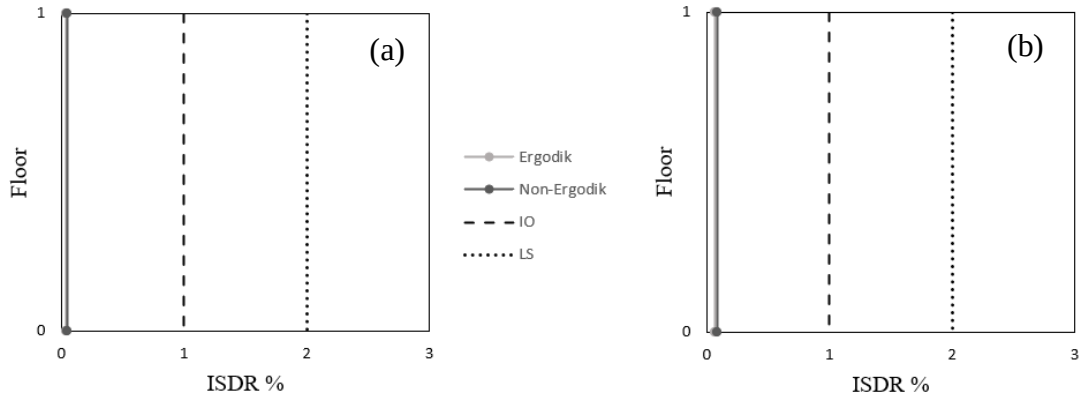

(5) Inter-storey drift ratios for the 1 storey building model at station site 2307 under strong motion records selected based on nonergodic and ergodic PSHA results based on Kotha et al. (2022) study (a) Long. Dir. (b) Trans. Dir.

Figure A.2 Inter-storey Drift Ratio (ISDR) for the Low-Rise Building Models

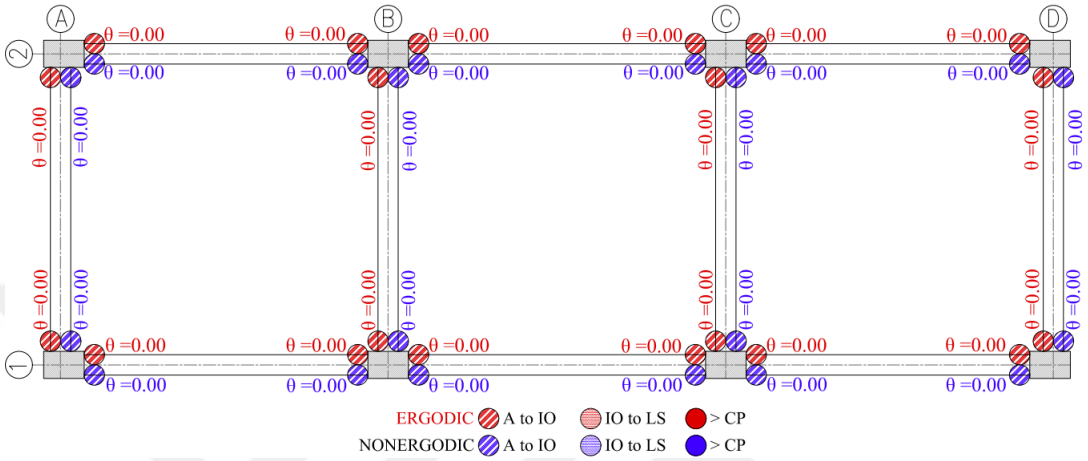

(1) Plastic hinge rotations for the 1 storey building model at station sites 2301,2302,2304 and 2307 under strong motion records selected based on nonergodic and ergodic PSHA results utilizing Kotha et al. (2022) and Kale et al. (2015) GMPM (The small circles represent hinges) Plastic rotation has not been observed in the beams. All beams have remained at the A-IO level in both cases.

Figure A.3 1st floor Plastic Rotations (Radians) of hinges for Mid-Rise Building Models

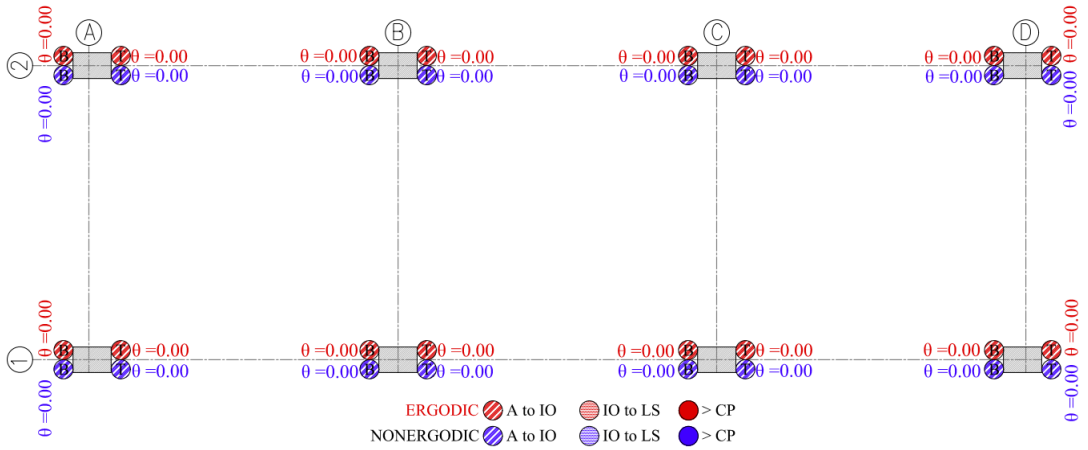

(1) Plastic hinge rotations for the 1 storey building model at station site 2301,2302,2304 and 2307 under strong motion records selected based on nonergodic and ergodic PSHA results utilizing Kotha et al. (2022) and Kale et al. (2015) GMPM (The small

circles represent hinges, B:Bottom Hinge, T:Top Hinge) Plastic rotation has not been observed in the columns. All columns have remained at the A-IO level in both cases.

Figure A.4 1st floor Plastic Rotations (Radians) of hinges for Low-Rise Building Models

B. BASE SHEAR/WEIGT-TİME GRAPHICS OF MID-RISE AND LOW-RISE BUILDINGS

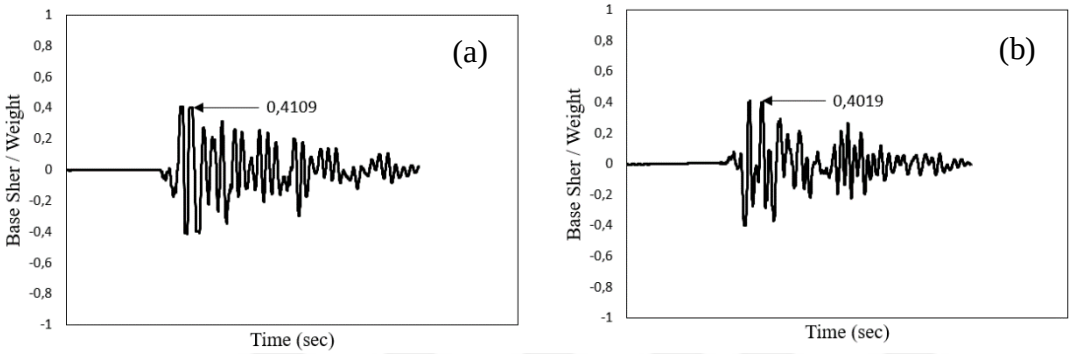

(1) Base Shear/Weight-Time graphics for the 5 storey building model at station site 2301 under strong motion records selected based on ergodic PSHA results based on Kale et al. (2015) study (a) Long. Dir. (b) Trans. Dir.

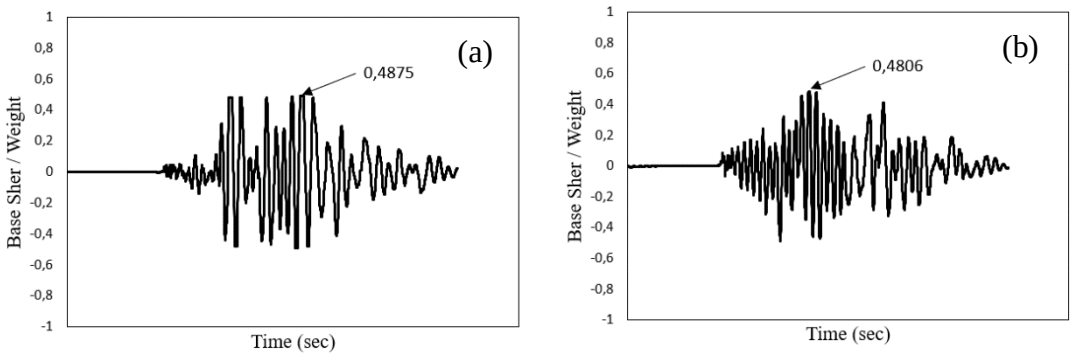

(2) Base Shear/Weight-Time graphics for the 5 storey building model at station site 2301 under strong motion records selected based on nonergodic PSHA results based on Kale et al. (2015) study (a) Long. Dir. (b) Trans. Dir.

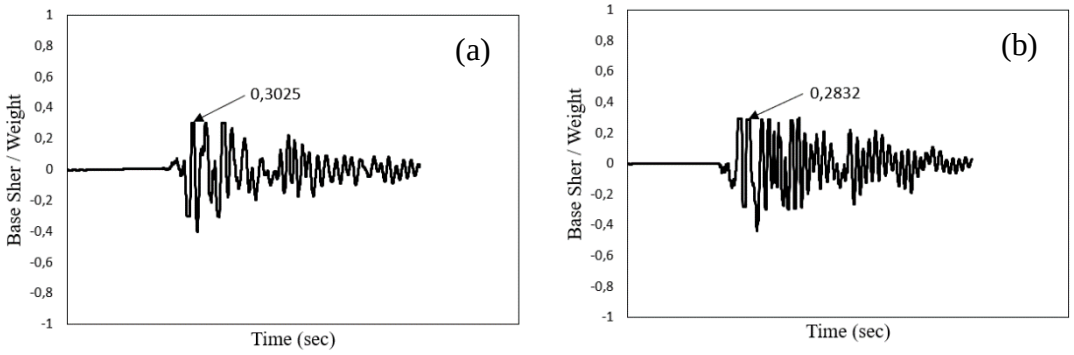

(3) Base Shear/Weight-Time graphics for the 5 storey building model at station site 2302 under strong motion records selected based on ergodic PSHA results based on Kale et al. (2015) study (a) Long. Dir. (b) Trans. Dir.

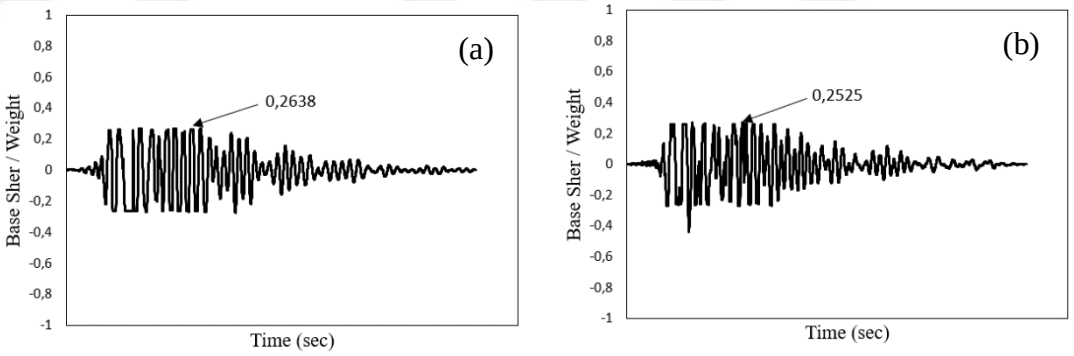

(4) Base Shear/Weight-Time graphics for the 5 storey building model at station site 2302 under strong motion records selected based on nonergodic PSHA results based on Kale et al. (2015) study (a) Long. Dir. (b) Trans. Dir.

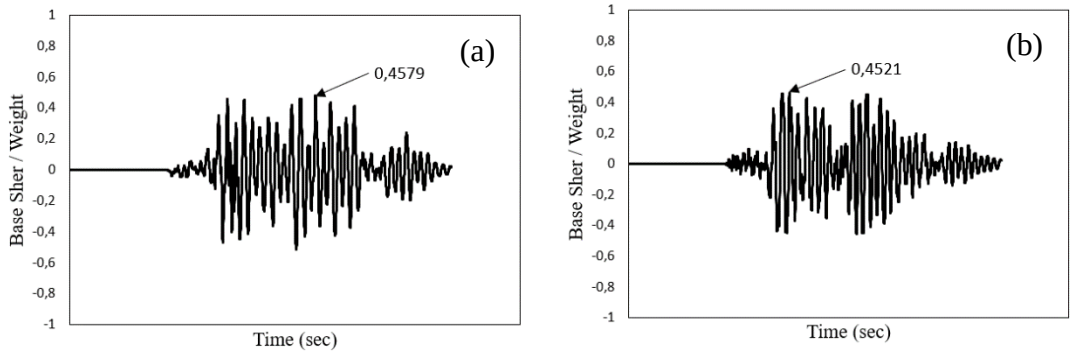

(5) Base Shear/Weight-Time graphics for the 5 storey building model at station site 2304 under strong motion records selected based on ergodic PSHA results based on Kale et al. (2015) study (a) Long. Dir. (b) Trans. Dir.

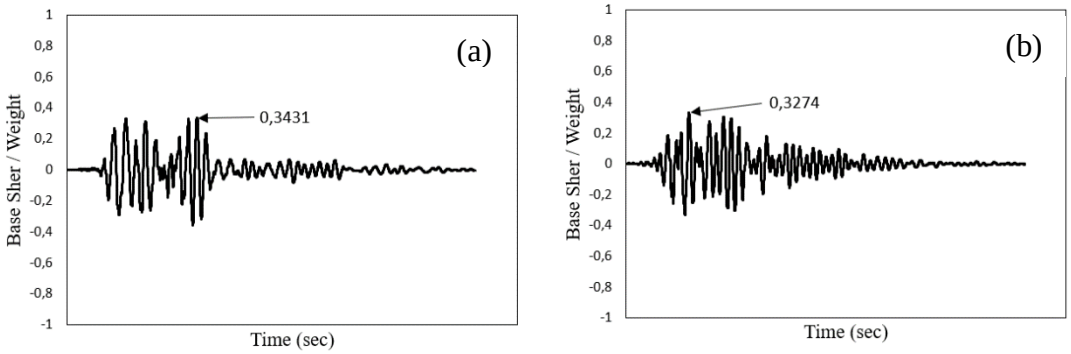

(6) Base Shear/Weight-Time graphics for the 5 storey building model at station site 2304 under strong motion records selected based on nonergodic PSHA results based on Kale et al. (2015) study (a) Long. Dir. (b) Trans. Dir.

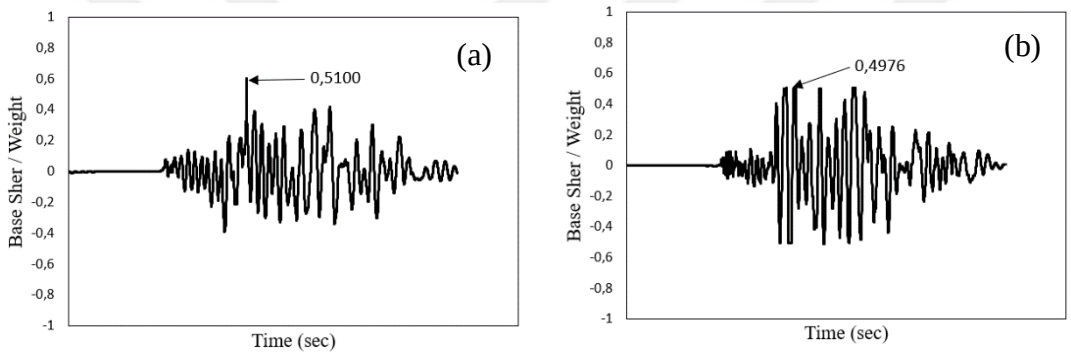

(7) Base Shear/Weight-Time graphics for the 5 storey building model at station site 2307 under strong motion records selected based on ergodic PSHA results based on Kale et al. (2015) study (a) Long. Dir. (b) Trans. Dir.

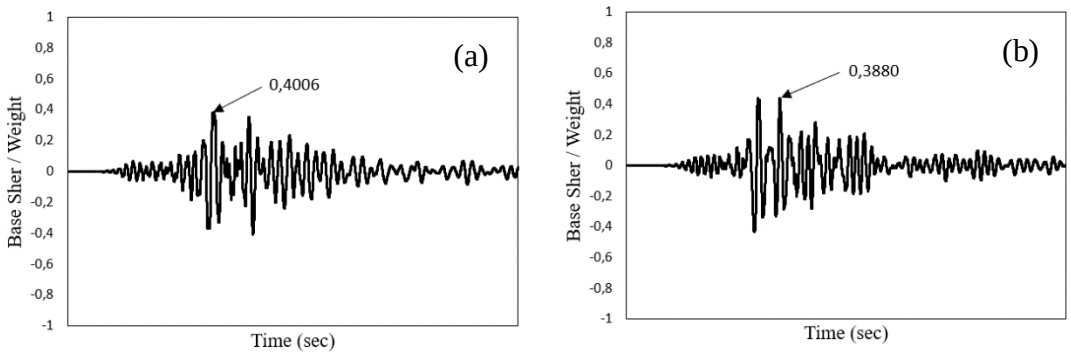

(8) Base Shear/Weight-Time graphics for the 5 storey building model at station site 2307 under strong motion records selected based on nonergodic PSHA results based on Kale et al. (2015) study (a) Long. Dir. (b) Trans. Dir.

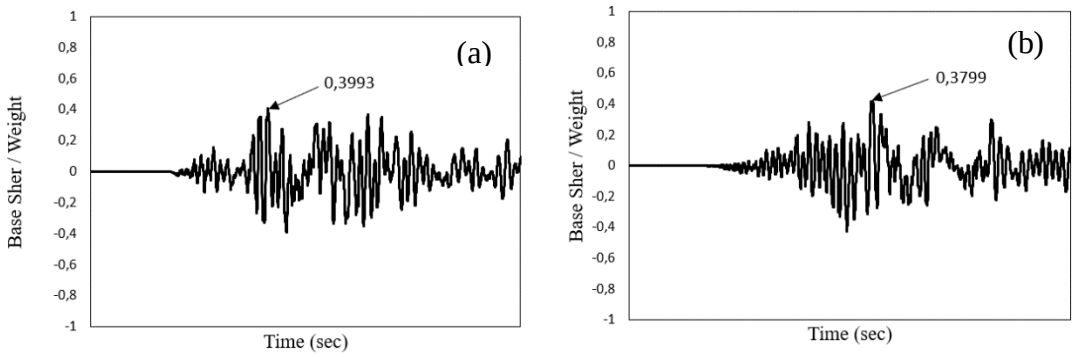

(9) Base Shear/Weight-Time graphics for the 5 storey building model at station site 2301 under strong motion records selected based on ergodic PSHA results based on Kotha et al. (2022) study (a) Long. Dir. (b) Trans. Dir.

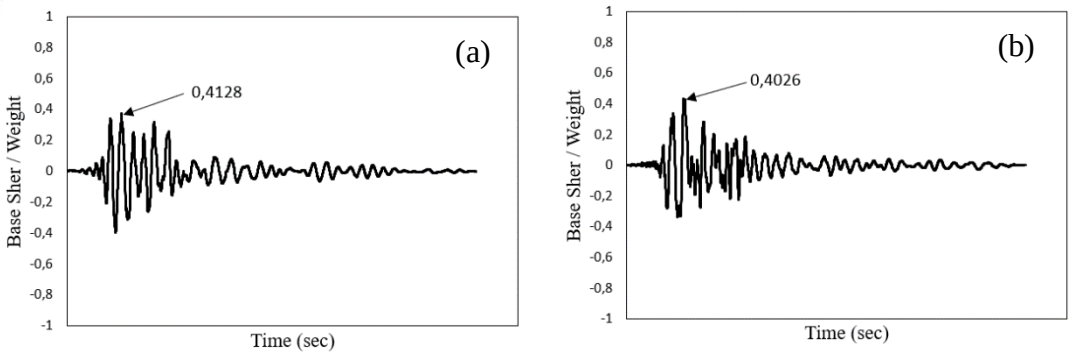

(10) Base Shear/Weight-Time graphics for the 5 storey building model at station site 2301 under strong motion records selected based on nonergodic PSHA results based on Kotha et al. (2022) study (a) Long. Dir. (b) Trans. Dir.

Figure A.5 Base Shear/Weight-Time graphics for the Mid-Rise Building Models

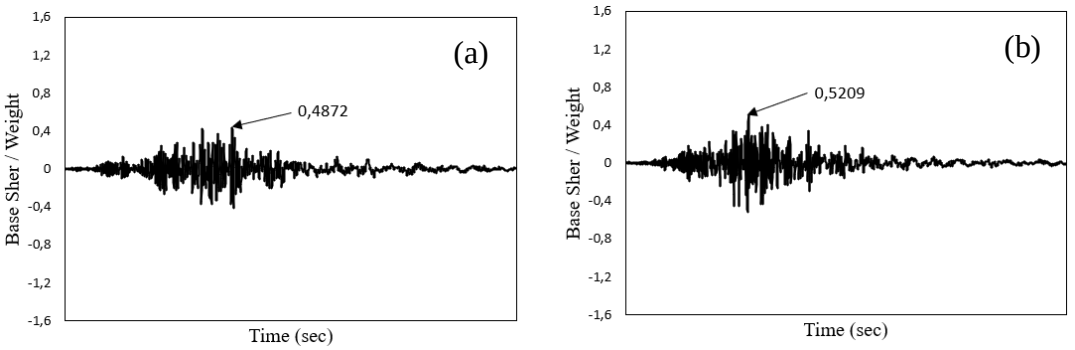

(1) Base Shear/Weight-Time graphics for the 1 storey building model at station site 2301 under strong motion records selected based on ergodic PSHA results based on Kale et al. (2015) study (a) Long. Dir. (b) Trans. Dir.

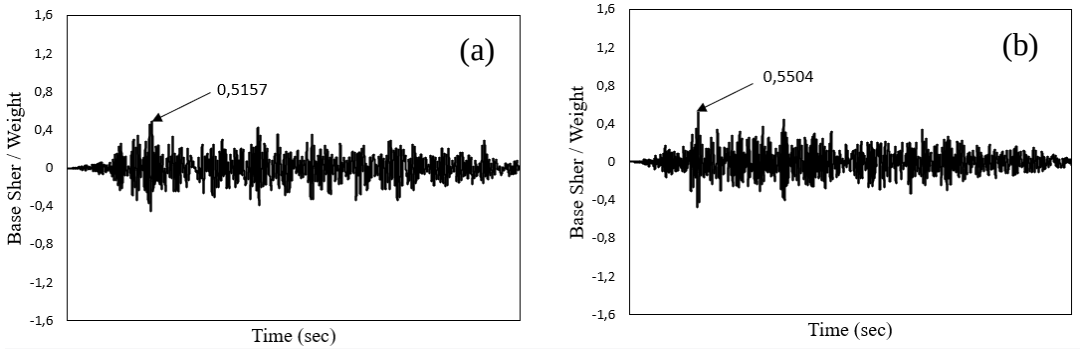

(2) Base Shear/Weight-Time graphics for the 1 storey building model at station site 2301 under strong motion records selected based on nonergodic PSHA results based on Kale et al. (2015) study (a) Long. Dir. (b) Trans. Dir.

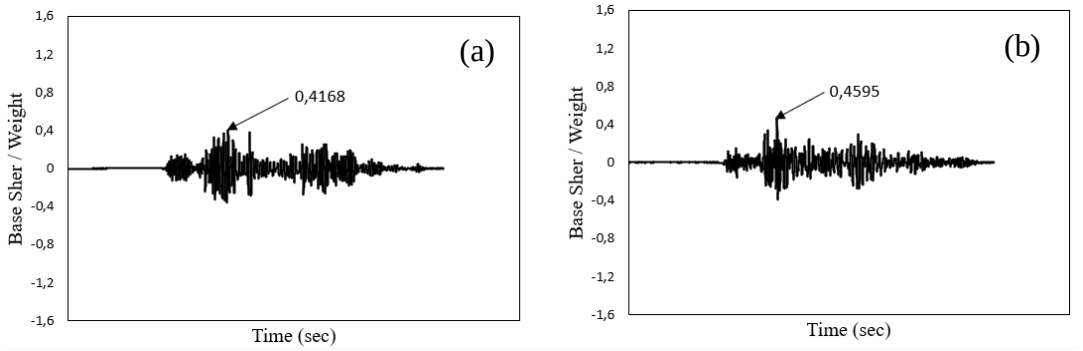

(3) Base Shear/Weight-Time graphics for the 1 storey building model at station site 2302 under strong motion records selected based on ergodic PSHA results based on Kale et al. (2015) study (a) Long. Dir. (b) Trans. Dir.

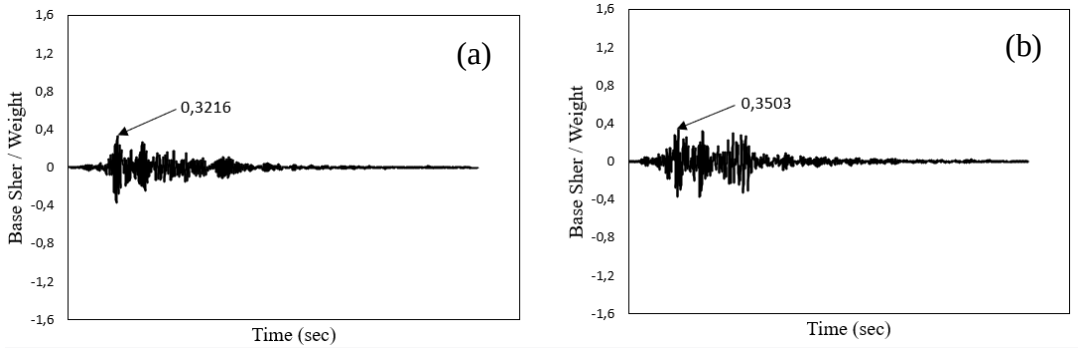

(4) Base Shear/Weight-Time graphics for the 1 storey building model at station site 2302 under strong motion records selected based on nonergodic PSHA results based on Kale et al. (2015) study (a) Long. Dir. (b) Trans. Dir.

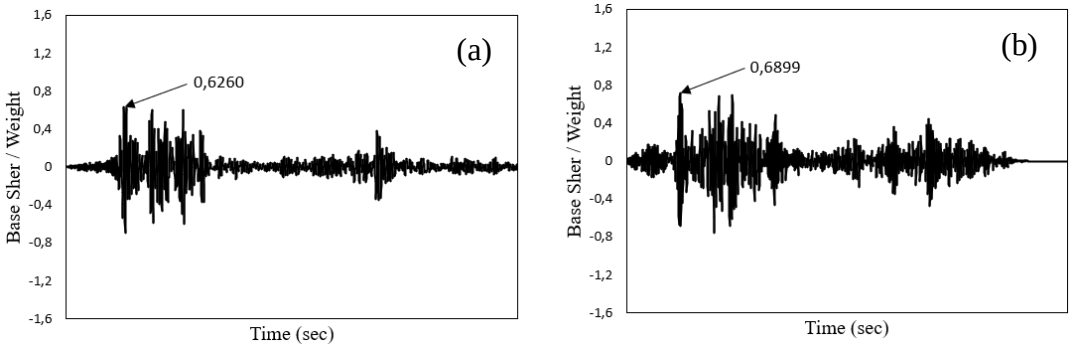

(5) Base Shear/Weight-Time graphics for the 1 storey building model at station site 2304 under strong motion records selected based on ergodic PSHA results based on Kale et al. (2015) study (a) Long. Dir. (b) Trans. Dir.

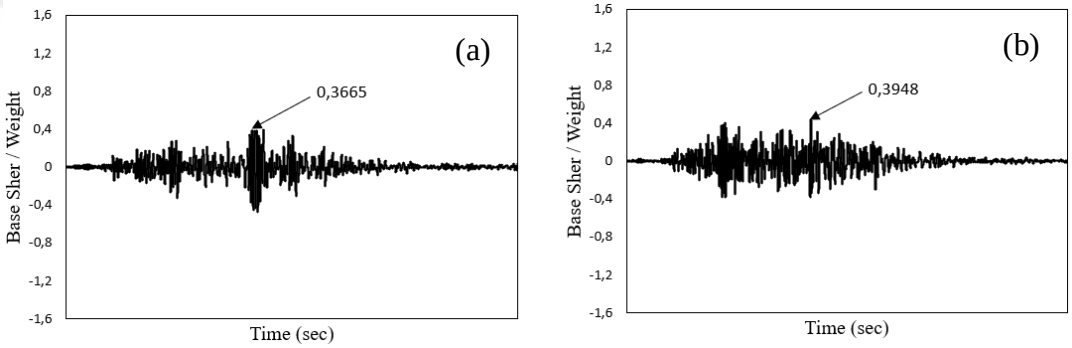

(6) Base Shear/Weight-Time graphics for the 1 storey building model at station site 2304 under strong motion records selected based on nonergodic PSHA results based on Kale et al. (2015) study (a) Long. Dir. (b) Trans. Dir.

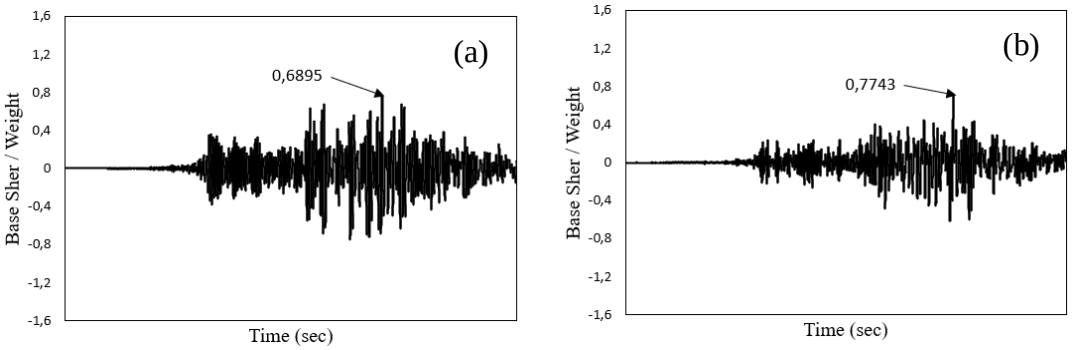

(7) Base Shear/Weight-Time graphics for the 1 storey building model at station site 2307 under strong motion records selected based on ergodic PSHA results based on Kale et al. (2015) study (a) Long. Dir. (b) Trans. Dir.

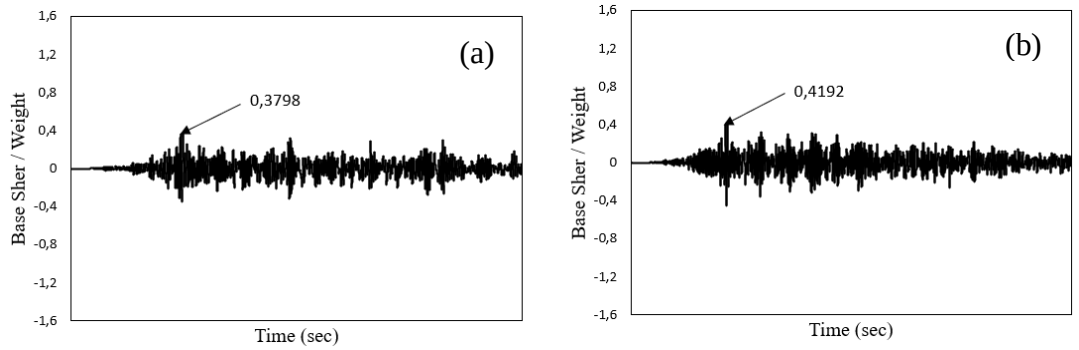

(8) Base Shear/Weight-Time graphics for the 1 storey building model at station site 2307 under strong motion records selected based on nonergodic PSHA results based on Kale et al. (2015) study (a) Long. Dir. (b) Trans. Dir.

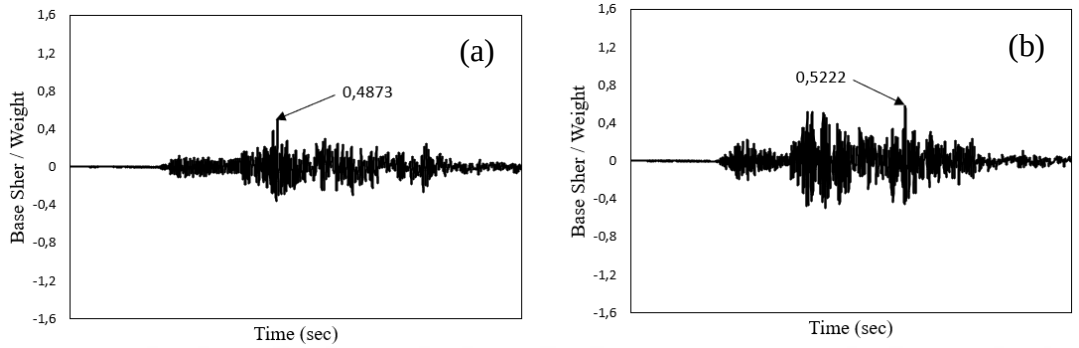

(9) Base Shear/Weight-Time graphics for the 1 storey building model at station site 2301 under strong motion records selected based on ergodic PSHA results based on Kotha et al. (2022) study (a) Long. Dir. (b) Trans. Dir.

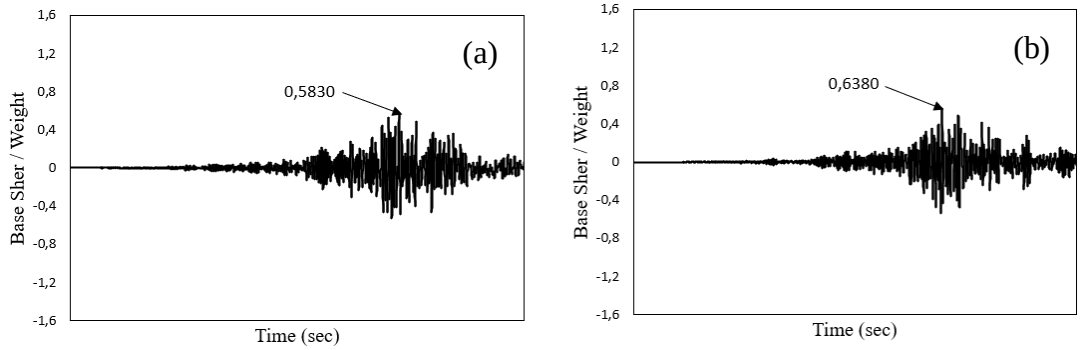

(10) Base Shear/Weight-Time graphics for the 1 storey building model at station site 2301 under strong motion records selected based on nonergodic PSHA results based on Kotha et al. (2022) study (a) Long. Dir. (b) Trans. Dir.

Figure A.6 Base Shear/Weight-Time graphics for the Low-Rise Building Models

C. 2nd FLOOR PLASTIC ROTATIONS OF BEAMS AND COLUMNS OF MID-RISE BUILDINGS

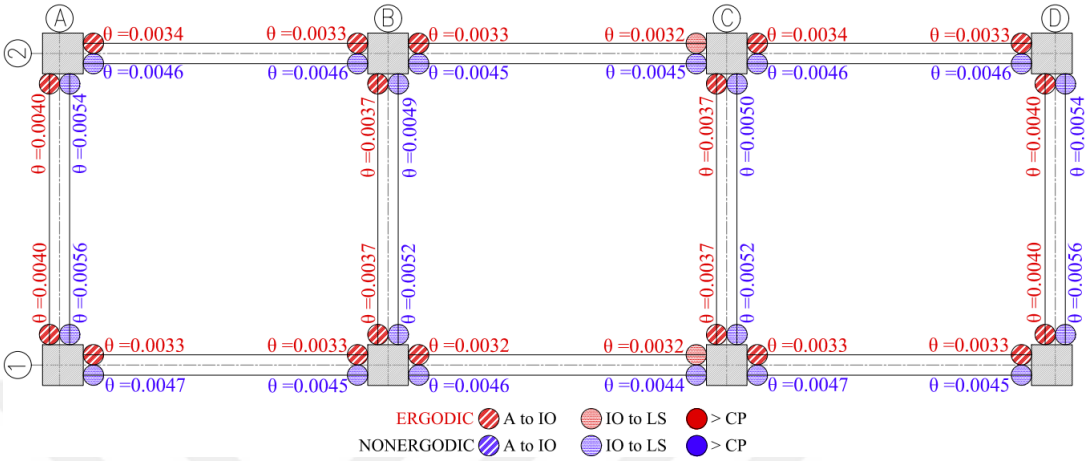

(1) Plastic hinge rotations for the 5 storey building model at station site 2301 under strong motion records selected based on nonergodic and ergodic PSHA results utilizing Kale et al. (2015) GMPM (The small circles represent hinges) In the ergodic PSHA case, with the exception of two beams in the longitudinal direction, all other beams remain at the A-IO level. In the non-ergodic PSHA case, all beams are at the IO-LS level.

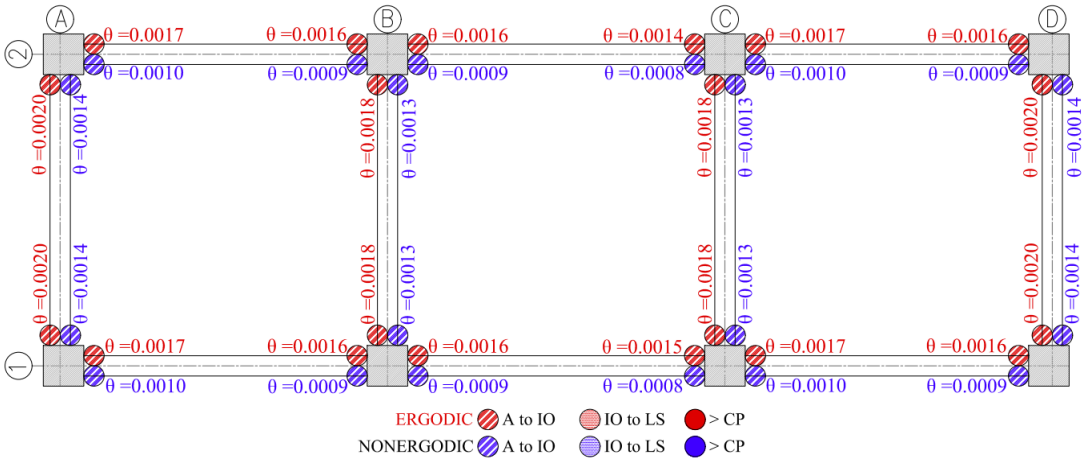

(2) Plastic hinge rotations for the 5 storey building model at station site 2302 under strong motion records selected based on nonergodic and ergodic PSHA results utilizing Kale et al. (2015) GMPM (The small circles represent hinges) In both PSHA cases, all beams are at the A-IO level.

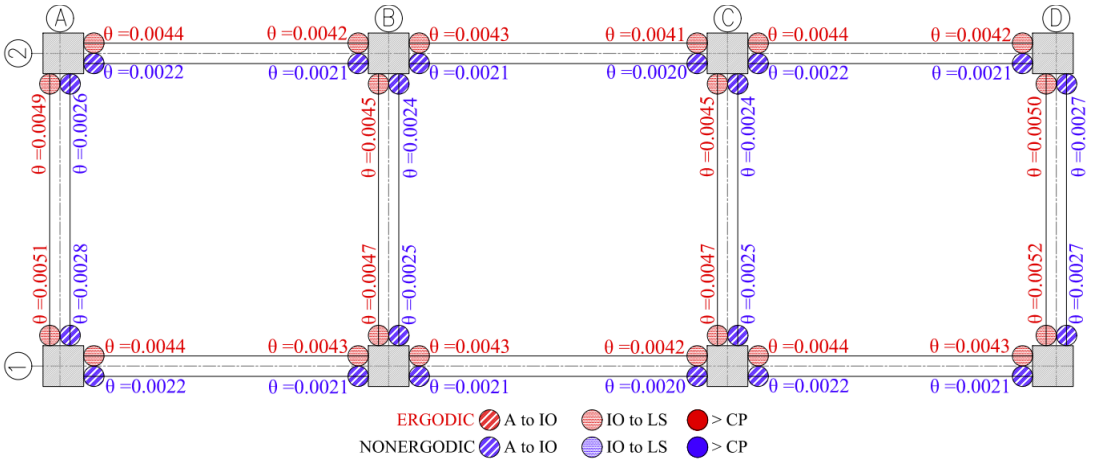

(3) Plastic hinge rotations for the 5 storey building model at station site 2304 under strong motion records selected based on nonergodic and ergodic PSHA results utilizing Kale et al. (2015) GMPM (The small circles represent hinges) In the ergodic PSHA case, all beams remain at the IO-LS level, whereas in the non-ergodic PSHA case, all beams have remained at the A-IO level.

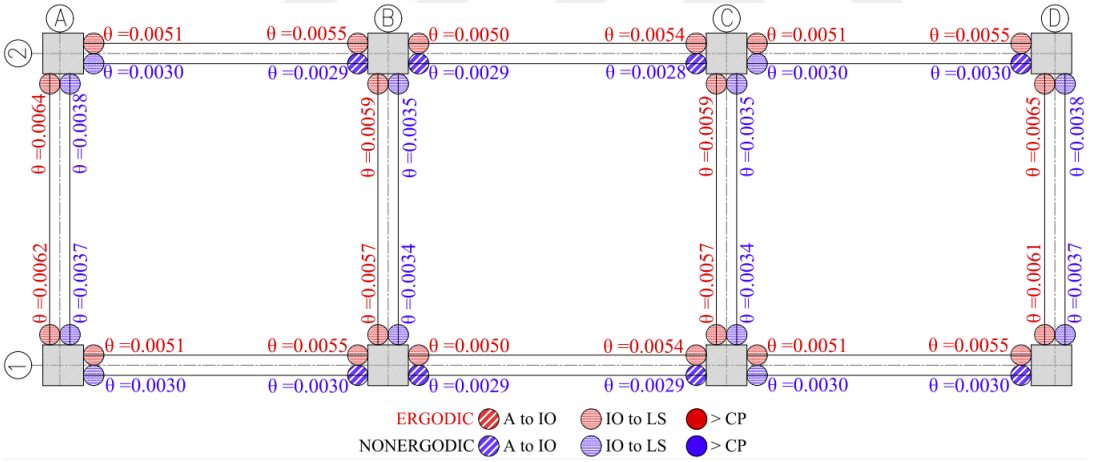

(4) Plastic hinge rotations for the 5 storey building model at station site 2307 under strong motion records selected based on nonergodic and ergodic PSHA results utilizing Kale et al. (2015) GMPM (The small circles represent hinges) In the ergodic PSHA case, all beams are at the IO-LS level, whereas in the non-ergodic PSHA case, eight of the hinges at longitudinal direction of building remain at the A-IO level, while the rest are at the IO-LS level.

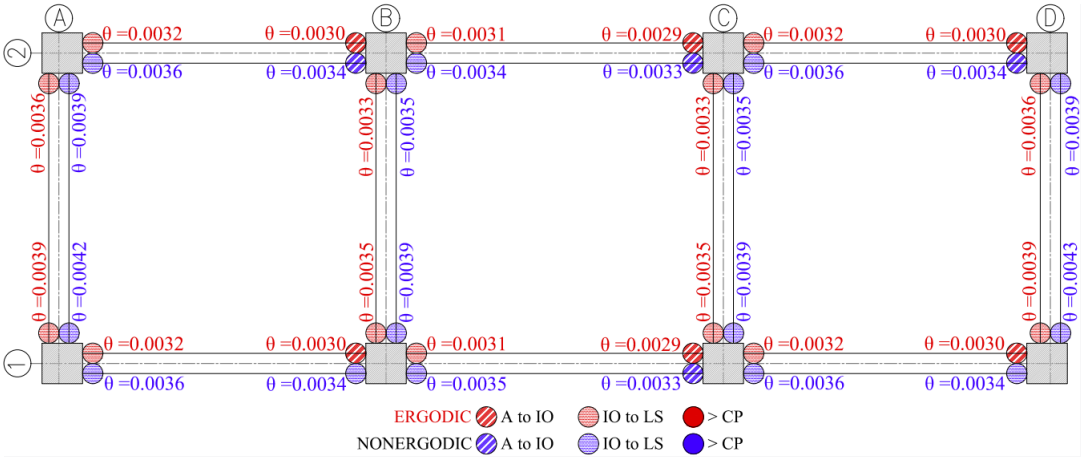

(5) Plastic hinge rotations for the 5 storey building model at station site 2301 under strong motion records selected based on nonergodic and ergodic PSHA results utilizing Kotha et al. (2022) GMPM (The small circles represent hinges) In the ergodic PSHA case, overall, all beams are at the IO-LS level, while in the longitudinal direction, six hinges are at the A-IO level. Similarly, in the non-ergodic PSHA case, generally, all beams are at the IO-LS level, with four hinges in the longitudinal direction at the A-IO level.

Figure A.7 2nd Floor Plastic Rotations (Radians) of Hinges for Mid-Rise Building Models

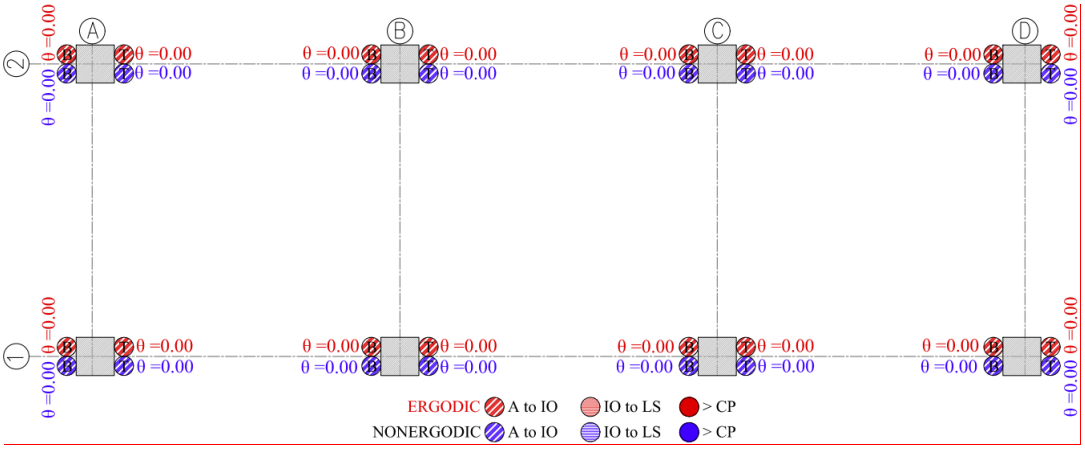

(1) Plastic hinge rotations for the 5 storey building model at station site 2301,2302,2304 and 2307 under strong motion records selected based on nonergodic and ergodic PSHA results utilizing Kotha et al. (2022) and Kale et al. (2015) GMPM (The small circles represent hinges, B:Bottom Hinge, T:Top Hinge) No plastic rotation has been observed in any column.

Figure A.8 2nd Floor Plastic Rotations (Radians) of Hinges for Mid-Rise Building Models